PREBIOTIC CHEMISTRY ON MINERAL SURFACES: PROTO-OLIGOPEPTIDE FORMATION ON SILICA AND OTHER SUBSTRATES WITHIN DEPSIPEPTIDE FORMING SYSTEMS

A Dissertation
Presented to
The Academic Faculty

by

Aaron Douglas McKee

In Partial Fulfillment
of the Requirements for the Degree
Doctor of Philosophy in the
School of Chemistry and Biochemistry

Georgia Institute of Technology
December 2019

PREBIOTIC CHEMISTRY ON MINERAL SURFACES:

PROTO-OLIGOPEPTIDE FORMATION ON SILICA AND OTHER

SUBSTRATES WITHIN DEPSIPEPTIDE FORMING SYSTEMS

Approved by:

Dr. Thomas Orlando, Advisor
School of Chemistry and Biochemistry
Georgia Institute of Technology

Dr. Nicholas Hud
School of Chemistry and Biochemistry
Georgia Institute of Technology

Dr. Charles Liotta
School of Chemistry and Biochemistry
Georgia Institute of Technology

Dr. Facundo Fernández
School of Chemistry and Biochemistry
Georgia Institute of Technology

Dr. James Wray
School of Earth and Atmospheric Sciences
Georgia Institute of Technology

Date Approved: August 23, 2019

For my father.

ACKNOWLEDGEMENTS

There are many people that I must thank for their invaluable assistance throughout all facets of my PhD, without whom, my attrition would not be possible:

My advisor, Thomas Orlando, for admitting me into his lab, supporting me, advocating for me and giving me the space to discover, while also giving me the guidance to remain efficient with my time.

The Center for Chemical Evolution (CCE), for introducing me to the wonders of Origins of Life and Astrobiological research, and providing many opportunities to learn, grow, network, travel, share my work and build new things to spread around the science and non-science community.

My committee, for your guidance, wisdom and collaboration with every challenge, presentation and paper.

My parents, Julie and Chadwick McKee, who were relentless in their encouragement and love, and raised me to be curious, observant and to think critically.

My wonderful partner, Aida Demissie, for being the best, and my most favorite, person I have met, who I have had the pleasure of sharing all matters of highs and lows with, learning from, and who I hope to always have by my side, hand-in-hand, in our adventure forward through a wonderful life.

My brother, Nathan McKee, who has always been an inspiration to keep going, who is one of my favorite people to talk to and who grows more dear to me every time I see him.

TABLE OF CONTENTS

LIST OF TABLES

LIST OF FIGURES

silica. Poly-condensation of the GGG reactant occurs to a greater degree when silica is present. Both MOPA and NAG were excluded to demonstrate that non-monomeric G is capable of sustaining oligomerization via silyl-ester aminolysis.

with only water. The sharp peak associated with isolated silanols is absent for quartz.

indicates a net loss of carbon from the sample surface, with losses of C^i and C^{ii} being the largest.

LIST OF SYMBOLS AND ABBREVIATIONS

COoL	Chemical origins oflife
NASA	National Aeronautics and Space Administration
AA	Amino acid
HA	α-hydroxy acid
EAX	Ester aminolysis, ester amide exchange
LA	Lactic
G	Glycine
A	Alanine
MS	Mass spectrometry
ESI-MS	Electrospray ionization mass spectrometry
LC-MS	Liquid chromatography mass spectrometry
NMR	Nuclear magnetic resonance spectroscopy
IR	Infrared spectroscopy
ATR-IR	Attenuated total reflectance infrared spectroscopy
DRIFTS	Diffuse reflectance infrared Fourier transform spectroscopy
a.u.	Arbitraty units
mM	Millimolar
mL	Milliliter
μL	Microliter
mg	Milligram
°C	Degrees Celsius
ppm	Parts per million

pH	Logarithm of the concentration of hydrogen ions in molarity
MOPA	2-methoxypropionic acid
NAG	N-acetyglycine
GGG	Tri-glycine
XPS	x-ray photoelectron spectrometer or spectroscopy
DKP	Diketopiperazine
C18	18-unit hydrocarbon chain
KHP	Potassium hydrogen phthalate
ACN	Acetonitrile
eV	Electron volt
σ	Mean, average
Ga	Billion years ago
amu	Atomic mass unit
LEE	Low energy electron
DEA	Dissociative electron attachment
TEY	Total electron yield

SUMMARY

The chemical origins of life is not a completely intractable, but it is incredibly complex. Life can be broken down into its major processes, which can be described by the actions of several major components, which themselves are constructed from increasingly simple and ordinary sub-units, and eventually, the building blocks of life. Much of prebiotic chemistry seeks to describe this process in reverse; how can these monomers become oligomers, then polymers with function, self-replication, etc.

The formation of poly-peptides by a plausibly prebiotic process has persisted as an unanswered problem since the earliest proposals of abiogenesis. A possible answer is that ~4 billion years ago, there was a distant chemical ancestor of the poly-peptide, which, through chemical evolution, slowly came to more closely resemble our extant proteins. The question of how could such a proto-peptide could transform remains an important question.

This thesis describes how the presence of minerals, the ubiquitous substrates that existed on an early Earth, affect the composition of a proto-peptide system, composed of amino acids and a similar chemical class, hydroxy acids, that forms oligomeric depsipeptides. It will be demonstrated that the addition of silica to a depsipeptide reaction results in amino acid enrichment and that the ester aminolysis mechanism that proceeds in a homogeneous condition is also able to proceed on the substrate surface as silyl-ester aminolysis. The specific mineral characteristics that make silica an ideal participant in this mechanism will be discussed, along with the exploration for other minerals that would be present on early Earth and capable of facilitating proto-peptide formation at an interface.

CHAPTER 1.   POSSIBLE ROLES OF MINERAL-ORGANIC INTERFACES IN PREBIOTIC CHEMISTRY

1.1   The Chemical Origins of Life

1.1.1   Prebiotic Chemistry

One of the longest standing, most intricate, even personal, questions regards the origins of life on Earth. The phenomena of abiogenesis refers to the conversion of non-living matter, such as organic molecules and other simple compounds, into a living system. While the mechanisms of such a transformation are the subjects of prebiotic chemistry and many other scientific sub-disciplines, there exists contention even in the definition of life itself [1]. The definition most prominently used by the United States National Aeronautics and Space Administration (NASA) is "Life is a self-sustained chemical system capable of undergoing Darwinian evolution" [2]. The intention of a definition in this case is to guide experimental design and provide a scaffold for concepts to be tested and new theories proposed. However, many definitions of life exist and are varied in their specificity, intent and interpretation [3].

One way to frame these denotative conflicts is to categorize the definitions as descriptive and prescriptive. A descriptive approach to defining life entails observing entities that are considered living, then constructing a definition as a collection of those characteristics. In many ways this is an intuitive method, as the source for each characteristic is undeniable, as there would be an example of a living entity possessing it. Such a definition would ultimately comprise of the set of traits that all living entities share,

but this method relies on a firm knowledge of which entities are living and which are not. Difficulty would arise when presented with something that may or may not be living such as a planet [4], a self-reproducing cellular system without genes [5] or proteins [6]. It becomes clear that a descriptive approach is biased and possibly hindered by our current understanding and experience of life. A prescriptive definition declares what *should* qualify as living or non-living and can be used to verify a living system based on its ability to meet those criteria. While this approach is very practical in performing tests to qualify if a system is living, drawbacks include the ability to categorically include too many or too few systems. Nevertheless, these prescriptive definitions are informed by observation and provide a more substantial framework for designing model prebiotic experiments than from a purely descriptive basis. One of the earliest accounts of modern chemical origins of life discourse comes from Alexander Oparin when he discussed a primordial soup, the physical similarity of living and non-living matter, and emergent properties of life arising from complex systems [5]. Oparin proposed a list of necessary qualifications which included self-reproduction and growth [7]. Other definitions have suggested "self-sustaining" [1], and from those, the concept of self-assembly [8] has been adopted. Prebiotic chemistry seeks to describe possible pathways that simple non-living matter could have acquired these characteristics and functional capabilities that are necessary for life, through various chemical processes.

Modern bio-macromolecules are polymers of bio-monomers such as nucleotides for RNA and DNA, sugars for polysaccharides and amino acids for proteins. While these bio-monomers are integral components of complex metabolic and physiological processes, the molecules themselves can be produced from simple compounds, e.g.

CH_4, NH_3, CO_2 and H_2O. The famed Miller-Urey experiment [9] demonstrated that these simple organic and inorganic gases could serve as feedstock, along with an external energy source, to form many of the building blocks of modern biology. Amino acids were among the most identified product of this model prebiotic reaction, with simple side-chain species dominating, but charged side-chain species such as aspartic acid, still detected. These crucial bio-monomers have also been identified in extra-terrestrial samples, such as the Murchison meteorite [10, 11] and are known to have been continuously deposited on the terrestrial surface from micrometeorites and by interplanetary dust particles [12]. With the availability of biological building blocks established, organization of these units into polymers with functionality and structure is the next step in chemical evolution towards the origins of life.

A prevailing theory for the origin of life is the RNA world hypothesis [13]. This theory asserts that self-replicating RNA is a prime candidate for a most primitive macromolecule and would predate proteins and DNA, as it has been shown capable of catalysis [14] and information storage [15, 16]. However, the RNA monomer is a nucleotide that possess three sub-units, the nucleobase, sugar and phosphate. Though a prebiotically plausible synthetic route has been proposed [17, 18], the poly-condensation of those monomers remains a barrier. An alternative biopolymer class that might also possess functional capabilities is the poly-peptide. Poly-peptides are attractive due to their elevated monomer yields in model prebiotic reactions [19], catalytic activity and ability to form secondary structures, e.g. β-sheets [20], which may promote self-replication and survivability. Peptides have even been purposed as the first genetic polymer as peptide nucleic acids [21]. Additionally, the diversity of amino acid peptide monomers [22], and

robustness of the peptide linkage [23, 24] present prebiotic poly-peptides as a goal worth pursuing.

1.1.2   *Challenges in Chemical Evolution*

Water is considered a crucial component of life and much of the Earth's surface is part of an oceanic system. While marine hydrothermal systems are popular setting for origins of life theories, aqueous environments are not well suited for the one of the most imperative classes of chemical transformations necessary for the production of early prebiotic molecules, the condensation reaction. The formation of amide linkages for poly-peptides, phosphoesters for nucleic acids and even esters all rely on condensation reaction to connect monomers and elongate the polymer. However, the formation of peptide and ester bonds in aqueous solution is not thermodynamically favored [25]. As shown in Figure 1-1, water is a product of this process and therefore reactants do not proceed toward the condensed side of the reaction if water is already abundant. One solution to this problem draws inspiration from periodic environmental cycles that likely existed on early Earth, e.g. seasonal and daily variations in temperature and humidity or tidal activity, to justify conducting reactions in an evaporative environment. With minimal or no hydration, condensation in general becomes more favored. However, for amino acid systems, temperature for direct amide formation in the absence of an activating agent are considered high, i.e. >150 °C, for a plausible prebiotic model [26, 27]. A secondary issue that occurs in exclusively amino acid systems is the diketopiperazine (DKP) "trap," which results from the cyclization of two amino acid monomers and becomes a sink for starting reactants and impedes formation of longer, linear peptides [28, 29].
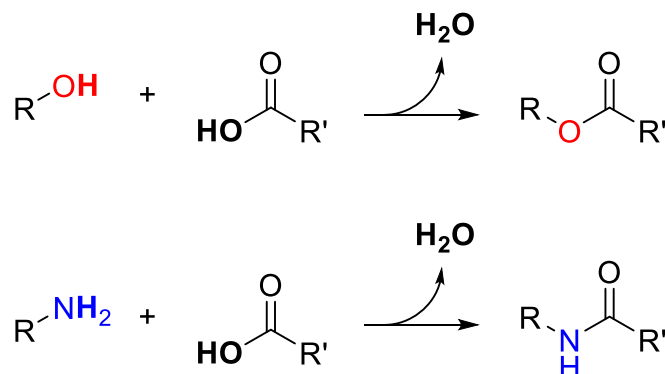
Figure 1-1   Examples of condensation reactions, featuring ester (top) and amide (bottom) formation, with carboxylic acid electrophiles.

Difficulties in poly-condensation exist in model reactions for all major bio-macromolecules and has inspired the use of non-canonical or analogous reactants. A new paradigm in origins of life research interprets the concept of chemical evolution to suggest that extant biological macromolecules developed from related, but not exact, ancestor molecules. These *progenimers* of familiar molecular classes, e.g. nucleic acids, proteins or polysaccharides, are the chemical ancestors of extant molecules; they may have possessed a similar function or form, but likely departed from modern incarnations in some manner. These early versions were likely formed by chemical processes that were more accessible or resulted in more stable assemblies given early Earth conditions and a lack of complex enzymatic catalysis. A nucleic acid progenimer may have included non-canonical nucleobases [30], a ribose alternative, or alternative backbone bonding schema [21, 31]. A protein progenimer may have contained non-canonical residues or even non-amide linkages, such as esters in the cases of depsipeptides [32, 33], or thioesters [34]. Preceding what resembles even the simplest of extant organisms would be the emergence of chemical

systems that possess some characteristics of functionality, self-assembly, replication and complexity [35]. While many details of the emergence of life remain in debate, the principal of evolution within prebiotic chemical systems is understood to be a plausible path towards extant biology from simple bio-monomers comprising the prebiotic inventory [36, 37].

1.2 Minerals in a Prebiotic Context

1.2.1 Background

Distinct from laboratory reactions, a common scenario for a molecule on early Earth would be either well-diluted in aqueous solution [38] or in contact with a mineral substrate [39, 40], while an encounter with a possible reactant might be rarer. In aqueous solution, poly-condensation is typically disfavored thermodynamically [41], but molecular films formed by evaporation of water onto a mineral surface would be both plausible and conducive towards oligomerization. J.D. Bernal, in his 1951 book *The Physical Basis of Life*, suggested that minerals, especially clays, may have provided confinement and catalysis for simple organic chemicals and contributed to the origins of life [42]. While Bernal himself never investigated these claims directly, there have been efforts to study the potential role minerals might have played in the in the emergence of life, and what aspects of mineral chemical composition, structure, defects and impurities contribute to these interactions. The early Earth, distinct from present day Earth, contained many environments that may have been conducive for the production of necessary prebiotic molecules. It has been established that significant mineral diversity on the early Earth likely presented myriad distinct settings in which chemistry leading to the emergence of life could

have proceeded [43]. The ubiquity of mineral-water and mineral-organic interactions, assuming the omnipresence of available surfaces in an evaporative environment, dictates that these interfaces must be considered in a comprehensive prebiotic model for origins of life chemistry.

1.2.2   Plausible Prebiotic Minerals

Minerals are naturally occurring inorganic compounds with specific crystalline structures and are typically categorized into a range of chemical compositions, e.g. montmorillonite, $(Na,Ca)_{0.33}(Al,Mg)_2(Si_4O_{10})(OH)2 \cdot nH_2O$, can contain various cation ratios distinct from its archetypal endmember [44]. Differentiated terrestrial geology predates the deposition of oceanic water [45] and cooling of the surface to a temperature that could support and sustain prebiotic chemical reactions [12]. Distinct from chemical evolution, the early Earth mineral inventory also underwent a type of mineral evolution due to changes in temperature and contact with the atmosphere and water [46]. While present mineral diversity amounts to 4000-4500 distinct mineral species, ~4 Ga there were likely up to 1000 unique species [44]. It is necessary to prioritize minerals that were likely abundant over rarer species when conducting model prebiotic reactions to maintain high plausibility.

In the earliest relevant period, predating even the Late Heavy Bombardment [47], the Earth's mantle had rapidly differentiation and consequently, the majority of lithospheric minerals where mafic (magnesium and iron rich) silicates, along with iron-nickel phosphides and alloys [44]. Following thermal, aqueous and impact processing, phosphates and clay silicates developed, specifically tectosilicates, e.g. feldspars, which

are highly structured aluminosilicates and compose ~75% of the terrestrial crust [48]. With increased volcanism, basaltic (a silica deficient mafic variety) magma joined the surface mineral inventory. Subductive and volcanic activity contributed to mineral speciation, along with prolonged exposure to intense thermal conditions led to hydrous minerals like hydroxides and zeolites [46]. Clays were present during the period that likely proceeded the emergence of life, while quartz (SiO_2) would have been present later, form 4.0-3.5 Ga [44]. On earth, the primary constituents of the primitive mantle, and later the outer crust, were silicates [49], which presented in many forms and with diverse surface terminations. Silicates expand on the core SiO_4 unit, with significant variety in crystalline structure, chemical ratios and cationic inclusion. The most relevant silicate major-groups for prebiotic chemistry are likely the phyllosilicates and tectosilicates.

Phyllosilicates, broadly referred to as clays [50], include kaolinite and montmorillonite, in addition to non-clay groups, e.g. the serpentine and mica subgroups. Their most distinguishing feature is a sheet-like arrangement, which results in interlayer distances that range from ~10 Å to an astonishing 20-30 Å when fully swelled in water [51]. Clays can accommodate multi-valent cationic substitutions. While clays are typically negatively charged in neutral or mildly acidic conditions, the edges can be positively charged. Tectosilicates, including the main feldspar and zeolite subgroups, are hydrous and cation containing aluminosilicates that are highly structured, possessing channels and voids [50]. These channels have well-defined spatial dimensions, making zeolites ideal as molecular sieves. These silicates, considering their interesting features, could have acted as primitive membranes, gettering agents or catalysts. Quartz is also a tectosilicate

prominent on early Earth that has familiar amorphous forms, e.g. fused quartz and fumed silica.

Beyond the scope of prebiotic chemistry, silica has been widely employed in applications where various characteristics such as a reacting or adsorbing surface and a large surface area are exploited. For many industrial chemical transformations, heterogeneous catalysts are preferable for reasons of longevity and minimal interruption to pre-existing process logistics compared to homogeneous approaches. Silica is a common support for neutral and cationic surface organo-metallic fragments that serve as the primary catalyst for an extensive and diverse suite of reactions, including metatheses and homologations [52]. Novel water purification techniques, where adsorption is preferred over chemical treatment have observed that nitrogen containing dye pollutants, common in plastic, textile and other industries, are readily removed from aqueous solutions by silica particles [53]. Innovation in industrial CO_2 scrubbing technology have for decades been driven by lowering costs and increasing longevity, thus sold-phase, rather than solution-phase, capture methods are increasingly attractive due to efficiency. Recent studies have shown that amine-tethered silica material has overcome issues of selectivity and diminished performance in high humidity conditions, typical of other porous materials [54]. Furthermore, silicas and silicates present as viable solid supports for catalysts by many distinct immobilization methods, including covalent anchoring and encapsulation [55]. Silica has been examined in model prebiotic reactions on numerous accounts demonstrating competitive adsorption of cationic over neutral amino acids due to electrostatic interactions [56], zwitterionic adsorption of glycine [57], and other interaction pathways.

1.2.3   Minerals Environments

An amphibious environment, one which experiences periods of hydration and dehydration, presents the most efficient method of concentrating organic reactants [40]. The evaporative environment is widely cited in model prebiotic reactions when employing "dry-down" conditions [40, 58-60]. The evaporative shore, pond, or comet pond [61] models are unique in that there is both elimination of water, a driving force towards condensation, and concentration of reactants. In the scenario where rain or tidal activity is the aqueous replenishing source, these events are expected to replenish the molecular feedstock and contribute to an extended progression of prebiotic chemical processes [12].

Marine hydrothermal systems have been considered an important potential environment for the origins of life [62-64]. The overarching concept is that these systems offer gradients in pH, temperature and reactant concentrations, all in the presence of potentially catalytic mineral substrates. Non-equilibrium conditions are continuously present and therefore allow access to chemistry that other environments do not provide [62]. Many of the minerals that are expected to have existed on early Earth, such as clays would likely be ubiquitous around such systems [65]. Acidic hydrothermal systems are specifically correlated with silicate minerals such as montmorillonite [66], a clay that has been implicated in various prebiotic catalytic reactions [67]. One of the large hurdles in prebiotic chemistry is the difficulty of creating solubilized and chemically available phosphate in a plausible manner. The phosphorylation of glucose has been reported in a simulated hydrothermal system in the presence of kaolinite [65]. However, there are drawbacks for a completely aqueous environment. Dilution of potential reactants, which is overcome in evaporative environments, requires clever work-arounds. Additionally,

condensation of reactants must be aided by activating agents or by some other mechanism, distinct from water removal by evaporation, if macromolecules are expected to form.

1.2.4   Mechanisms of Mineral Interaction

For heterogeneous chemical reactions, the interface, were molecules and substrate are in contact, is distinct from the respective bulk constituents. The surface may play a role in altering reaction rates, preferences between possible products, and other interactions. Mineral surfaces are not often terminated as the empirical formulations would suggest. Likewise, reactions in solution or within a dried film of organic molecules encounter a different environment than those same reactants at a heterogeneous interface. To probe surface-promoted reactions, it is necessary to understand the nature of these distinct interactions and the mineral characteristics that describe and account for them [68].

One of the most important characteristics of a surface in an aqueous, protic or otherwise ionic solvent is its charge state, as it may affect adsorption and reactivity. Mineral surfaces often present hydroxyls or uncoordinated metal or ionic centers, distinct from the bulk repeated cell. For simplicity, hydroxyl termination, common for silica, metal oxides and silicates, will be the model interfacial functionality. In contact with a solvent, these hydroxyls can disassociate their protons or become protonated, producing a respectively negative or positive surface charge. When the solution pH is below the pK_a for a certain motif, the hydroxyl will protonate, Eq. 1, and present as positively charged, likewise when the pH is above the site pK_a, the hydroxyls will deprotonate, Eq. 2, and present a negatively charged surface [69].

$$MOH + H \rightleftharpoons MOH_2^+ \qquad\qquad (1)$$

$$MOH \rightleftharpoons MO^- + H^+ \qquad\qquad (2)$$

For a mineral sample in the presence of water, the surface charge will vary as a function of pH. While the precise dependence must be obtained experimentally, the general form of the reaction is given in Figure 1-2. The pH value when the polarity of the surface charge switches is the metric that is most variable between various mineral types and samples. The point of zero charge (PZC) is the pH condition that is associated with a net neutral surface charge, or the region where the surface charge changes from one polarity to another [70]. A net neutral charge does not imply no charge, simply an equal representation of positively and negatively charged sites. The phenomena of a double-layer is related to surface charging and present in a heterogeneous environment [71]. It refers to two charged layers at the interface – the first being the native mineral surface itself, which will vary in polarity and magnitude depending on solution pH, and a second layer of oppositely charged entities, likely solvated ions or molecules, which are attracted the surface. The accumulation of these charge compensating bodies presents an effective surface charge opposite of that which would be predicted based on the solution pH and the mineral PZC.
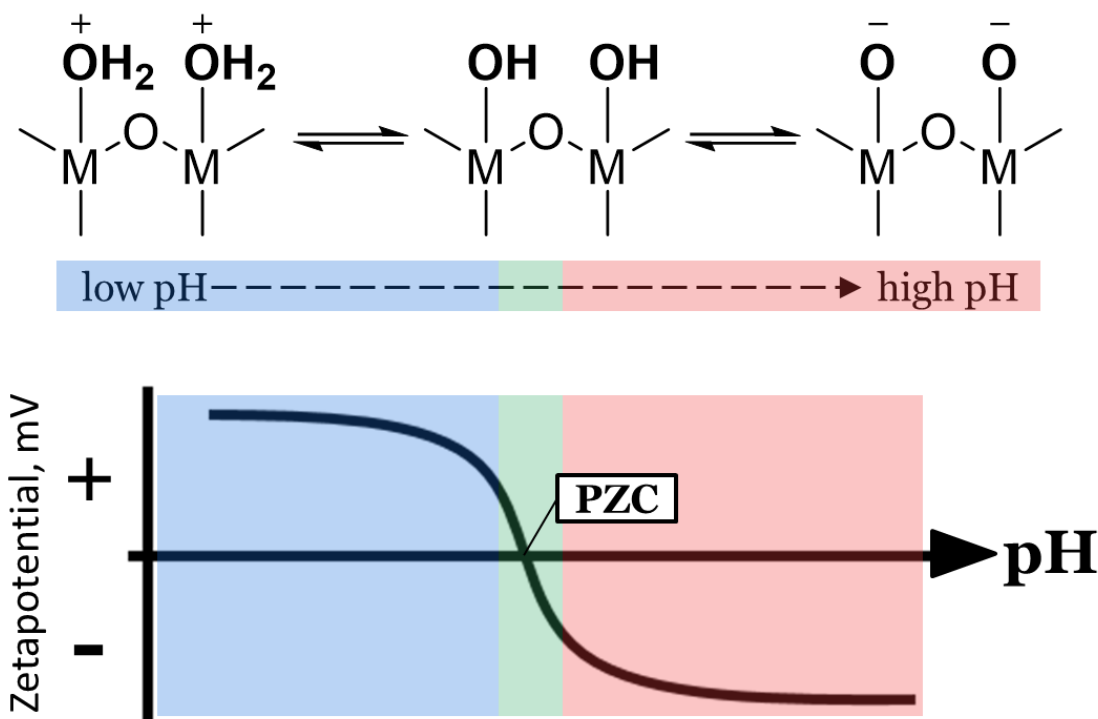
Figure 1-2   Form of the general pH vs. surface charge (Zetapotential) relationship and corresponding surface motif for hydroxyl terminated substrates (M represents a generic cation). The point of zero charge (PZC) is labeled and represent the pH of surface net neutrality.

The process by which molecules are adhered to a surface is broadly referred to as adsorption. Physisorption is mediated through weaker, highly distant-dependent forces such as Van der Waals and hydrogen-bonding. Chemisorption describes a much stronger interaction between a surface and sorbent, such as a covalent bond and most electrostatic attraction between oppositely charged chemical moieties. Adsorption is ultimately achieved by some favorable kinetic or thermodynamic process that is mediated through the aforementioned interactions and others, such as solvophobicity [44].

Factors which dictate the affinity of organic molecules towards adsorption include solubility, charge, polarizable functionalities, and steric properties [41, 44]. As far back as

Bernal, the concentration of reactants has been a stated role for minerals in prebiotic reactions. The molecular concentration of amino acids has been estimated to fall below mM levels [72], which is not sufficient for extensive chemical reaction to occur. Sorption in aqueous solution is a reversible process that is likely unable to achieve high local concentrations of reactants. Evaporation is a much more effective method for bringing reactant into close proximity, however this process is not unique to mineral environments, and structured minerals like clays might retain sorbents at higher rates [73]. Adsorption is only an initial step in the production of proto-biopolymers; reactions of the monomeric building blocks of life must occur and may be affected or catalyzed by the unique chemical characteristics of a mineral surface.

1.3   Mineral Interaction with Polypeptides

Peptide bond formation has been the subject of many studies utilizing mineral substrates as potential catalysts by various degrees and mechanisms of chemisorption[41]. Many experiments have collectively demonstrated that there is some positive effect on the rate, length or conversion magnitude for amino acid poly-condensation reactions due to the presence of a mineral substrate. However, variation in experimental conditions, including temperature, reactant ratios, mineral pre-treatments, solution pH, reaction duration and deposition method have obscured, in many cases, a clear relationship between mineral identify and catalyst efficacy.

Kitadai et. al. has examined the poly-condensation of glycine within an impressively large nine mineral sample set, including Ti, Si, Al and Fe oxides [59]. Here, all samples were subjected to identical conditions of unbuffered glycine solutions with

reactions proceeding at 80 °C in an evaporative environment. Comparing total yields of glycine incorporation into some oligomeric system (G_n, $n>1$) and length of oligomers, this report found that both the rutile and anatase phase of TiO_2 far outperformed other oxides, with silica performing the worst. For the TiO_2 samples, linear products of 5 residues in length were detected, with the cyclic dimer DKP as the most dominant product. In contrast, silica yielded ~10x less glycine consumption and produced only dimers, mostly in the DKP form. Still, control reactions with no mineral present far underperformed even silica, which demonstrates that all examples of mineral inclusion facilitate amide catalysis to some degree. The activation process was inferred to involve the positively charged surface for TiO_2 mineral phases. Electrostatic binding between a positively charged TiO_2 site ($\equiv Ti^+$ or $\equiv Ti–OH_2^+$) and the glycine carboxylate (COO^-) increased electrophilicity of the glycine carbonyl carbon. The poor performance of silica was attributed to its inability to support non-zwitterionic species or stabilized the glycine carboxylate.

The condensation of glycine on a silicate clay mineral, montmorillonite, has been studied by Fuchida et. al. [74]. During dry-down reaction at 150 °C, ~15% of glycine was in some way incorporated into non-monomer systems, with the cyclic DKP coming as the most dominant product. In the absence of montmorillonite and for the subtracted reacted in the presence of water, peptide products were not observed. Glycine was found to adsorb in the zwitterionic state, as the pH ~6 in the unbuffered suspension. By infrared analysis, an ester linkage with the surface was not detected, so this was not considered a motif that contributed to peptide formation. While clays have abundant Lewis acid and base sites, interaction between the protonated amine of the zwitterionic glycine and the negatively charged Lewis base sites on the surface were identified as the catalytic interaction.

15

The mechanism of amide formation on certain oxide and hydroxide materials has been described by Martra et. al. [75, 76]. Evidence for the amidation of a formate ion adsorbed on the surface of a TiO_2 substrate, at ~50 °C has been presented via infrared and mass spectrometry analysis. Formic acid, vapor deposited onto the TiO_2 surface in a non-aqueous environment displayed anionic adsorption, similar to amino acids in zwitterionic states. Only after dosing levels exceeded the approximate monolayer coverage did the carboxylic form of the molecule persist, inferring that interaction with the surface was responsible for the interfacial formate species. Subsequent dosing of a alkyl primary amine resulted in a decrease in carboxylate signal and an increase in amide carbonyl signal, suggesting the transformation from one to the other. The proposed mechanism relies on the electrostatic interaction between uncoordinated Ti^{4+} ions and the formate. The Lewis acid sites are expected to withdraw electron density from the carbonyl carbon, imparting electrophilicity sufficient to participate in nucleophilic attach by the amine and implicating surface carboxylates in amide bond promotion [75].

In a similar system which employs vapor phase deposition, glycine was studied and found to oligomerize on TiO_2, SiO_2, but not for hydroxyapatite $Ca_5(PO_4)_3(OH)$ [76]. A similar adsorption state for glycine on TiO_2 was observed and a possible indication of a "surface mixed anhydride," otherwise known as a silyl-ester, was identified at 1760 cm^{-1} but associated with a specific hydrogen bonding motif instead. At a reaction temperature of 130 °C, glycine oligomers exceeding 11 residues in length where observed for both oxides. SiO_2 was significantly less reactive than TiO_2, but both yielded peptide products, whereas hydroxyapatite did not, therefore implicating the oxides as peptide catalysts.

The formation of amide linkages catalyzed on silica has been modelled by first principals by Ugliengo et. al.[77-79]. The simulation of glycine and ammonia, as a surrogate for a second glycine, reaction determined that the silyl ester (≡Si–O–(C=O)–R), Figure 1-3, would be thermodynamically unstable with respect to the non-bound surface-glycine conformation. It was also determined that the esterified carbonyl was only moderately activated towards amide formation (nucleophilic attack) and that water is a necessary participant, serving as a proton transfer agent [77]. Though the silyl-ester is energetically disfavored in studied conditions, it may be accessible in far from equilibrium conditions, perhaps during a dry-down process, and would indeed result in a hypsochromic shift, relative to the carboxylic acid vibrational frequency [78]. Investigation of silica catalyzed amide formation with glycine using computational and infrared spectroscopic techniques have added several qualifications to the previous findings. Non-hydrogen bound silanol pairs have been determined as necessary for catalytic glycine adsorption, by supporting the co-existence of glycine in both the uncharged and ionic forms, leading to amide formation [79]. Additional computational work as agreed that silica may stabilize neutral glycine via interaction with multiple silanol sites [80].
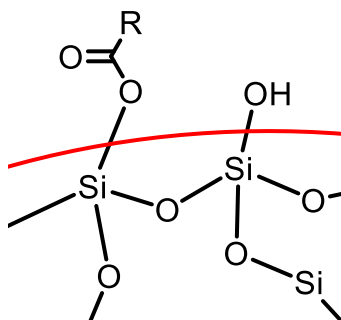
Figure 1-3 **Molecular depiction of a silyl-ester or "surface mixed anhydride" [77] between a silica substrate and some molecule with a carboxylic acid. The horizontal**

red line is provided to delineate the bulk silica features (SiO₂) from the non-stoichiometric surface functionalities, e.g. Si–OH.

In summary, while silica has been determined to facilitate amide formation to some degree, the reactions produce mainly cyclic DKPs and few linear oligomers past dimers. Additionally, if peptides are catalyzed by the surface, it is through non-covalent adsorption of glycine in the neutral or anionic state, due to the disfavored formation of a surface silyl-ester.

1.4   Depsipeptides

1.4.1   Overview

Modern proteins are comprised purely of amino acids (AA) from a specific set, optimized for the host physiology. As previously mentioned, p*rogenimers*, ancestral proto-biomacromolecules, could have contained non-canonical residues or linkages. Depsipeptides are a robust and plausible protein progenimer which have been recently discussed in model prebiotic contexts [33]. Distinct from peptides, Figure 1-4a, the distinguishing characteristic of depsipeptides are that both amide and ester linkages are included in their backbone, Figure 1-4b. The term depsipeptide is adopted from medical science, where this class of molecule continues to be the subject of new drug therapies, such as histone deacetylases inhibition [81] and HIV treatment [82].

18
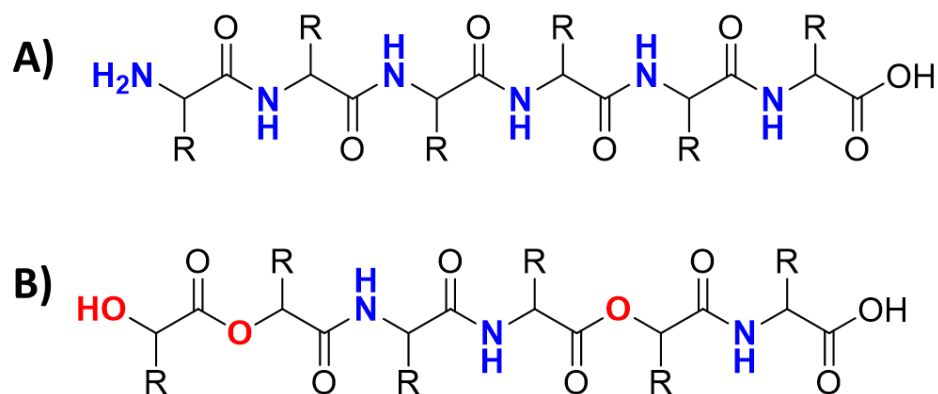
Figure 1-4   Example of an A) oligopeptide and B) depsipeptide 6-mer. For the depsipeptide, some number of the amide linkages from the oligopeptide have been replaced with ester linkages.

In a prebiotic context, the component of depsipeptides are amino acids and hydroxy acids (HA), Figure 1-5. Hydroxy acids should not considered an exotic or obscure prebiotic reactant, rather they can be synthesized by the same model prebiotic reactions that have been used to produce amino acids. Summarized in a review that revisited the original Miller-Urey spark discharge experiments with gaseous aldehydes, ketones, cyanide and ammonia, amino acid synthesis is favored in neutral to basic conditions, while the ratio of HA:AA can be in excess of 1000 in acidic conditions [83]. Here, the Strecker mechanism produces amino acids, and α-hydroxy acids are produced via the cyanohydrin mechanism. Each depsipeptide monomer possess a distinct nucleophilic moiety and therefore produces a distinct bond in a condensation reaction; amino acids produce amide linkages, while α-hydroxy acid produce ester linkages. The monomers also differ in the pK_a of their electrophilic carboxylic acid group; for an amino acid such as alanine, pK_a (alanine) = 2.34, while the analogous α-hydroxy acid is less acidic, pK_a (lactic acid) = 3.86. The amide and ester linkages in depsipeptides also possess distinct hydrolytic stabilities in heated acidic conditions, with esters cleaving and amides persisting much longer [32]. This distinction

allows for recycling of α-hydroxy acid residues, rearrangement of oligomers, and a more efficient exploration of sequence-space in a multi-monomer co-oligomerizing system, which is advantageous for the emergence of function.
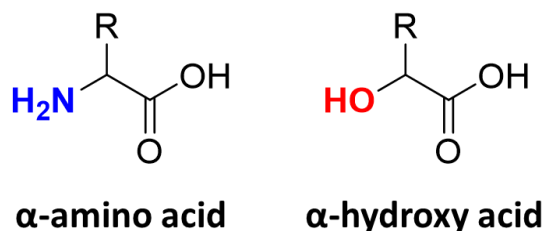
Figure 1-5   General forms of α-amino acids and α-hydroxy acids, the monomer units in depsipeptides.

1.4.2   Ester-Mediated Amide Formation

Most prebiotic systems require an evaporative environment to drive the condensation reactions towards oligomerization. While direct amide formation can occur in this manner, the temperature required to achieve this transformation with practical yields for reasonable reaction durations is typically considered too high within some prebiotic models. Esters, however, are able to form at much more moderate temperatures, near 65 °C [32]. In a depsipeptide system, the electrophile for amide formation is a carbonyl carbon in an ester motif, not a carboxylic acid [33]. While carboxylic acids and an esters have similar leaving group basicity and therefore reactivates for nucleophilic attack, esterification likely does contribute to a more electrophilic carbonyl carbon, and certainly avoids a deprotonated carboxylate, which is considered a poor electrophile due to the localized negative charge. For this reason, ester formation always precedes amide formation, and has been demonstrated as a thermodynamically favored route compared to direct amide formation [84].
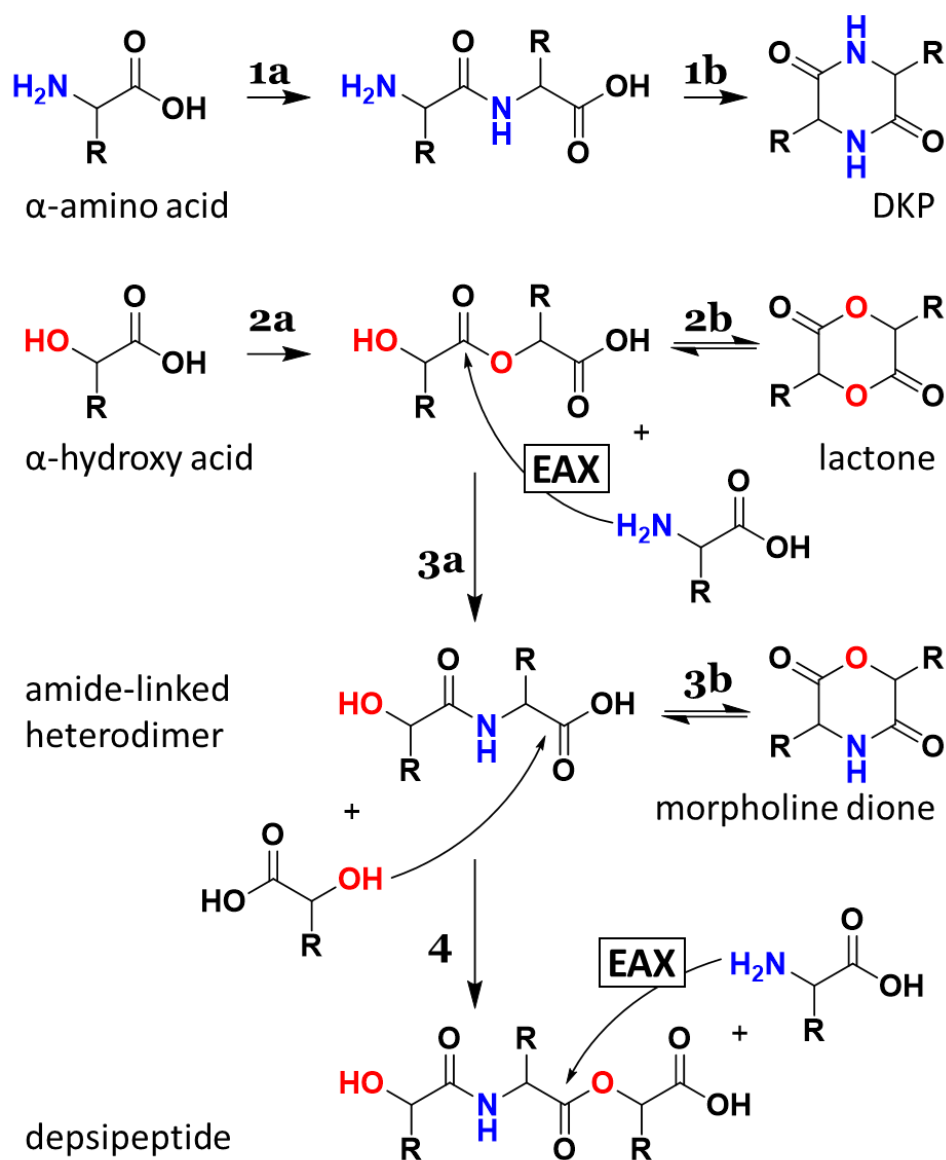
Figure 1-6 **Scheme depicting the formation of depsipeptides from α-hydroxy acids and amino acids.**

A mechanism for depsipeptide formation under evaporative, heated and unbuffered conditions is presented in Figure 1-6. Considering a reaction of only amino acid species, production of the linear dimer via direct amide formation (1a) is universally observed. However, for most reactions, the major product is the cyclized dimer (1b), referred to as a diketopiperazine (DKP). This cyclization is not considered reversible within these

conditions, so DKP becomes a sink for starting material, as further amino acid addition and linear trimer production is not accessible. In contrast, α-hydroxy acid species are able to esterify (2a) and reversibly cyclize to the dimeric lactone form (2b), such that poly-esterification can be achieved at moderate temperatures and in laboratory time scales. When amino acids and α-hydroxy acids are reacted concurrently, ester bonds are sites of sufficient electrophilicity such that amide formation can proceed (3a). In this process, the C-terminus α-hydroxy acid residue is displaced or *exchanged* for an amino acid residue. For this reason, this mechanism is often referred to as Ester-Amide eXchange (EAX), though the process may also be described as ester aminolysis (EAX), as the ester is cleaved by an amine moiety, leading to the formation of an amide bond. The EAX product from an α-hydroxy acid-dimer and an amino acid is an amide-linked heterodimer (HA–AA). Similar to DKPs or lactones, this heterodimer is also likely to cyclize (3b) and form a morpholine-2,5-dione. While as a DKP, this form was a reactive "trap," the ring-closing ester is both susceptible to hydrolysis in addition to being an activated site for EAX. If another ester is formed at the C-terminus of the amide-linked heterodimer (4) a simple depsipeptide is formed with a sequence HA–AA–HA. If another ester is present, a second amino acid addition can proceed via EAX and make the first contiguous amino acid pair in the depsipeptide sequence, HA–AA–AA. The last steps in this process can be repeated in addition to multiple α-hydroxy acid additions. With these pathways available, depsipeptide products always have a α-hydroxy acid residue at the O-terminus (analogous to N-terminus for peptides), and can have amino acid and α-hydroxy acid residues in different abundances and arranged in different sequences.

1.5   Objectives

This thesis will discuss the native character of minerals and the results of interactions between organic molecule and mineral surfaces in the context of the chemical origins of life and prebiotic chemistry. CHAPTER 2 will demonstrate the effect on depsipeptide composition due to the presence of silica. CHAPTER 3 will describe the mechanism by which a silica surface can facilitate ester aminolysis. CHAPTER 4 will examine a more diverse cohort of mineral substrates in the context of surface-ester aminolysis. CHAPTER 5 will explore nucleotide stability to electron-induced damage as a possible factor in the evolutionary path from RNA to DNA. Lastly, CHAPTER 6 will summarize major findings and present several recommendations for continued research regarding depsipeptide and proto-peptide formation on mineral surfaces.

CHAPTER 2. DEPSIPEPTIDE FORMATION IN THE PRESENCE OF SILICA[1]

2.1 Summary

The work presented here is the first account of a productive depsipeptide reaction interacting with a mineral substrate in a heterogeneous system. Formation of alanine and glycine oligomers in films produced by drying aqueous mixtures of lactic acid and silica nanoparticles have been studied under plausible prebiotic conditions. The addition of silica results in alanine or glycine enrichment in the polymers. Oligomerization proceeds via ester-mediated peptide bond formation, ester aminolysis, in an acidic evaporative environment at temperatures as low as 85 °C. For both amino acids studied, the dominant species produced in the presence of silica and lactic acid are rich in amide bonds and ester deficient. At higher temperatures, glycine and alanine oligomers contain only a single hydroxy acid residue conjugated to the N-terminus. Similar product distributions occurs with silica is pre-reacted with lactic acid, suggesting a catalytic role of a functionalized surface. This work highlights the role minerals may have served in transitioning from oligomers with both ester and amide linkages (depsipeptides) to peptides in a prebiotic context.

2.2 Background

As discussed in the introduction α-hydroxy acids (HA) can act as molecular catalysts for the formation of amide bonds between amino acids. This reaction is of potential prebiotic relevance since i) the reaction proceeds with amino acids that are not pre-activated, at temperatures as low 85 °C, and ii) α-hydroxy acids are also considered plausible prebiotic molecules, as they are found together with amino acids in meteorites. This system is of considerable interest because both amino acids and α-hydroxy acids are also among the products of spark discharge experiments and are therefore considered plausible for prebiotic reactions [85, 86]. Upon drying and heating, to be referred to as dry-downs, ester bonds are formed between the nucleophilic hydroxyl groups of α-hydroxy acid residues and the electrophilic carboxylic acid groups present on both α-hydroxy acids and amino acids. Subsequently, these esters facilitate amide bond formation via nucleophilic attack by the amino group of an amino acid. The α-hydroxy acid and amino acid reactions therefore produce mixed HA/AA oligomers, called depsipeptides, which contain both amide and ester backbone linkages. The mechanism of chain elongation proceeds via an ester aminolysis reaction and is discussed in detail in the introduction. The resulting depsipeptides are hypothesized to be ancestral forms of polypeptides, i.e. protein progenimers. If this hypothesis remains valid as an origins of life theory, the inclusion of increased amino acid content for depsipeptides, and the further transformation to purely amino acid-containing poly-peptides, would have been an important chemical evolution pathway. With this perspective, we sought a plausible prebiotic mechanism to enhance peptide content in the α-hydroxy acid-mediated amide forming reaction.

It has been hypothesized that minerals interacting with amino acids in an evaporating or tidal pools on the prebiotic Earth could have acted as catalysts for peptide formation [87]. There have been many tests of this concept, with a variety of amino acids, minerals, and reaction conditions, resulting in various degrees of peptide bond formation [29, 88]. Most work has been carried out with glycine, the simplest amino acid, which is among the easiest to polymerize of the twenty canonical amino acids. Mineral catalysed polymerization studies with non-glycine amino acids (i.e., alanine and more complex amino acids) have generally been less successful, mostly being limited to di-peptide products in low yields. Moreover, a detailed and generalized understanding of how minerals facilitate or alter the oligomerization of amino acids has not reached a consensus, especially considering the numerous distinct types of minerals [89, 90].

As discussed in CHAPTER 1, studies of amide bond formation involving carboxylic acids and amines on metal oxides, such as TiO_2, have shown evidence of surface carboxylates as an activated electrophilic species [75, 91]. Thus, mineral-catalysed reactions and the above-mentioned α-hydroxy acid-catalysed reaction may act through a common mechanism of ester aminolysis (EAX). Given this background, the potential impact of a mineral-like substrate on depsipeptide formation in the α-hydroxy acid-catalysed amino acid polymerization reaction has been investigated. The proceeding report covers investigations of depsipeptide formation in the presence of fumed silica using the HA + L-lactic acid (LA) and either L-alanine (A) or glycine (G). Fumed silica was chosen as a model substrate to represent a broad range of quartz and silicate minerals.

2.3   Experimental

The LA/A or LA/G depsipeptide formation experiments, with and without the addition of silica, were conducted in parallel to directly compare the product distributions. Fumed silica was added (100 mg/mL) to 1:1 LA/A or LA/G mixtures (0.25 mL, 100 mM solutions [92]). The starting reagents and standards include: L-Lactic acid (LA), L-alanine (A), glycine (G), tri-glycine, fumed silica powder, (CAS: 112945-52-5) and LC-MS grade water, acetonitrile and formic acid were purchased from Sigma-Aldrich. The LA-G amide-linked heterodimer cassette was synthesized flowing a published procedure [93].

Unless stated otherwise, reactions were conducted by a single step "dry down" phase in uncapped glass vials and incubated for durations ranging from 0.25 hours to 3 days. Incubation occurred in a temperature-controlled oven, in ambient atmospheric conditions, at 85 °C or 125 °C. The silica absent control reactions proceeded under otherwise identical conditions, without silica. Reaction mixtures were unbuffered and therefore at a pre-reaction pH 2.8, primarily owing to the carboxylic acid functionality of the lactic acid. The final pH becomes less acidic based on the extent of LA oligomerization, which increases with time and temperature. Post-reaction pH measurements indicated pH: 4-5 for reaction conditions presented here. Post-reaction, samples were rehydrated with water at room temperature and briefly sonicated. Samples were subjected to centrifugation to remove silica particles and the supernatant was collected for analysis by single quadrupole mass spectrometry (MS) or proton magnetic resonance spectroscopy (NMR).

2.4 Results and Discussion

2.4.1 Mass Spectrometry of Depsipeptide Products

Mass spectrometry (MS) analysis is a very intuitive approach to understanding the depsipeptide system. In a homo-polymer, with only one monomer species, MS resolves oligomers of different lengths by the mass to charge (m/z) difference associated with the molecular weight of one residue minus a H_2O due to the condensation nature of the oligomerization process. During the co-reaction of amino acids and α-hydroxy acids, oligomers of varying length and composition are produced. Though there are 2 monomers present, the fact that they differ in molecular weight allows for unique compositional assignments to be made for each MS peak observed. For every n-mer produced in a depsipeptide reaction, there are $n+1$ combinations of amino acid and α-hydroxy acid for that n-mer to contain. The oligomer can be either completely amino acid composed, completely α-hydroxy acid composed, or contain all available ratios of AA:HA in between. Therefore, for every n-mer, there is a distribution of compositions which can be discerned via MS. This metric of oligomer composition has not been available for previous investigations of single-amino acid proto-peptide reactions and is therefore an interesting and new approach to discussing the role minerals can have in a prebiotic model.

2.4.1.1 Sample Preparation

Electrospray ionization (ESI) mass spectrometry was conducted on an Agilent 6130 single quadrupole mass spectrometer and a Waters ACQUITY QDa single quadrupole ESI mass spectrometer. All samples were prepared in water and introduced to the MS via direct injection of 5 µL and analyzed in negative ion mode, such that the [M - H]- ion and mass is the expected product. Regarding Figure 2-2 and the oligomer composition distributions, a nonparametric hypothesis test was employed to distinguish the composition distributions of both conditions, with and without silica. This confirmed that the two distributions are

significantly distinct, and therefore the G enrichment due to the presence of silica, beyond a 95% confidence interval, p=0.049.

2.4.1.2   Reactions of Alanine and Lactic Acid with Fumed Silica

The inclusion of alanine as an amino acid in this depsipeptide system in important for the simple reason that it is not glycine. While glycine experiments are among the most popular for model prebiotic peptide experiments, the reactivity of alanine is closer to that for the many other amino acid, while glycine is typically more reactive. Therefore, production of long (greater than 3 units in length) products in the A+LA+silica depsipeptide system is noteworthy just as a non-glycine system.
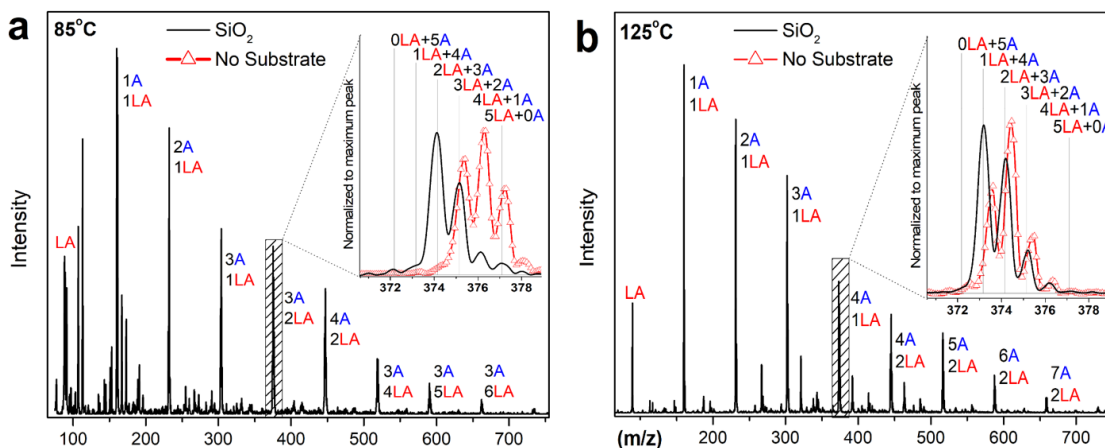
Figure 2-1   ESI mass spectra showing depsipeptide formation in an LA/A system in the presence of silica after A) 3 days of incubation at 85 °C and B) 20 h of incubation at 125 °C. The labels indicate the dominant species for each n-mer. The insets illustrate differences in pentamer product distributions between the LA/A reactions carried out in the presence of silica and samples without silica.

Analysis of products from the silica+LA+A system, incubated in the dry state for 3 days at 85 °C in Figure 2-1a, reveals the range of oligomer lengths. Oligomers extending to 9 residues in length are considered very productive and far exceeds other experiments

with silica in non-depsipeptide systems [59]. The inset provides a representative comparison of the 5-mer composition distribution between reactions with and without silica, demonstrating that the dominant species are distinct. This comparison is an example of the primary effect that can be observed between the two conditions for depsipeptide reactions. In the presence of silica, depsipeptide products contained greater amounts of amino acid. The connectivity of these amino acid residues will be discussed in the NMR section below

Reactions were conducted at 125 °C to assess if oligomer composition disparities in the presence of silica persisted at a temperature known to facilitate amino acid oligomerization [94]. At this temperature (Figure 2-1b), the LA/A system produced oligomers containing up to 7A and 6A residues as the dominant species with and without silica, respectively. The increase of incubation temperature, from 85 °C to 125 °C, results in a substantial increase of peptide character for both the substrate absent and silica containing conditions. Despite accessibility of both direct amide formation and ester aminolysis, oligomer composition remains distinct and amide enriched for silica samples at both temperatures. This implies a substrate-related mechanism distinct from the bulk EAX process is occurring during oligomerization and that this substrate-related mechanism results in greater amino acid inclusion.

2.4.1.3   Reactions of Glycine and Lactic Acid with Fumed Silica

To contribute to the diversity of amino acids studied and because oligo-G is more soluble than oligo-A peptides, G was chosen for a quantitative analysis of oligomer yields, lengths and compositions. While MS results from the A+LA system are convenient to

display as minimally altered mass spectrum, i.e. similar to the instrument output, G+LA data is not as well-suited. The mass difference between A and LA is 1 amu, so the oligomer composition series are adjacent in m/z space. However, G and LA differ in molecular weight by ~15 amu, so the most efficient method of communicating MS results is with a histogram. The adjacent m/z values for the A+LA system are replace with the adjacent number of LA residues space, which is taken directly from the same type of mass spectra.
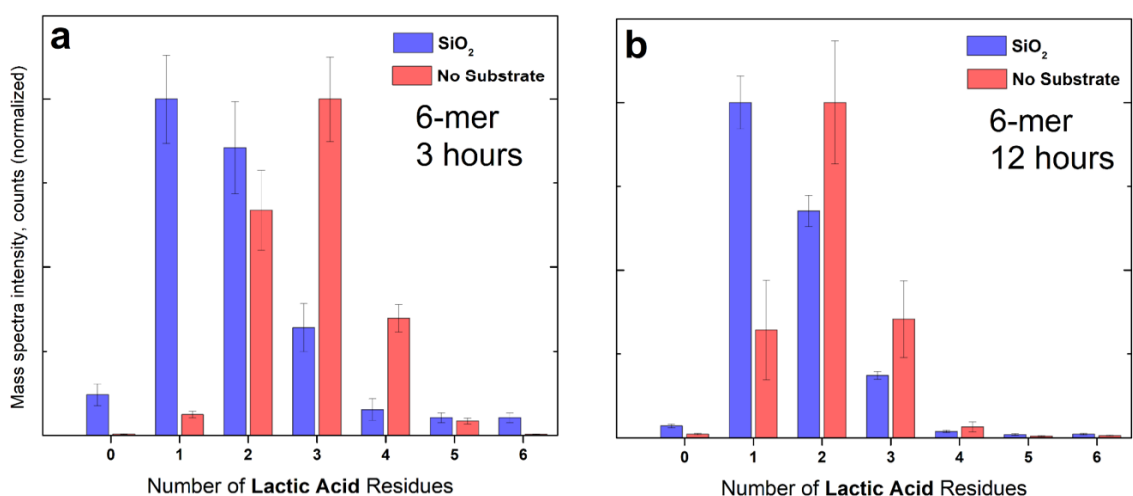
Figure 2-2   Distribution of hexamer oligomer composition abundances from a 1:1 LA/G system reacted at 125 °C, with and without silica, extracted from ESI-MS spectra. The distributions for this representative mid-length oligomer (hexamer) are distinct for both A) 3 and B) 12 h samples. Although product distributions shift, silica samples remain G enriched.

The normalized 6-mer abundances from 125 °C data are summarized in Figure 2-2 as representative for the complete set of n-mers produced. While all composition varieties are present, the dominant composition for the 6-mer in the silica containing sample follows as 1LA+(n-1)G, with the longest detected oligomers surpassing 10 contiguous G residues with still only 1 LA residue included. These 1LA-residue oligomers contain no ester linkages, as the LA resides at the N-terminus. Substrate-absent experiments produce

extensive depsipeptide diversity and length, but less contiguous G content and much higher LA content, especially at short incubation times. In LA and substrate absent experiments, oligo-G was observed up to 9-mers at 125 $^{\circ}$C but not 85 $^{\circ}$C, consistent with previous work [94, 95]. Amino acid enrichment also occurs in LA/G systems at 85 $^{\circ}$C in the presence of silica. Both conditions shift towards less LA incorporation, greater amino acid abundance, with time, yet the populations remain distinct, though to a lesser degree. This observation suggests that there is a distinct process occurring within the two conditions and confirms amino acid enrichment to somehow due to the presence of silica.
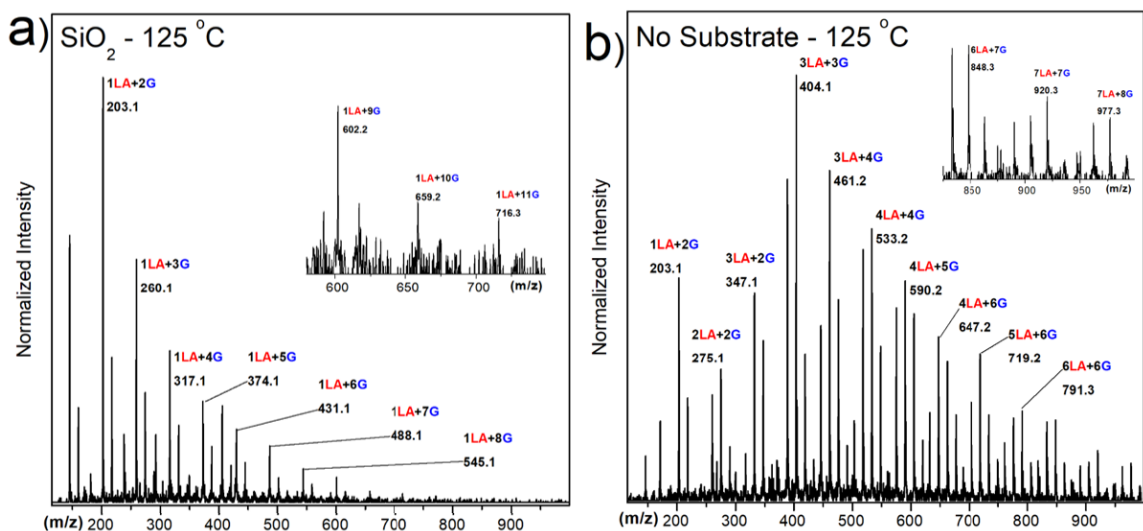
Figure 2-3   Mass spectra of depsipeptide formation for a glycine and lactic acid system, after 3 hours of incubation at 125 $^{\circ}$C, in the a) presence of silica and b) absence of silica.

Examination of the full MS for the LA+G system can provide a further insight as for the extent to which amino acid enrichment is observed in the presence of silica. The mass spectra of depsipeptide formation for a G and LA, after 3 hours of incubation at 125 $^{\circ}$C is shown in Figure 2-3, in the a) presence of silica and b) absence of silica. The dominant species for each n-mer is labeled with its composition and mass. At 125 $^{\circ}$C, silica

containing samples are G enriched compared to silica-absent conditions. When compared to products of the A+LA system, G depsipeptides contain even more amino acids at maximum length, which is expected considering the general reactivity of G and solubility of oligo-G. At this elevated temperature, silica-containing samples majorly produce oligomers containing only one LA residue, with up to 11 G residues. At the higher oligomer lengths, the diversity in composition appears to decline, such that 2LA or 3LA species are not of sufficient abundance to be identified, despite these products existing for the 4-,5-, 6-mers. The G in oligomers with only a single LA residue are contiguous with the LA residing at the N-terminus. In a drastically distinct distribution, the silica-absent control samples produce a greater diversity of depsipeptide compositions, with increased LA abundance, many of which possess a LA:G ratio near 1. While the control condition results in overall longer oligomers, detecting 15-mers and likely longer species beyond the range of the instrument, only up to 8 G residues were found for any one species. One the basis of G content alone, this is still considered a reduced G content. However, for the oligomers with multiple LA residues, it cannot be assumed that they are all located at the termini. Instead, it is near equally likely that internal LA exist between shorter groups of contiguous G. In any hydrolysis scenario, such as a hydrated phase in environmental cycling, those esters will cleave and the population of oligomers will narrow and contract towards shorter products.
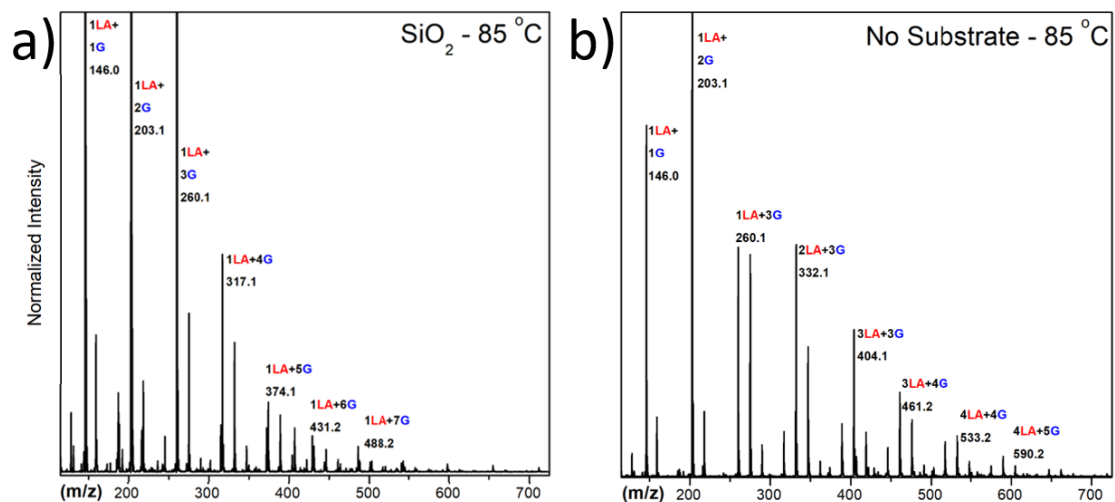
Figure 2-4 **Mass spectra of the glycine and lactic acid system, after 3 days of incubation at 85 °C, in a) the presence of silica and b) the absence of silica.**

At lower temperatures (Figure 2-4), the dominant products within silica containing samples remain as a single LA species, though the maximum length of oligomers is decreased compared to the 125°C experiments. A similar trend is observed for silica-absent samples at both temperatures; the LA:G ratio is near 1. At 85°C, silica-absent samples possess less G content than all other conditions discussed. Similar to the A+LA reactions, temperature is a major contributor to amide formation and poly-condensation of any molecules.

Observing the behavior of various species as a function of time is imperative for understanding how silica leads to amino acid enrichment. By integrating extracted ion chromatograms corresponding to the mass of a specific product species, traces of abundance over time can be compared for both conditions. Whereas Figure 2-2 is a snapshot in time of the composition distribution, Figure 2-5 (solid line, left axis) shows a progression over the reaction duration for two distinct 1LA species. Additionally, Figure

34

2-5 (dashed line, right axis) denotes the composition of the dominant species for the n-mer discussed for comparison. As shown in Figure 2-5a, though the heterodimer is the dominant species under both conditions, the abundance as a function of time is quite distinct. This must be due to the presence of silica and suggests that a mechanism distinct from that of the control experiments. Figure 2-5**b** illustrates the abundance of the 1LA+5G oligomer as a function of time. Unlike the dimer, the maximum abundance occurs within the same temporal order of magnitude for both conditions. The dominant 6-mer composition for silica containing samples is consistently the 1LA+5G, however this is not the case for the mineral-absent control. The G enrichment and progression from 4LA+2G to 2LA+4G for a mineral-absent reaction is shown in Figure 2-5**b** (dashed line). The silica-absent sample does not reach the same degree of amino acid enrichment even after 48 hrs.
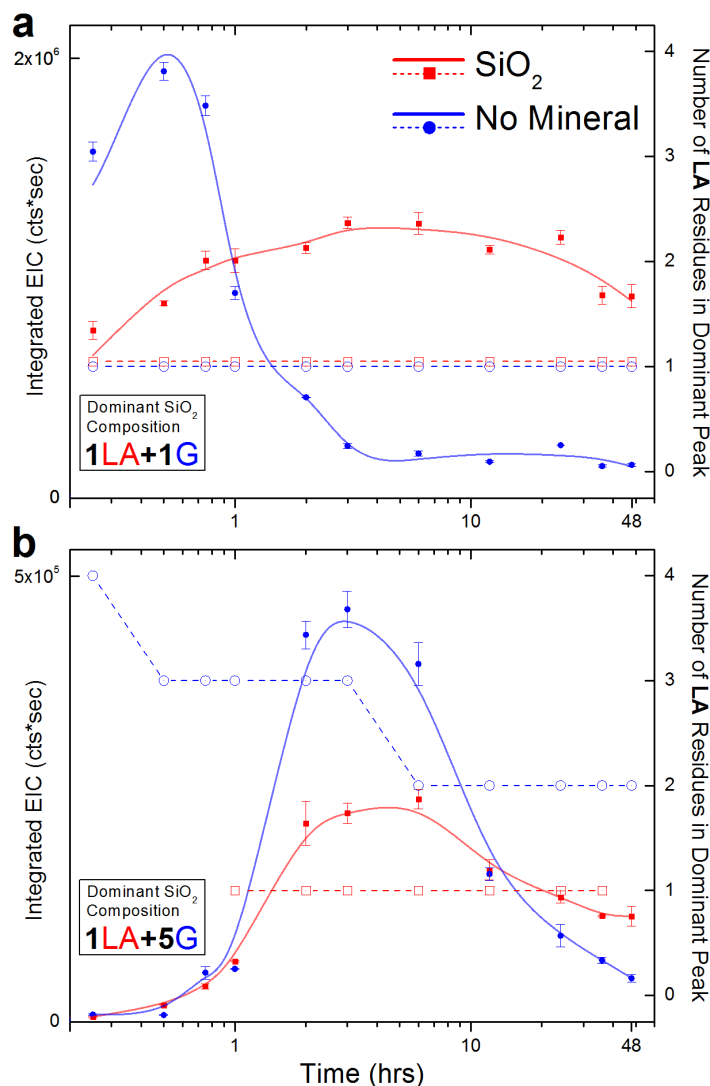
Figure 2-5 **Integrated extracted ion chromatograms (solid line is a moving average for visualization), corresponding to the 1LA+*n*G species, were collected as a function of time and compared for both conditions. Included is the corresponding composition of the dominant species for each condition (dashed). The a) amide-linked heterodimer and b) 6-mer are representative of the behavior of shorter and longer oligomers for each condition.**

2.4.1.4   Reactions of Amino and Fumed Silica without α-Hydroxy Acids

The introduction highlighted several accounts of pure amino acid polymerization

in the presence of silica. The experiments where products included longer chains, beyond

trimers, employed elevated reaction temperatures, considered to be above 85 °C in this context. Presented in Figure 2-6 is the reaction of glycine a) with and b) without silica are included from a reactant solution prepared at 100 mM, with silica added at 100 mL/mg. In both conditions, poly-glycine is formed within the timescale reported for other depsipeptide experiments. At elevated temperatures, direct amide formation is expected, however, long contiguous G chains are still achieved in the G+LA+silica depsipeptide system (Figure 2-3) and may be facilitated by the ester-aminolysis mechanism.
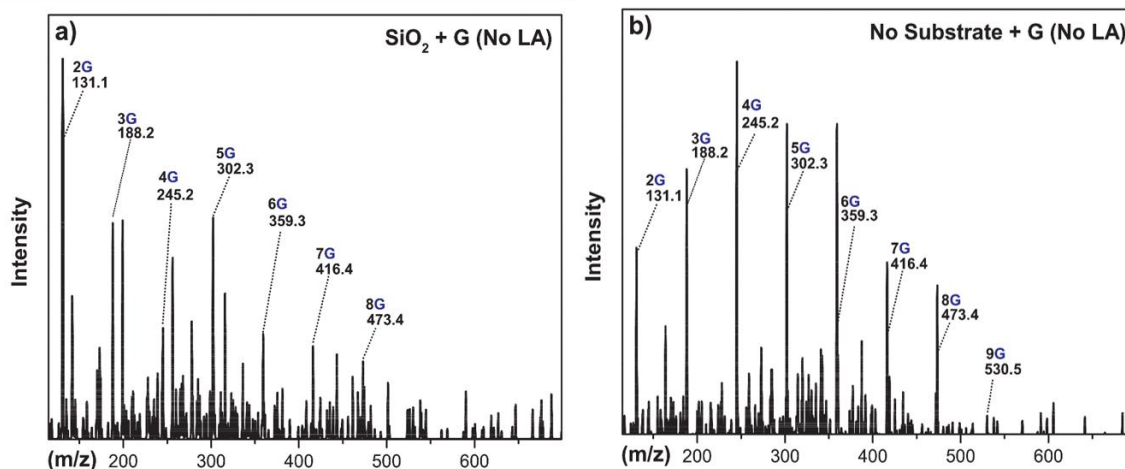
Figure 2-6 – Mass spectra of glycine only dry-downs at unbuffered pH 5.8, incubated at 125 °C for 20 hours.

2.4.2   NMR of Depsipeptide Products

Depsipeptide composition was determined explored with mass spectrometry analysis, but only minimal inferences regarding sequence could be determined, such as the N-terminus LA residue (referred to as the O-terminus). To investigate depsipeptide connectivity, NMR analysis has been employed to identify multiple bonding motifs, from which inferences of residue neighbour identities can be made. NMR is also advantageous

as it can easily be used for product quantitation when samples are prepared in a carful manner and a reference is used. Presented here is a full NMR analysis of depsipeptide products that assigns bonding motifs and reaction yields based on standards, post-reaction processing and previous work [33].

2.4.2.1   Experimental

NMR spectroscopy was conducted on a Bruker Avance III-500 spectrometer (500 MHz). Spectra were collected over 32 scans with a 10-second relaxation delay. All NMR samples were prepared by rehydrating dried reaction material in a deuterated aqueous phosphate solution buffered to pH 7. An external standard capillary insert, 1 mm in diameter, containing 50 mM potassium hydrogen phthalate (KHP) was used to calibrate all samples. The KHP protons appear at 7.40-7.64 ppm. All spectra were scaled to have an equivalent integrated signal for the external standard, such that all reported NMR spectra could be quantitatively compared due to identical sample preparation. An exception to quantitative comparison exists for spectra that are for specific comparison and are shown off the zero-count baseline in supplemental figures below. The values presented in Table 2-1 are yields calculated by comparing the integrated NMR spectral regions of those motifs with the total glycine signal from each spectrum.

The ester-selective hydrolysis procedure entailed permitting the samples to remain at room temperature in the pH=7 buffered solution for 7 days. The low temperature assured the cleavage of ester bonds, while maintaining amide bonds.

2.4.2.2   Depsipeptide Reaction Products

^{1}H-NMR spectroscopy confirmed different LA and G residue connectivity for oligomers produced at 125 °C in reactions with and without silica. Expanding on previous NMR assignments for LA/G depsipeptides,[93, 95] five unique G methylene proton resonances were identified by comparison with standards and treatment by a mild hydrolysis procedure. The hydrolysis left amide linkages intact while the more labile ester bonds were cleaved.
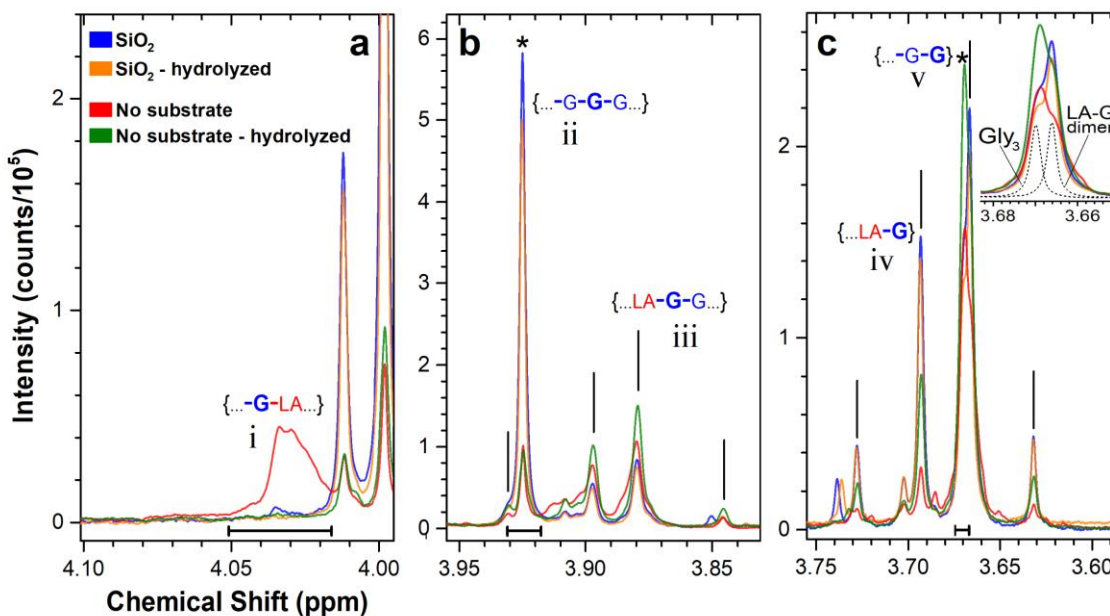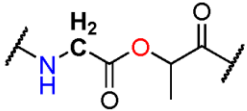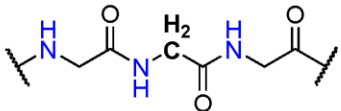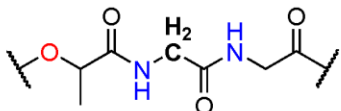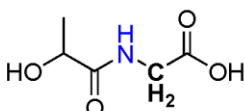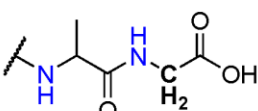
Figure 2-7 – ^{1}H-NMR spectrum of the LA/G oligomer forming system after 20 h of incubation at 125 °C. Included are samples of reactions with and without silica both before and after an ester hydrolysis procedure. The regions show glycine in A) an ester-linked motif, B) internal amide-linked motifs, and C) C-terminus amide-linked motifs. The vertical lines denote sets of diastereotopic protons. The inset includes spectra from standards of tri-glycine and the LA–G cassette for comparison. All spectra are scaled to an equivalent external capillary standard for quantitative comparison.

The broad resonance **i** at 4.03 ppm (Figure 2-7a) corresponds to a G residue connected via ester linkage to a LA residue; it represents internal LA residues that divide otherwise contiguous G sequences and is the only motif expected to decrease with hydrolytic treatment. Resonance **ii** (Figure 2-7b) represents internal, G-adjacent G residues, whereas the set labeled **iii** (Figure 2-7b) is a diastereotopic proton system representing LA-adjacent G residues. This means that the two methylene protons for a glycine residue that is LA-adjacent are non-equivalent. The conditions for this are likely related to the fact that LA is chiral and G is not, so each LA-adjacent methylene proton experiences a distinct environment, whereas those same protons would not if it were a G-adjacent G residue. As such, the protons split each other and produce a doublet of doublets, instead of a singlet. The large relative abundance of peak **ii** for the silica condition indicates G enrichment. Two C-terminal G motifs are labeled **iv** and **v** (Figure 2-7c). Resonance **iv** reflects mostly the population of amide-linked heterodimers, while resonance **v** represents G residues that are amide-linked to another G. Additional NMR data (Figure S5) further reinforces the low abundance of ester linkages in the silica samples and the compositional observations from MS data.

Table 2-1   Percent yield of glycine bonding motifs from ¹H-NMR, determined as a percent of total glycine signal detected. A description of the motifs can be found in the supporting information, section ii.

Sample Condition		Silica		No Substrate	
		Post Reaction	Post Ester-Hydrolysis	Post Reaction	Post Ester-Hydrolysis
(i)	–**G**–LA–	0.6%	0.1%	6.8%	0.8%
(ii)	–G–**G**–G–	11.8	10.8	4.9	4.4
(iii)	–LA–**G**–G–	7.6	7.1	16.7	15.8
(iv)	LA-**G** dimer	12.8	10.6	4.0	9.4
(v)	–G–**G**	4.6	4.4	11.5	13.8
Total amide yield		**37%**	**33%**	**44%**	**44%**

A summary of NMR findings in Table 2-1 lists the yields of each motif, derived by integration of each region, as a percent of total glycine detected. The absence of motif **i** for silica samples is consistent with MS data that identifies 1LA-oligomers as most dominant, and confirms the one LA residue as N-terminal. Greater abundance in this motif is expected for the control reaction that is dominated by multi-LA products. The ratio of terminal to internal G residues (**ii**:**v**) is larger in silica samples than substrate abscent samples and indicates a greater abundance of contiguous peptide cores. Post-hydrolysis, all signal for motif **i** disappears as expected, due to the adjacent ester. The abundance of motifs **ii** and **iii** are accordingly uneffected by ester hydrolysis, while mofits **iv** and **v** change differently for each condition. In silica samples, the small decrease for motifs **iv** and **v** is likely due to limited amide hydrolysis. For substrate absent sample, signal increase in **iv** and **v** arises from the fragmentation of longer oligomers into simple heterodimers (**iv**) and loss of LA or poly-LA tails to reveal C-terminus G residues (**v**).   The total amide yield for silica samples is reduce compared to control samples and is like related to the decreased incidence of ester linkages that are activated sites for amide formation or the persistence of some species on the substrate during the preparation of liquid-phase analysis. Though fewer total amide linkages are formed with silica, contiguous G chains are more prevalent based on MS (Figure 2-2) and NMR (Figure 2-7b peak **ii**) data. While amide yield within the same condition should not differ post-hydrolysis, the 12% decline for silica samples may be due to substrate-aided hydrolysis in a hydrated state.

Figure 2-8 – Structures of depsipeptide sequence motifs identified by NMR, listed in Table 1 and Figure 2-7 from the main text.

Comparison of the reaction mixtures with standards and post-hydrolysis spectra allowed for the identification of five distinct G bonding motifs, displayed in Figure 2-8. The methylene protons for which each label refers to are emboldened. Ester and amide linkages are denoted by red and blue colored oxygen and nitrogen atoms, respectively. Motifs **i**, **ii**, and **iii** may appear in an oligomer internally or at the termini, however motif **iv** refers specifically to a 2-residue species and motif **v** occurs only at the C-terminus.

42

After the ester hydrolysis treatment, only motif **i** should exhibit substantial decrease in prevalence, as it is the only motif that would become another motif (**i** would become motif **v** after ester cleavage). Though motif **iii** does contain a LA residue, the bonding state of that O-terminus hydroxyl, ester or carboxylic acid, does not significantly affect the G proton.
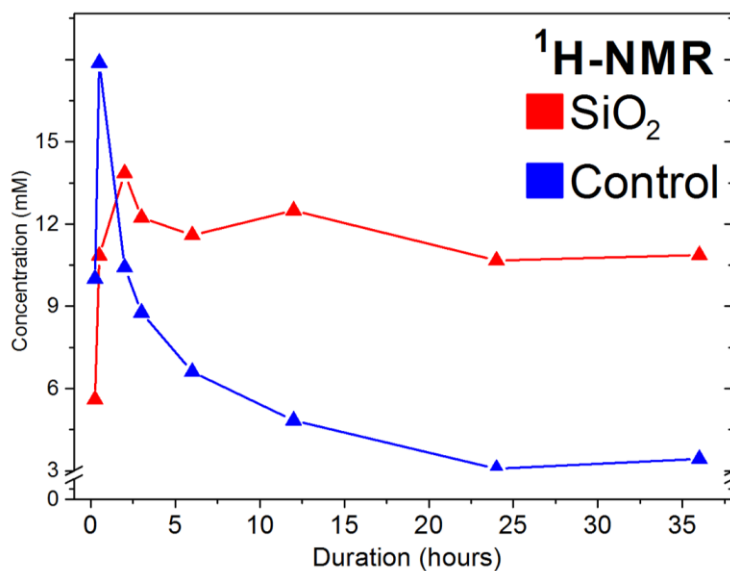
Figure 2-9 – Behavior of the LA-G heterodimer as a function of time, monitored by ^{1}H-NMR.

Identification of the amide-linked heterodimeric species by NMR analysis allowed the abundance of this initial depsipeptide molecule to be monitored as a function of time and corroborate the result from Figure 2-5. The resulting plot, Figure 2-9, shows good agreeance with the data from MS extracted ion chromatograms. The principal features for the substrate-absent control condition is a rapid rise in heterodimers, followed by a slightly less rapid consumption. This consumption could occur via amide hydrolysis, but more likely is due to addition of a LA residue to the C-terminus of the heterodimer. Dissimilarly, the abundance trace for the reaction with silica demonstrates a slower initial production, to

a smaller maximum abundance with a very slow consumption of the heterodimer. As higher order products have been identified, it is not the progression of the reaction that is responsible for the sustained heterodimer abundance, but likely a steady state of heterodimer production and consumption. This suggests that the intermediate confirmation is rate-limiting, and may be a silyl-esterified LA molecule.

2.4.2.3 Standards

Within these NMR conditions, the methylene (CH_2) system for glycine residues in a glycine oligomer experience a sizable chemical shift depending on their position in the oligomer; for oligoglycine at least up to G_5, each residue methylene is well resolved. Consistently, the most up-field position is the C-terminus residue and the second most up-field position is the N-terminus residue. While the remaining positions can be assigned, as a general rule, an increasingly down-field chemical shift is associated with an increasingly central glycine residue. Various oligoglycine standards, analysis of an oligomerized LA–G cassette have been compared to the products of G+LA depsipeptide reactions.
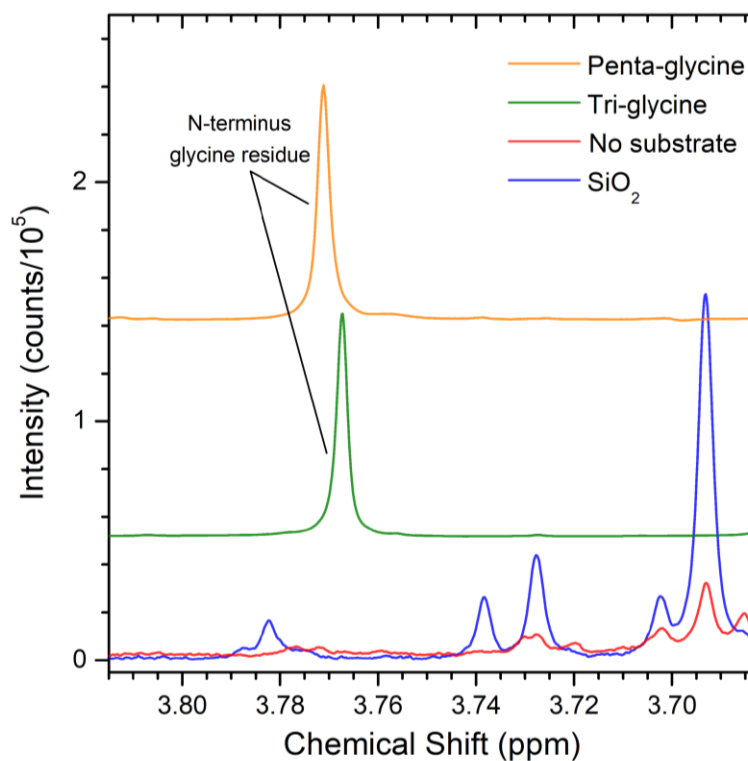
Figure 2-10   Spectral region for the N-terminus glycine residue for several oligoglycines and products of G+LA depsipeptide reactions at 125 °C with and without silica.

Figure 2-10 highlights specifically the N-terminus glycine methylene proton at 3.767 ppm for a Gly$_3$ standard, and at 3.771 ppm for a Gly$_5$ standard. Not shown are the C-terminus resonances, up-field, and the internal residues, down-field. The absence of this peak in both silica and substrate absent depsipeptide samples suggests that no depsipeptide oligomers are glycine terminated at the N-terminus and instead are terminated by an amide-linked LA residue, as previously speculated regarding 1LA containing species from MS data.
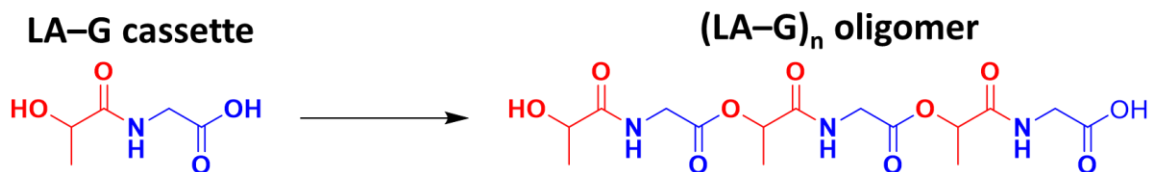
Figure 2-11   Molecular representation of the LA–G cassette "monomer" and oligomer.

In an effort to aid the process of assigning bonding motifs for all signal in crude G+LA reaction mixtures, a synthesized amide-linked LA–G heterodimer, or cassette, was analyzed in its monomeric and oligomeric states, before and after a dry-down reaction, see Figure 2-11. These molecules are very useful as no two glycine residues are adjacent. Also, the difference between the monomer and oligomer forms is exclusively due to ester formation, with no new amide motifs formed.
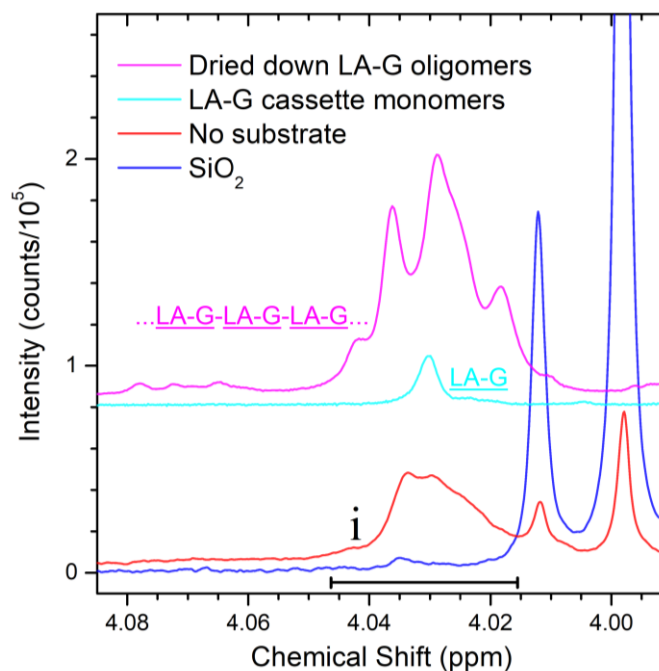
Figure 2-12   NMR analysis was conducted on a LA+G system incubated for 20 hours at 125 °C.

NMR analysis was conducted on a LA/G system incubated for 20 hours at 125 °C, Figure 2-12. The broad G resonance at 4.03 ppm labeled (**i**) is abundant for the silica-absent control condition, but does not appear for silica-containing samples. Peak (**i**) diminishes after hydrolytic treatment, so it has been attributed to an ester-bonding system, as […G-LA…]. This assignment was further confirmed by comparison with the LA-G cassette synthesized amide heterodimer (LA-G). When the cassettes are dried down in similar procedure as described in the main text, esterification occurs forming extended $(LA-G)_n$ oligomers. The […G-LA…] motif is therefore present in the condensed cassette sample, which overlaps the peak **i** resonance precisely. The motif is absent for the LA-G cassette monomers that have been incubated for only a short period, though the beginning of signal in this region is visible. The cassette monomers do not show signal here because the G residue is not ester bonded, as it is for the oligomer at the C-terminus side. The diastereotopic methylene signature for the cassette monomer comes at 3.63-3.73 ppm.
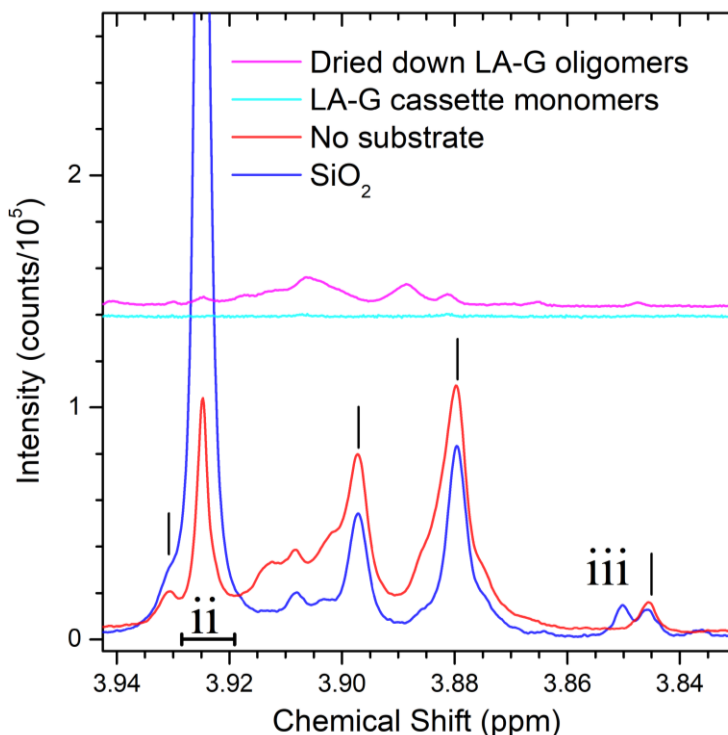
Figure 2-13 – NMR analysis was conducted on a LA/G system incubated for 20 hours at 125 °C.

For the same sample, the assignments for internal or G-adjacent G residues can be tested with the oligomerized cassette. Similar to Figure 2-7b, the doubly amide-linked internal G motif is confirmed by comparison with prepared LA-G amide-linked heterodimers. The region from 3.86-3.94 ppm Figure 2-13, contains two distinct internal G motifs. The undiminished signal, post-hydrolysis, suggests that the G residues are amide bonded at both sides, as in [...G-**G**-G...] (**ii**) and [...LA-**G**-G...] (**iii**). It is known that the central G is LA adjacent for peak set **iii** due to a set of diastereotopic resonances. These resonances are prominent in both conditions of the LA/G monomer reactions, with and without silica. However, the LA-G cassette monomer and extended (LA-G)$_n$ condensation spectra show no signal at 3.925 ppm (the spectra are zoomed in to see that slight signal from product impurities). Even though the cassette G is amide-linked, neither of these

peaks appear, supporting the assignment of both peak **ii** and **iii** as 3-unit motifs distinct from (LA-G)$_n$. This is because there are little or no contiguous G units in cassette experiments, whereas G$_n$ is found in LA/G monomer reactions and is especially prominent in the presence of silica.
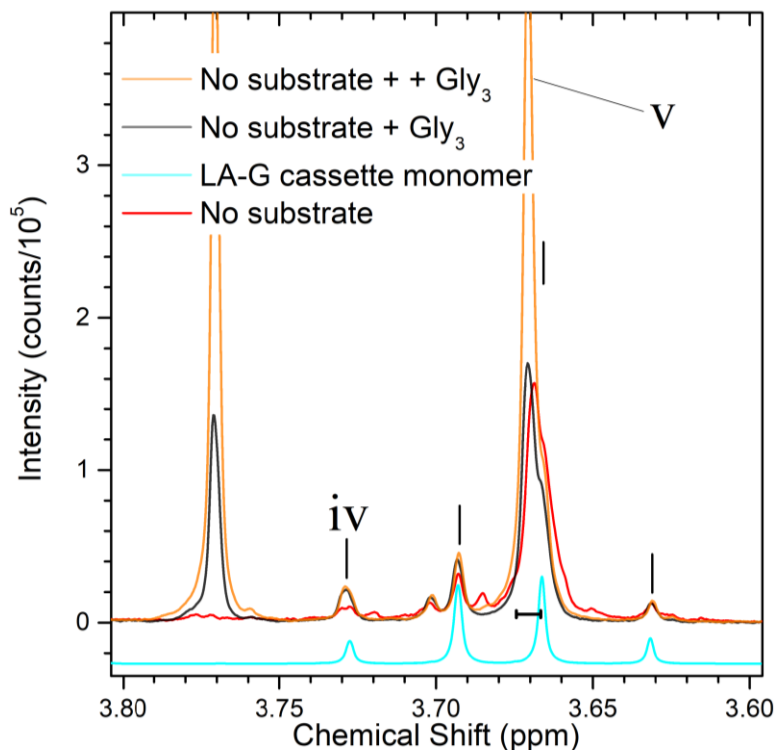
Figure 2-14 – NMR analysis was conducted on a LA/G system incubated for 20 hours at 125 °C.

NMR analysis was conducted on a LA/G system incubated for 20 hours at 125 °C. Similar to (Figure 2-7c) in the main text, the double amide-linked internal G motif is confirmed by comparison with prepared LA-G amide-linked heterodimers. The region from 3.62-3.74 ppm, Figure 2-14, has been associated with C-terminus glycine residues in […LA-**G**] (**iv**) and […G-**G**] (**v**) bonding motifs. To confirm the identity of the 3.67 ppm peak, G$_3$ was incrementally spiked in under similar pH conditions and overlaps well with

49

the proposed C-terminal G. The peak at 3.77 ppm is the N-terminus G residue. Since the signals do not increase after hydrolytic treatment, the G residues are assumed to be amide bonded. The resonance at 3.67 ppm (**v**) represents the terminal G for all oligomers longer than a dimer, while superimposed on this peak are diastereotopic methylene protons (**iv**), split due to their vicinity to a LA residue, from the C-terminus G of the amide-linked heterodimer.
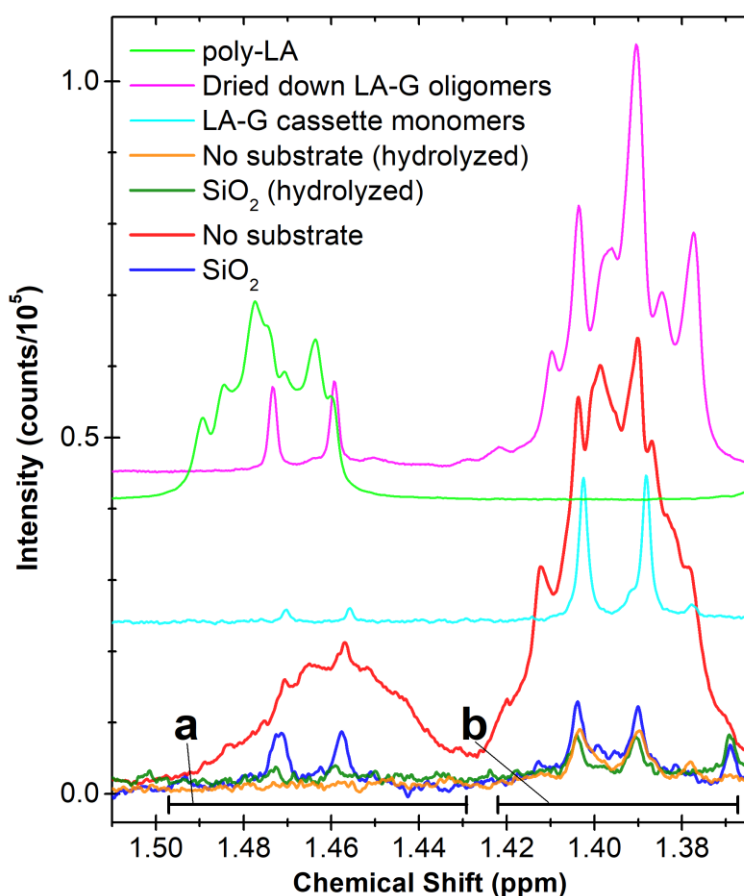
Figure 2-15   Methyl region for LA residues in G+LA depsipeptide and LA−G cassette reactions at 125 °C and for poly-LA.

^{1}H-NMR data for the LA methyl (CH$_3$) region, Figure 2-15, with only the four spectra on the 0 count baseline are scaled by an external capillary insert allowing for

50

quantitative comparison. Two distinct resonances in the LA methyl region, shown here from 1.36-1.50 ppm, offer support for differences in product composition for LA/G oligomers in depsipeptide forming system after 20 hours of incubation in a dry state at 125°C (conditions identical to those for spectra shown in Figure 3 of the main text). Analysis of prepared standards enabled the identification of both regions.

Region **a** (1.43-1.50 ppm) overlaps with two of the standards presented: poly-LA, which has its dominant signal here as a broad and over-lapping cluster of doublets, and the oligomerized $(LA-G)_n$, which has its minor signal here as a narrow doublet. The absence of signal in this region for the amide linked LA-G cassette monomers, which possess no ester linkages, suggests that region **a** is ester-associated. However, when those cassettes are incubated to a dry state, in similar fashion to depsipeptied experiments, and form $(LA-G)_n$ abundant with esters, the appearance of signal is relatively minor. In $(LA-G)_n$ oligomers, LA is always adjacent to G, so region **a** cannot refer to a G-associated motif. This is supported by the overlap of the poly-LA signal, which contains exclusively LA-LA esters. Furthermore, signal disappearance after hydrolytic treatment confirms that the region **a** signal is ester-associated. Thus region **a** is not only ester-associated, but refers to LA residues that are surrounded by other LA and not adjacent to G residues, which has also been previously determined in high molecular weight poly-LA samples.[96] The sharp doublet in region **a** from the $(LA-G)_n$ sample may be due to esterified LA monomers as impurities or hydrolysis products, or it may refer to terminal LA residues.

Region **b** (1.37-1.43 ppm) overlaps with two of the standards presented: the oligomerized $(LA-G)_n$, which has its dominant signal here as a broad and over-lapping cluster of doublets, and the monomeric LA-G cassette, which also has its major signal here,

51

as a narrow doublet. The absence of signal in region **b** for the poly-LA sample and abundance of signal for either form of LA-G suggests that region **b** is G-associated. The difference in spectra for the LA-G cassettes before and after oligomerization suggests that the broadness of the peak is due to esterification. Furthermore, signal disappearance after hydrolytic treatment confirms that the region **b** signal is ester-associated. Thus region **a** is not only ester-associated, but G-associated, and refers to LA residues that are adjacent to atleast one G residue. To add, though this region is G-associated, it does not necessitate that the G residue is amide bonded to another G or LA residue. However, in the $(LA-G)_n$ spectrum in this region integrates 3:2 with the G methylene region assigned to motif **i** (see Figure S.A), which suggests that it is the LA-methyl component of motif **i** and indeed also amide-associated. This region is distinct from the monomer cassette signal (3.63-3.73 ppm, motif **iv**) that is only an amide system and an ester-linked G-LA dimer is excluded as a contributor to this signal, as N-terminus G residues are not observed (see Figure S.C).

The spectrum for the substrate absent condition shows signal in both regions much greater in magnitude than for the silica-containing sample, which has almost none. As both regions **a** and **b** are ester-associated, this observation supports the characterization of oligomers produced in the presence of silica as ester deficient, especially as contiguous LA sections. After the hydrolytic treatment, all signal in both regions disappears, which is expected with ester-associated motifs. The oligomer units that contributed to signal in region **b** likely became amide-linked LA-G dimers, post-hydrolysis. This agrees with amide bond yield data from Table 1 in that the 6.0% decrease of motif **i** is very near the 5.4% increase of LA-G dimers (motif **iv**).

2.4.3   LC-MS of Depsipeptide Products

Since yields obtained from ESI-MS are difficult to quantify, liquid chromatography mass spectrometry analysis of the G+LA depsipeptide system, reacted at 125 °C has been employed to determine the relative abundancies of oligomer compositions and augment the quantitative data from NMR.

2.4.3.1   Sample preparation

Liquid chromatography mass spectrometry (LC-MS) was conducted on an Agilent 1260 HPLC coupled to an Agilent 6130 ESI-QMS and adapted from a published procedure [93]. Chromatographic separation occurred on a SeQuant ZIC-HILIC column (150×2.1 mm, 3.5 µm PEEK coated particle, 100 Å pore size). The analytical procedure held the column at 40°C, maintained a 0.2 mL/min flow rate and injected a 2 µL volume of analyte, diluted 4x in a 1:1 acetonitrile/water solution. The mobile phase was (A) water with 0.5% v/v formic acid added and (B) acetonitrile. The procedure began at [A=5%, 5 min], then ramped linearly to [A=50%, 25 min], maintained [A=50%, 5 min], ramped down to [A=5%, 1 min] and maintained at [A=5%, 14 min], totaling 50 minutes. The MS was collected in negative mode, with similar expected product masses as direct injection.

2.4.3.2   Reactions of Glycine and Lactic acid

Analysis of the G+LA depsipeptide system, reacted at 125 °C, was analyzed via LC-MS and reported in Figure 2-16. In panel **a)** the total ion chromatogram demonstrates that the 1LA+nG species is by far the major product for silica containing reactions. The 2LA+3G (t=7.54 min) peak is the only multi-LA species in large abundance, but extracted

ion chromatograms (EIC) for the masses associated with the 1LA+4G (t=11.13 min) and 2LA+3G 5-mers determine that the integrated signals are within 1% difference; the visual discrepancy is due to some co-elution at 7.5 min, an issue also seen for the 1LA+7G (t=14.12 min) where the EIC determines the abundance to be slightly less than 1LA+6G species, as expected. The prominent LA monomer peak (t=3.12 min) agrees with NMR analysis (Figure 2-7a) where silica samples had significantly more monomeric LA remaining than silica absent samples. The two peaks assigned to the heterodimer (t=5.02, 6.01 min) likely represent both the amide (LA-G) and ester (G-LA) linked forms of the dimer, which are indistinguishable by the [M-H]⁻ mass dominant for both peaks. Whereas the peak at t=6.01 min is present for both conditions, the t=5.02 min peak is most abundant for the silica sample. NMR data shows a significant amide linked heterodimer deficiency for substrate absent samples relative to silica containing reactions, which suggests that the t=5.02 min peak is amide linked (LA-G) and the t=6.01 min peak is ester linked (G-LA).

In panel **b)** the TIC demonstrates that the 1LA+nG species is not the major product for substrate absent reactions, beginning with the 4-mer. 2LA and 3LA species are prominent for the control condition, highlighting the product composition difference due to the presence of silica. A large LA monomer peak is not present, which agrees with quantitative NMR data seen in LA monomer CH quartet peak (Figure 2-7a).

Region **i** encompasses monomeric LA and multi-LA species that appear in low abundance for each condition. Panel **c)** demonstrates that when silica is present, though less monomer LA is consumed, LA-rich species are uncommon, with only 2LA+1G 3-mer detectable. In contrast, panel **d)** shows several distinct species with two to four LA residues.

The species in this region underscore the distinction in composition between oligomers produced in the presence or absence of silica.
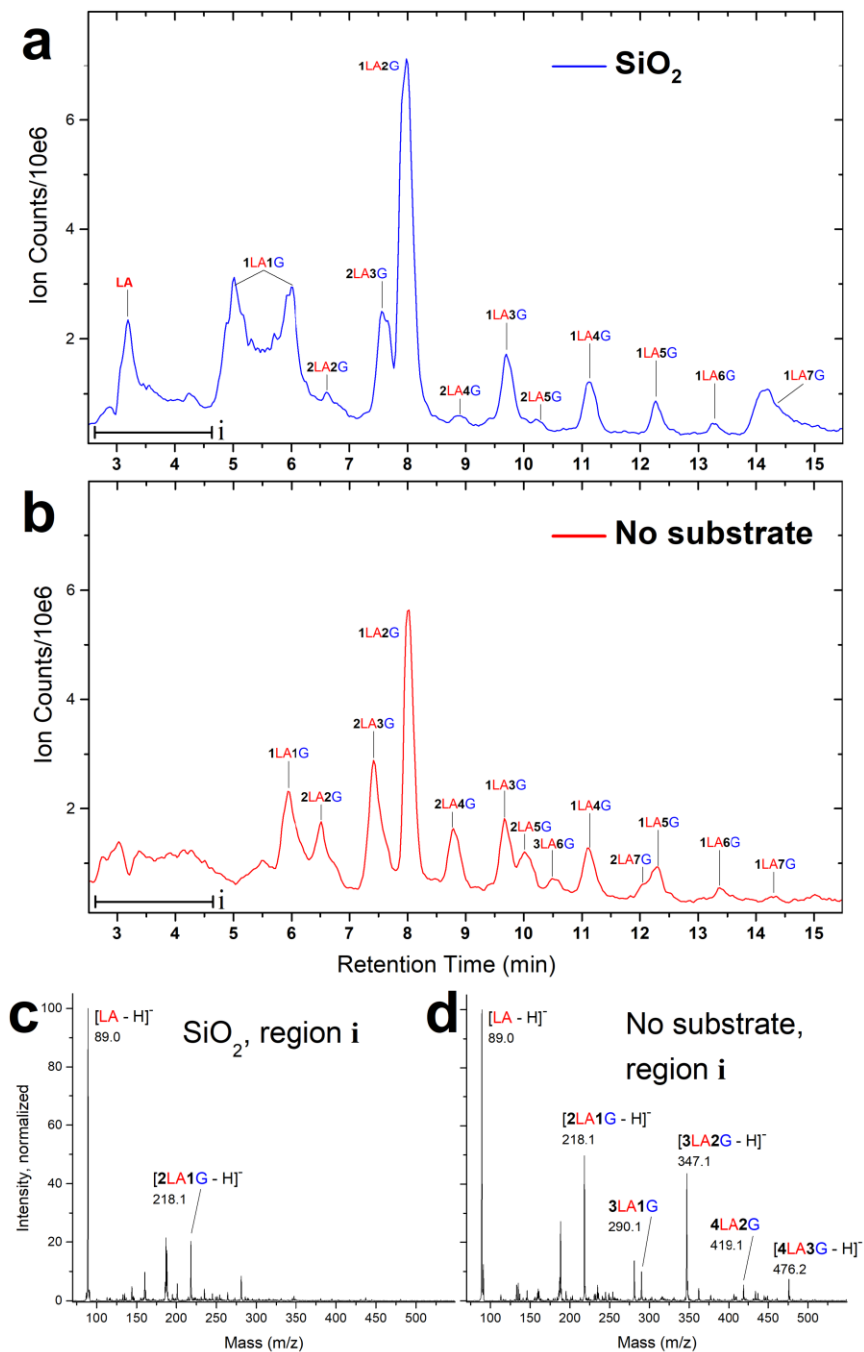
Figure 2-16   Liquid chromatography mass spectrometry (LC-MS) data for a 1:1 100 mM glycine and lactic acid system, after 20 hours of incubation at 125 °C. Total

55

ion chromatogram (TIC) of the reaction in the a) presence of silica and b) absence of silica. Mass spectrum of c) region 1 for the silica sample and d) region 1 for the control sample.

2.4.4   Non-Concurrent Reaction of Depsipeptide Components

In an effort to probe the possible role of a surface reaction, a stepwise version of the reaction was carried out. The two-step process is a modification of the aforementioned dry-down procedure, allowing the LA to pre-react with silica and potentially form silyl esters that would be activated towards ester aminolysis. The reaction proceeds by addition of silica (100 mg/mL) to LA (0.25 mL at 100 mM), then incubation at 85°C for 24 hours. The sample is washed with excess cold water, agitated, centrifuged and the supernatant removed. This process is repeated two additional times. A similar volume of G (0.25 mL at 100 mM) was subsequently added to pre-reacted silica particles and re-incubated at 85°C for an additional 3 days. The sample is then rehydrated and the supernatant analysed by ESI-MS, are shown in Figure 2-17.
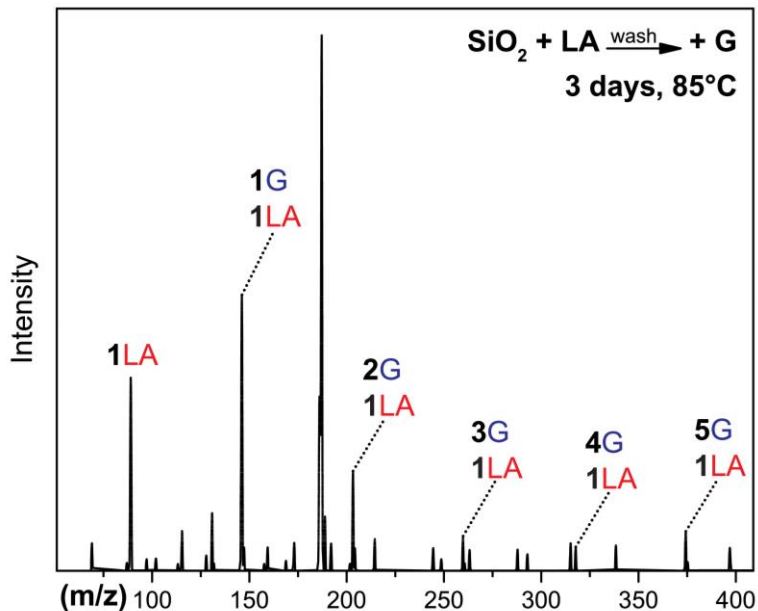
Figure 2-17 **Mass spectrum of a LA+silica then G stepwise reaction after 20 hours of re-incubation at 85 °C. The initial step allows only LA and silica to react, creating a population of surface bound residues, followed by a wash step that removes all free LA. The second step of G only addition produces oligomers with dominant compositions labeled above.**

Similar to the previous one-step experiments, the two-step products contain few α-hydroxy acids and are dominated by oligomers with a single LA residue. However, the implications of observing products from this reaction are quite large. The washing step assured that only surface-bound or reacted LA was available in the system, illustrated as motifs a) and b) in Figure 2-18. The reaction of silica+LA might produce bulk phase poly-LA, surface grafted LA monomers, surface-grafted poly-LA and bulk LA monomers will remain as well. After the washing procedure and assuming insignificant hydrolysis, both the bulk poly-LA and LA monomers will be removed from the surface. Since the MS analysis revealed oligoglycine, it can be concluded that the addition of G to this sample allowed for amide formation via EAX. While this result does not imply that all the esters are surface-esters, as Figure 2-18b demonstrates, the retention of esters implies that there

57

is *some* mechanism of anchoring to the surface. This mechanism of anchoring may indeed

be a silyl-ester, or it may be electrostatic in nature and is worth pursuing further.
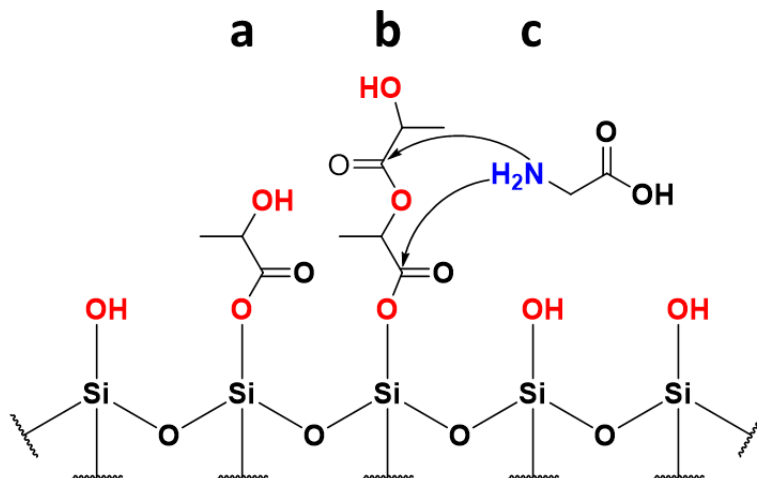
Figure 2-18   Scheme for the step-wise depsipeptide reaction of LA+G on silica. Motifs a) and b) represent possible post-washing LA arrangements, while c) represents the variety of activated ester sites that the glycine could react with via ester-aminolysis.

An ideal experiment to confirm the nature of this interaction would involve a LA-like molecule that is capable of forming silyl-esters, but incapable of poly-esterifying, thereby limiting the potential EAX sites to the surface exclusively.

2.5   Conclusions

Interaction between substrate and molecular components of peptide and depsipeptide forming heterogeneous systems have been documented [97]. Reactive hydroxyls and Lewis acid and base terminations are expected to occur on other metal-oxide surfaces [98] and interact with α-hydroxy acids [99]. Earlier work has also suggested that organic acids esterified with surface hydroxyl groups are potentially important for mineral catalysed amide bond formation under prebiotic conditions [100]. Though silicates were

present on early Earth [89, 90] and SiO_2 is a primary component of basalt and primary magmatic rock [101], silica has been thought to be of minor importance in the prebiotic formation of oligopeptides due to limited reactivity of the surface when exposed to liquid-phase solutions containing amino acids [102]. However, the interaction with co-adsorbates or co-reactants, such as esterified surface hydroxyl groups, was not considered.

In summary, formation of alanine and glycine depsipeptides in the presence of lactic acid and SiO_2 nanoparticles have been studied under plausible prebiotic conditions. The dominant species produced in the presence of SiO_2 and lactic acid show minimal hydroxy acid residues (i.e. ester linkages) by MS analysis and substantial signal for sequence motifs abundant in amide bonding by ^{1}H-NMR analysis. Oligomers exceeding 10 contiguous G residues and up to 7 alanine residues have been produced. Similar product distributions and amide bond formation also occur with silica that has been pre-reacted with lactic acid, suggesting a catalytic role of surface silyl ester bonds. Overall, surface functionalization of oxides with simple α-hydroxy acids may provide catalytic pathways useful for unravelling plausible routes to production of complex molecules under early Earth conditions or on extraterrestrial bodies.

CHAPTER 3. MECHANISM OF SILYL-ESTER AMINOLYSIS ON SILICA SURFACES[2]

3.1 Summary

Poly-condensation of glycine with modified α-amino acid and α-hydroxy acid analogs in the presence of SiO_2 has been studied under plausible prebiotic conditions. An O-methylated α-hydroxy acid and an N-acetylated amino acid were chosen as non-oligomerizing reactants to investigate the mechanism of amino acid enrichment in mixed amide/ester proto-peptide oligomers, known as depsipeptides. Glycine oligomerization was found to proceed via aminolysis of activated silyl-ester motifs on a silica substrate, initially formed between surface silanols and the modified reactants, and subsequently formed between silanols and C-terminus glycine residues. Ester formation was confirmed by a reversible shift in the carbonyl stretching frequency via infrared spectroscopic analysis. Oligomerization did not occur in the absence of fumed silica, due to the lack of an ester-forming nucleophile. Reactions utilizing an alternative SiO_2 sample, without discernable isolated silanol terminations, were unable to form silyl-esters or facilitate glycine oligomerization. This work describes the mechanism by which silica or other minerals may promote oligopeptide formation within depsipeptide reactions or other diverse chemical environments on Early Earth.

---

[2] This chapter was adapted from a soon to be submitted manuscript. McKee, Aaron D.; C, Martin; Leman, Luke J.; Liotta, Charles L.; Hud, Nicholas V., Orlando, Thomas M. "Mechanistic investigation of prebiotic oligopeptide formation on silica surfaces via ester aminolysis" 2019

3.2   Background

Often, in the context of exclusively amino acid, evaporation-driven reactions, products formed while in the presence of silica are compared to such products with other substrates. Silica has been reported to produce shorter length oligomers in glycine condensation reactions, compared to titanium, aluminum and iron oxides. This under performance is attributed to the dominance of zwitterionic glycine residues, which possess significantly less reactive moieties, i.e. the primary ammonium ion (NH_3^+) or carboxylate ion (COO^-), over the anionic/cationic states that are formed through interaction with other surfaces. Specifically, TiO_2 and other metal oxides are thought to catalyze glycine condensation by increasing nucleophilicity via deprotonation of NH_3^+ to NH_2 and increasing electrophilicity by withdrawing electron density from the carboxylate via adsorption [59]. As previously discussed, G poly-condensation has been reported with silica substrates [103, 104], citing surface-aided catalysis when silanol (Si-OH) pairs allow for co-adsorption of G residues in both canonical and ionic states. The same body of work that offers mechanism for silica catalysis also explicitly and repeatedly demonstrate that a covalent ester adsorption pathway is inaccessible for silica and glycine [79].

3.2.1   Step-Wise Reaction

The final experiment discussed in chapter 2, summarized by Figure 2-17 in section 2.4.4, provided the very interesting result that some surface bound species is formed after incubation of fumed silica with LA. Ultimately, this experiment could have been better designed, as there was ambiguity as to the nature of the esters that were necessary formed

to permit oligoglycine formation via ester-aminolysis. The same experiment, silica+LA incubated at 85 °C, was repeated and analyzed by infrared spectroscopy (Figure 3-1).
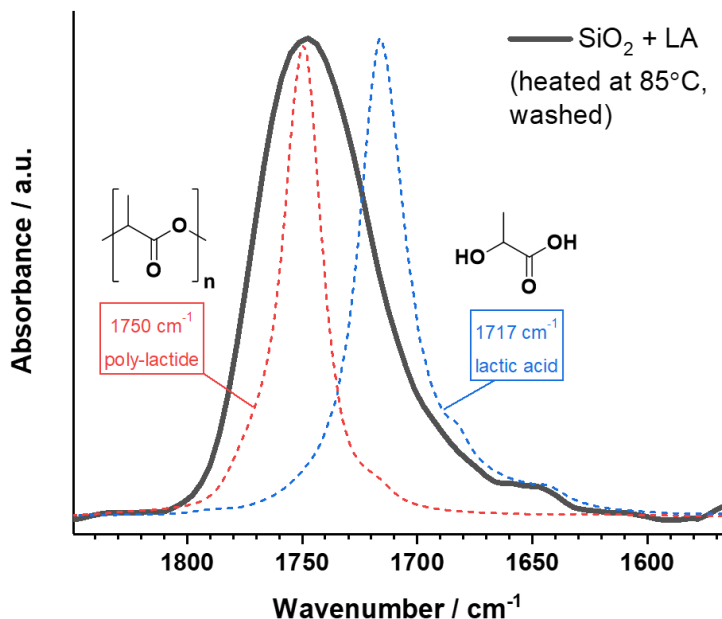
Figure 3-1 **Infrared spectrum of silica incubated in an aqueous 100 mM solution of LA to evaporation at 85 °C, then washed with dry acetonitrile . Lactic acid d in monomer and polymer form are included as references for LA as a carboxylic acid and as an ester.**

Infrared spectrum of silica with lactic acid (LA) incubated at 85 °C to evaporation (LA at 100 mM, fumed silica added at 100 mg/mL), then washed with dry acetonitrile with 5x the initial volume reacted. This spectral region focuses on the carbonyl (C=O) stretching mode for carboxyl moieties. For reference, a spectrum of unreacted LA, representing a carboxylic acid (COOH, 1717 cm^{-1}) carbonyl, and a spectrum for poly-lactide, representing an ester (COOR, 1750 cm^{-1}) carbonyl, are included and agree with literature values [105, 106]. LA is a hydroxy acid that, along with amino acids, are the molecular components of a depsipeptide forming system. Since LA has both alcohol and carboxyl functionalities, it is able to form polyesters. Within typical depsipeptide reactions, LA is capable of forming

activated esters at mild temperatures [58] and therefore facilitates amino acid condensation via ester aminolysis in dried films. Depsipeptide reactions in the presence of silica are amino acid enriched, possibly due to an activated surface ester [107].

The step of washing the substrate, post-reaction, is crucial in removing molecules not bound to the silica surface. Dry acetonitrile was used to avoid hydrolysis, even at room temperature. LA might be bound to the silica covalently via a silyl ester linkage [108] or non-covalently by surface stabilization of an ionic form [75]. The strong peak at 1750 cm^{-1} suggests that there are LA molecules remaining that are ester bonded to the surface. The lack of signal in both the symmetric/antisymmetric carboxylate regions demonstrates that a non-covalent interaction that retains molecules after washing is unlikely. While it is difficult to discern between signals of poly-LA and a silyl ester, ester linked propionic acid on silica has been prepared by simple heating [108]. It is likely that LA-LA esters contribute to the signal at 1750 cm^{-1}, the existence of the signal, post-wash, requires an ester anchor. This data suggests that esterification with silanol terminations on silica can proceed under the reaction conditions studied in this account by LA monomers and likely other depsipeptides. These silyl esters may serve as activated sites for ester aminolysis and therefore may contribute to the disparity in depsipeptide composition in the presence of silica compared to a substrate absent condition.

Diffuse reflectance IR (DRIFTS) analysis of powder samples is an ideal technique to determine if an ester is present on a surface, LA is not well suited for this examination. After incubation of silica+LA, the IR spectrum show overlap with the poly-lactide standard, inferring ester formation. However, the ester signal could originate from LA

dimer cyclization, bulk poly-LA, surface grafted poly-LA, in addition to a surface silyl-ester (Figure 3-2).
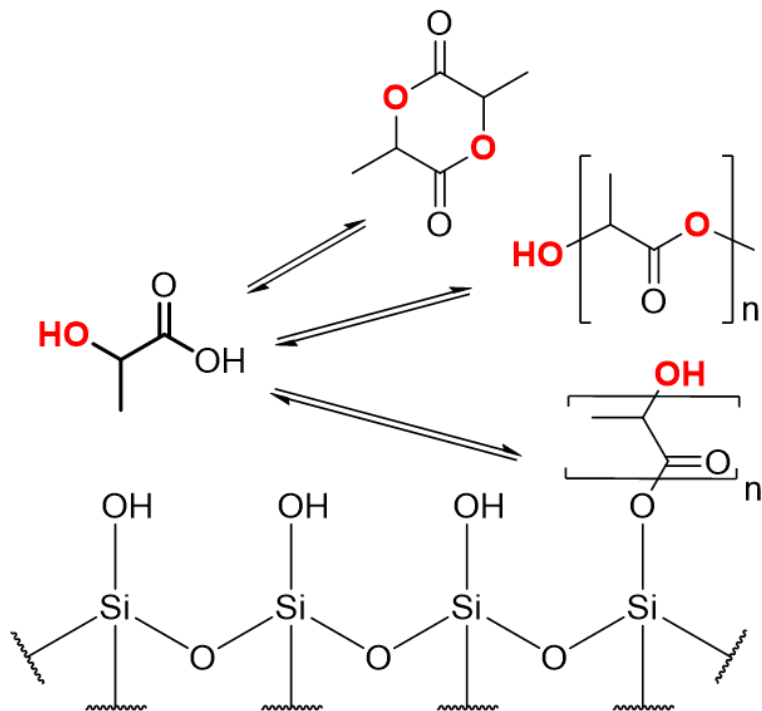
Figure 3-2   Scheme of possible ester-forming paths that LA can follow within an incubated dry-down reaction with fumed silica.

3.2.2   *Amino Acid and Hydroxy Acid Analogues*

In the preceding chapter, ester-mediated amide bond formation in depsipeptides [58] (ester amidolysis [109], EAX) has been expanded to a heterogeneous system [107] and demonstrated behavior distinct from the homogeneous reaction of similar molecules. The oligomeric products from co-reaction of the α-hydroxy acid lactic acid (LA) with glycine or alanine are amino acid enriched in the presence of fumed silica, compared to silica-absent control reactions. Detailed analysis of the supernatant showed greater abundances of contiguous amino acids in addition to fewer ester-bonded motifs. The

paradox of observing excesses of amide bonds, which form almost entirely via EAX at a mild temperatures, with fewer esters present to serve as activated motifs, suggests that the substrate may act as a catalysis for amide formation. Sequential reaction of the same depsipeptide components in the presence of silica resulted in OH-peptides, i.e. oligopeptides with an amide-bonded α-hydroxy acid at the N-terminus. These results suggest that the near 40% amino acid inclusion yield is due to silica-involved catalysis, likely via an activated surface ester, and not direct amide formation [107].

There have been many accounts of metal oxides catalyzing direct amide formation for amino acids [74, 92, 110, 111], yet silica persists in being considered a non-ideal substrate for amino acid exclusive systems [59]. These results are undeniable, however, and have been reproduced in section 3.4.1. Only minimal amounts of di- and tri-glycine products are detected from thermal incubation of silica with glycine when no α-hydroxy acid co-reactant, such as LA, was present. Unbuffered G dry-down reactions in the presence of silica, confirm some amide formation, but did not show esters or consumption of surface silanol sites. Due to the poor electrophilicity of monomeric G films on silica in the zwitterionic state, G alone is not well suited for direct or ester-mediated poly-condensation. This ambiguity motivates the selection of a LA analog which cannot polymerize or cyclize, by eliminating the nucleophilic alcohol group, but still has the ability to esterify, by retaining the electrophilic carboxyl group (Figure 3-3). 2-methoxypropionic acid (MOPA) possesses these characteristics, while maintaining steric and pK_a properties similar to LA. This rational was also applied for amino acids and motivated the selection of N-acetylglycine (NAG), which is similarly unable to cyclize or polymerize.

2-methoxypropionic acid
(MOPA)

N-acetylglycine
(NAG)
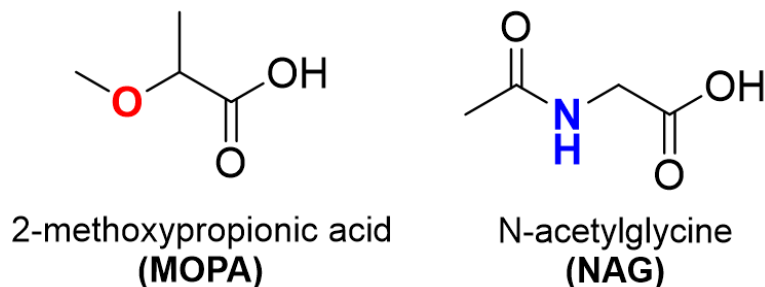
Figure 3-3 **Molecular structures of α-hydroxy acid and amino acid analogue.**

In evaporative conditions, LA is able to condense and form poly-ester oligomers exceeding 12 residues in length [58]. To probe the ester-forming, and therefore activating, ability of depsipeptide reagents with silica, intermolecular esters which could act as sites for EAX must be eliminated from the system to leave only silyl-esters as activated sites. Methoxylation of the LA alcohol removes nucleophilic functionality and therefore the ability to cyclize or oligomerize, while retaining similar acidity and steric bulk. In place of LA, 2-methoxyproprionic acid (MOPA) will serve as a mono-functional analog. A second model reagent was required to model a C-terminus G residue similar to the amide-bonded depsipeptide heterodimer LA-G, as it represents the ester-forming electrophile for repeated G addition at an oligomer C-terminus. Transformation of the G amine to an amide via N-acetylation achieves this by maintaining G in the anionic, rather than zwitterionic, form while also restricting cyclizing and oligomerizing capabilities, a major sink for glycine reactions [28, 112]. In place of LA-G, N-acetylglycine (NAG) will serve as a molecular analog for a non-monomeric G. For the model reactions of silica with G and MOPA or NAG, the only ester-forming nucleophiles will be interfacial silanols ($\equiv$Si-OH) [113]. Therefore, the expected EAX product for those reactions is of the form NAG+nG or MOPA+nG, where a single LA or LA-G analog is at the N-terminus of otherwise pure

oligoglycine. This work outlines a mechanistic study of amide formation in depsipeptide-like systems by EAX at silica surfaces.

3.3 Experimental

Fumed silica (silica, Sigma-Aldrich, 7631-86-9, PZC: 3), 2-methoxypropionic acid (MOPA, Sigma-Aldrich, 23953-00-6, pK_a: 3.9), N-acetylglycine (NAG, Sigma-Aldrich, 543-24-8, pK_a: 3.7), glycine (G, Sigma-Aldrich, 56-40-6, pK_a: 2.4, 9.6), tri-glycine (GGG, Sigma-Aldrich, 556-33-2, pK_a: 3.7, 9.3), lactic acid (LA, Sigma-Aldrich, 79-33-4, pK_a: 3.9) and fused quartz (quartz, Sigma-Aldrich, 68855-54-9, PZC: 3-4) were used as received.

Dry-down reactions proceeded via the addition of 1:1 mixtures of 100 mM aqueous solutions of MOPA or NAG and G to silica powder. The silica powder was added at 100 mg/mL reaction solution for fumed silica, which produced a viscous suspension and required vortexing to mix completely, and 500 mg/mL or ground fused quartz. All components where incubated in an oven at 85 °C for 6 days in an open glass vial, which facilitated complete evaporation of water. Reactions were unbuffered, with the mixed MOPA or NAG and glycine solutions presenting pH~3, regardless of silica inclusion.

Mass spectrometry (MS) analysis was performed on an Agilent 6130 single quadrupole mass spectrometer via electrospray ionization (ESI-MS). Samples were rehydrated with water and analyzed in negative ion mode, with the [M - H]⁻ anion as the expected product.

Infrared (IR) analysis of samples was carried out on a Shimadzu Prestige 21 Infrared Spectrometer with a diffuse reflectance attachment (DRIFTS). Samples of silica and dried reactants were analyzed, unwashed, in powder form, using silica incubated with water at identical temperature as a background. Spectra were collected for 64 scans, at 4 cm^{-1} resolution, in the range 400-4000 cm^{-1}.

^{1}H-NMR spectra were collected on a Bruker Avance III-500 spectrometer (500 MHz) over 32 scans using a 10-second relaxation delay at 25 °C. For NMR analysis, samples were prepared via rehydration of dried reaction material in a D_2O sodium phosphate solution, buffered to pH=7. A capillary external standard containing 50 mM potassium hydrogen phthalate was used to calibrate all samples and standards.

The point of zero charge (PZC) of fumed silica was determined using a Malvern Zetasizer Nano ZS in a 10 mM solution of NaCl, buffered to pH=3.0 by phosphoric acid.

3.4   MS Analysis

For each depsipeptide component analog, e.g. MOPA, mass spectrometry was used to analyze the products of the analog with silica and glycine, co-reacted at 85 °C, to determine if amide formation occurred. If oligoglycine species are detected, the silica surface may be implicated in the ester aminolysis process, as no other ester forming nucleophile exists in the chemical system, and direct amide formation at this temperature is quite limited.
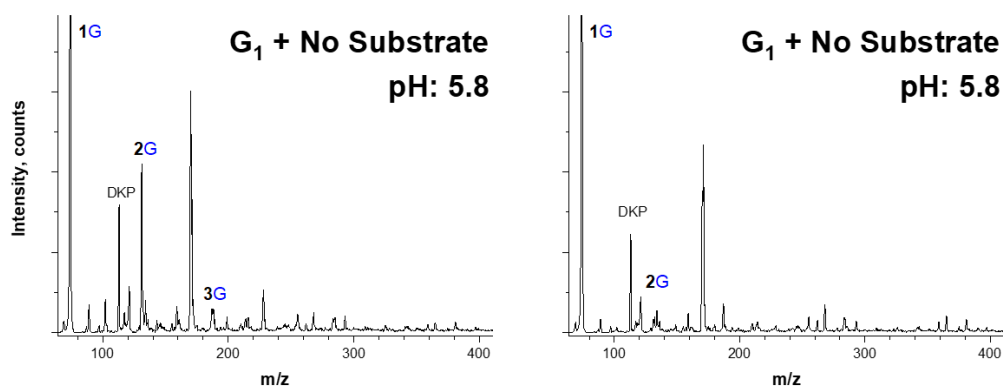
Figure 3-4   Mass spectrum of G incubated with fumed silica.

The analysis of unbuffered glycine (G) dry-down reaction at 85 °C for 6 days, with and without the inclusion of fumed silica (G at 100 mM, fumed silica added at 100 mg/mL), is reported in Figure 3-4. At moderately acidic pH and with G in the zwitterion state, conditions for acid catalyzed amide formation are not ideal. However, both reactions produce detectable amounts of amide-linked products. While both reactions produce oligomers of limited length, the silica containing sample has a greater abundance of dimers and detectable trimers, whereas the substrate absent control only shows trace amounts of dimers. This result is comparable to several reports outlined in section 1.3, e.g. [59], in that a G-only evaporative reaction at moderate temperature produces mostly glycine dimers and small amounts of trimer.
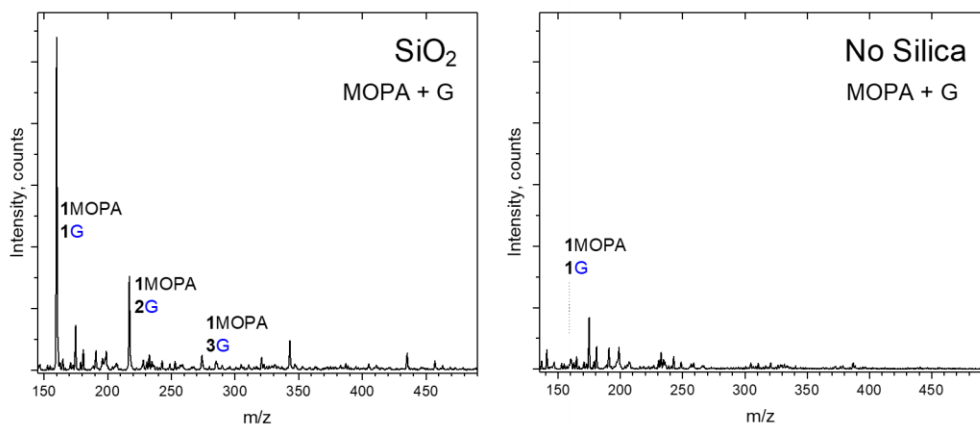
Figure 3-5   Mass spectra from dry-down reactions of MOPA+G A) with, and B) without the inclusion of fumed silica. All products are terminated by a single MOPA residue at the glycine N-terminus. Oligoglycine is only formed with silica, which facilitates peptide formation via silyl-ester aminolysis.

To access the role of silica in the oligomerization of G with the LA analog MOPA, reactions were carried out both in the presence and absence of the substrate. Products from incubation of MOPA+G at 85 °C in an evaporative environment show a pronounced distinction between the two conditions by MS analysis, summarized in Figure 3-5. When silica is not present, only trace levels of the MOPA-G heterodimer can be detected and no G–G peptide linkages of any length are formed, including pure G species without MOPA termination. The addition of silica to the MOPA+G reaction produces glycine oligomers capped by an amide-linked MOPA unit, with a G incorporation yield of 15% by NMR quantification (Table 3-1). While the maximum length does not exceed three glycine residues, linear G–G linkages are only observed in the presence of silica, suggesting a silica-involved mechanism for G oligomerization. At this temperature, direct amide formation of poly-G is not expected to produce oligomers that exceed two residues in

length in significant abundance, similar to the results of pure G incubation (Figure 3-4). The limited extent of linear peptides formed may be due to the availability of esterified MOPA sites, as MOPA is liquid at room temperature and therefore volatile at 85°C. When a volume of pure MOPA is incubated without silica, no sample is detected in the vial by NMR, while similar NMR and MS analysis of the supernatant and IR analysis of silica+MOPA samples confirm that MOPA is retained, likely by the covalent interaction.

3.4.3   Reaction of Glycine and NAG with Fumed Silica
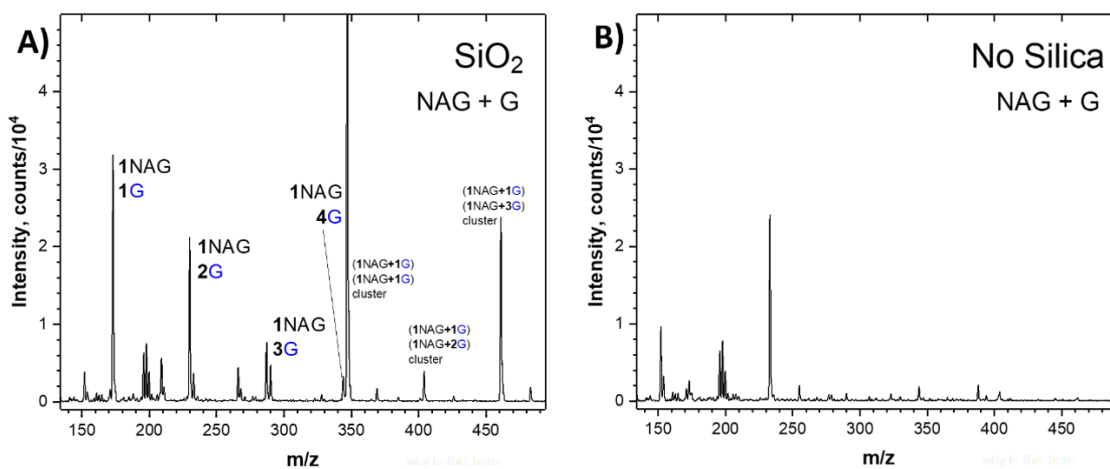
Figure 3-6   Mass spectra from dry-down reactions of NAG+G A) with, and B) without the inclusion of fumed silica. All products are terminated by a single NAG residue at the glycine N-terminus. Oligoglycine is only formed with silica, which facilitates peptide formation via silyl-ester aminolysis.

While the production of oligoglycine in the presence of MOPA requires silica and supports a repeated EAX process for G addition, direct demonstration of the ability for non-monomeric G to form a silyl-ester would further support this mechanism. To access the role of silica in the oligomerization of G with the LA-G analog NAG, reactions were carried out both in the presence and absence of the substrate. For the NAG+G system,

71

reaction at 85°C in evaporative conditions produces no oligopeptides when G and NAG are reacted alone, while NAG terminated oligo-glycine is formed in the presence of silica, with a G incorporation yield of 32% by NMR quantification (Table 3-2). Figure 3-6 depicts mass spectra for each condition with major products labeled. Both reactions share an acidic pH due to NAG, but neither NAG-terminating nor pure oligoglycine products are observed in the absence of silica. This experiment is consistent with, in a similar manner as the MOPA+G results, the theory that silica silanols can act as ester-forming nucleophiles are facilitating silyl-ester aminolysis which results in NAG-capped oligoglycine production.
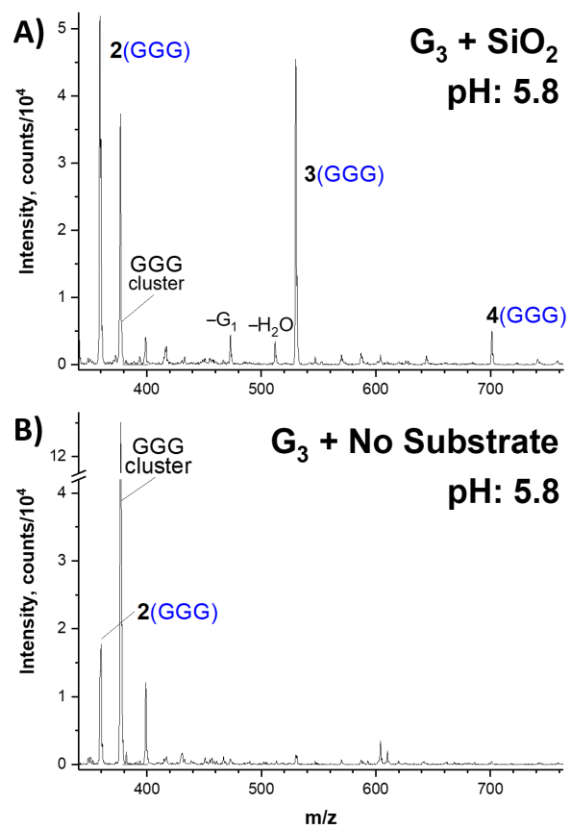
Figure 3-7   Mass spectra from dry-down reactions of MOPA+GGG at unbuffered pH=5.8 A) with, and B) without the inclusion of fumed silica. Poly-condensation of the GGG reactant occurs to a greater degree when silica is present. Both MOPA and NAG were excluded to demonstrate that non-monomeric G is capable of sustaining oligomerization via silyl-ester aminolysis.

The lack of oligoglycine products in silica-absent reactions sugests that without an ester-forming nucleophile, often provided by the α-hydroxy acid in a depsipeptide system, glycine and the model reatants MOPA and NAG are unable to facilitate oligomerization. When silica is added, the silanols fulfill that role of ester-forming nucleophile and allow for oligomerization via silyl-EAX. The inability of monomeric G to form silyl-esters suggests that an enabling characteristic of the reactants might be a carboxylic acid pK_a that

is closer to or exceeds the reaction pH. This is also closely related to the zwitterionic form of G. With the protonated amine so close to the carboxylic acid, as it is for monomer amino acids, electron density is inductively drawn towards the amine, contributing to glycine acidity. Consistent with this description, the protonated amine of a G trimer is sufficiently separated from the carboxyl moiety such that the pK_a is unlike monomeric G and instead, similar to NAG or MOPA. Therefore, GGG should be capable of esterifying with silica and sustaining oligomerization via EAX in a purely amino acid reaction, without the addition of monomeric G or the initiators NAG and MOPA.

Figure 3-7 shows MS analysis of silica+GGG dry-down reactions which demonstrate large abundances of GGG dimers and detectable levels of tetramers $(GGG)_4$. When silica is absent from the reaction, only $(GGG)_2$ are produced and at a lesser abundance relative to the starting reactant, represented by the GGG cluster. Due to the inclusion of either NAG or MOPA, all preceding experiments have been acidic, at pH~3. The pH is for silica+GGG reactions is higher at 5.8, which is known to be less accommodating for amide formation [114]. For unbuffered reactions, the solution pH increases over the course of the reaction, proportional to the extent of ester or amide formation. When the pH is established by a non-reactant molecule, i.e. not phosphoric acid, direct amide formation may dominate and account for the lack of GGG oligomerization differences in both silica-containing and silica absent conditions. However, the disparity of $(GGG)_n$ formation with silica at pH: 5.8 confers two points: a) tri-glycine is indeed a "pre-initiated" reactant in that silyl-ester formation is possible, unlike monomeric G, and b) the pH range for which oligomerization may proceed via silyl-EAX, without an α-hydroxy acid co-reactant, has been extended to a more neutral pH.
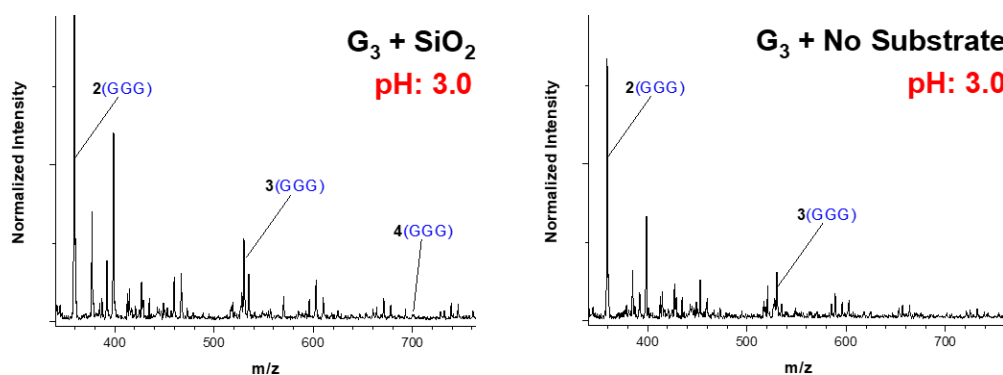
Figure 3-8 – Mass spectrum of G₃ incubated at pH=3.0, with and without the addition of fumed silica.

Reaction of silica+GGG was also performed at a phosphoric acid adjusted pH=3, (fig s5) were similar extents of GGG oligomerization were observed, regardless of silica inclusion. Figure 3-8 reports the MS analysis of tri-glycine (GGG) dry-down reaction at 85 °C for 6 days, with and without the inclusion of fumed silica (GGG at 100 mM, fumed silica added at 100 mg/mL, pH adjusted with phosphoric acid). As the extent of polymerization is similar between the conditions, the oligomerization mechanism likely does not involve silica directly and instead proceeds via direct, acid-catalyzed amide formation.

3.5 DRIFTS Analysis

3.5.1 Theory

The DRIFTS technique is well-suited for analysis of powder samples and sensitive to detect chemical motifs on the surface of moderate surface area substrates. IR spectra map the frequency of directly excited vibrational modes that are characteristic of certain chemical bonds and motifs. Considering a carboxyl functional group, there are three

relevant states that it can persist as: the ester (COOR), carboxylic acid (COOH) and carboxylate (COO⁻), Figure 3-9. By analysis of the carbonyl stretching region (C=O), all carboxyl moieties can be discerned, post-reaction, by IR analysis of products from silica included reactions.
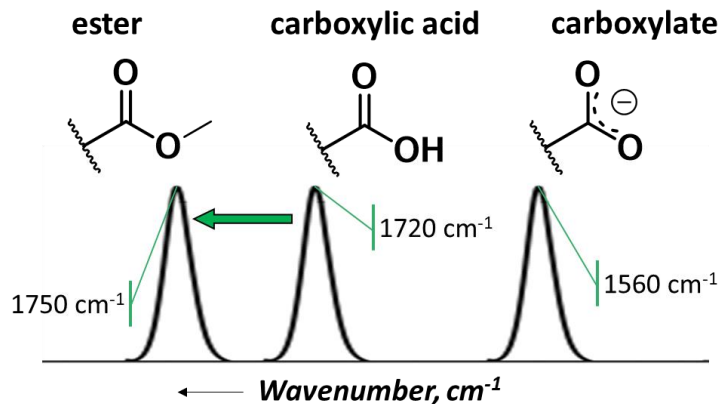
Figure 3-9   **Cartoon of infrared data corresponding to various carbonyl (C=O) environments, illustrating an exaggerated spectral shift due to esterification.**

Not only is IR analysis useful for examining the chemical state of the molecular reactants, but it is well-suited to examine the silica surface itself. At higher energy frequencies ~3500-3800 cm^{-1}, hydroxyl functionalities (–OH) are detected. Such motifs are associated with water, silanol groups, along with many terminations of oxide and silicate minerals.

3.5.2   Fumed Silica Reactions

3.5.2.1   MOPA
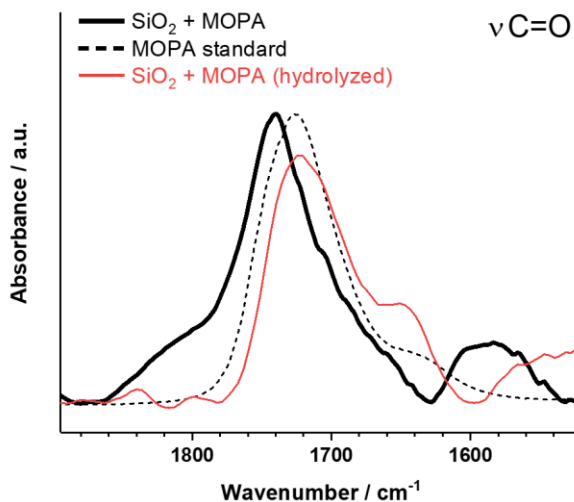
Figure 3-10   Infrared spectra of the carbonyl stretching region from a silica+MOPA reaction, incubated at 85 °C (peak at 1740 cm⁻¹). An unreacted MOPA standard is included (dashed line) to emphasize the hypsochromic shift due to ester formation (peak at 1723 cm⁻¹). The sample, post-hydrolysis (red line), presents a shift back to the unreacted carboxylic acid form (peak at 1724 cm⁻¹).

To determine if an activated ester, known to facilitate amide formation via EAX, is present or can form under these conditions, samples of silica+MOPA were incubated and analyzed via DRIFTS, summarized in Figure 3-10. The carbonyl stretching region (νC=O) from 1675-1775 cm⁻¹ is diagnostic of the persistent molecular state for the carboxyl moiety. The dotted line spectrum was collected from a neat, unreacted sample of liquid MOPA and represents the carboxyl moiety in its native carboxylic acid form (1723 cm⁻¹). After incubation with silica, the carbonyl peak exhibits a hypsochromic shift of 17 cm⁻¹, implying a change in molecular state from a carboxylic acid to an ester (1740 cm⁻¹) [77, 104, 115-

117], depicted in Figure 3-11. This signifies the ability for MOPA to form a silyl-ester and create an activated amide bond formation site on a silica surface. Additional confirmation of a covalent interaction was achieved by hydrating and incubating the same silica+MOPA sample in a closed vessel for 12 hours. Since evaporation could not take place, it was expected that all ester linkages hydrolytically cleaved. The sample was then allowed to air dry at room temperature in preparation for re-analysis. This result, shown as the red line, shows a restoration of the carbonyl peak back to the characteristic carboxylic acid stretching frequency of unreacted MOPA. This both corroborates the assertion that the observed hypsochromic shift is characteristic of silyl-ester formation and demonstrates the reversibility of the chemisorption.
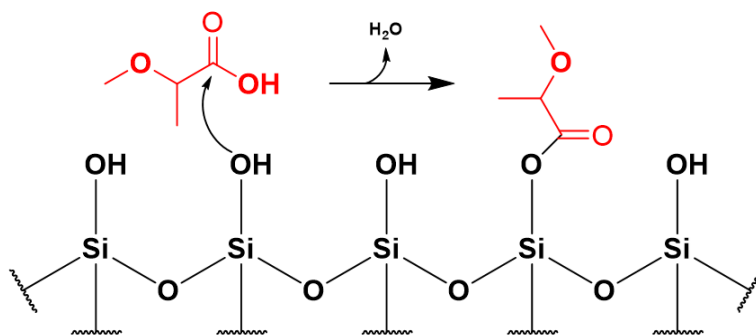
Figure 3-11   Scheme describing the formation of a silyl-ester between MOPA and fumed silica.

Considering that LA is known to extensively poly-esterify under these conditions, it is reasonable that MOPA is also able to esterify, especially as the pKa for MOPA is very close to that of LA. It is likely that the lower carboxyl acidity for these molecules, relative to glycine, and the lack of available zwitterionic forms are the distinguishing features that allow these three molecules and not amino acids to esterify with a silica surface. Additionally, MOPA is observed in the carboxylic acid form and not as the carboxylate

anion, post-hydrolysis. Such anionic adsorption has been observed on substrates with a higher isoelectric point that present a net positive surface charge at the reaction pH=3 [75].
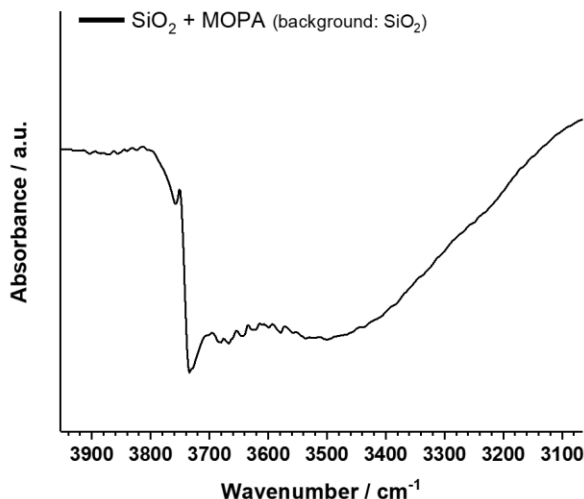
Figure 3-12   Infrared spectra of the silanol region for MOPA, incubated with fumed silica (peak at 3736 cm^{-1}).

For the same silica+MOPA sample incubated at 85 °C to evaporation (MOPA at 100 mM, fumed silica added at 100 mg/mL), IR analysis was applied to a native substrate feature in Figure 3-12. This spectral region includes the hydroxyl (-OH) stretching mode for silanol (Si-OH) moieties on the surface of silica, with isolated silanols represented by the narrow peak at 3736 cm^{-1}. This spectrum represents the subtraction of an unreacted silica sample from a post-reaction silica+MOPA sample. The negative signal is due to a decrease of isolated silanols in the post-reacted sample, relative to the unreacted silica. The decrease in abundance can be understood as consumption of these motifs by silyl-ester formation. Therefore, along with the shift in carbonyl signal, this result confirms that

MOPA is able to esterify with fumed silica and facilitate G oligomerization via ester-aminolysis.

3.5.2.2 NAG
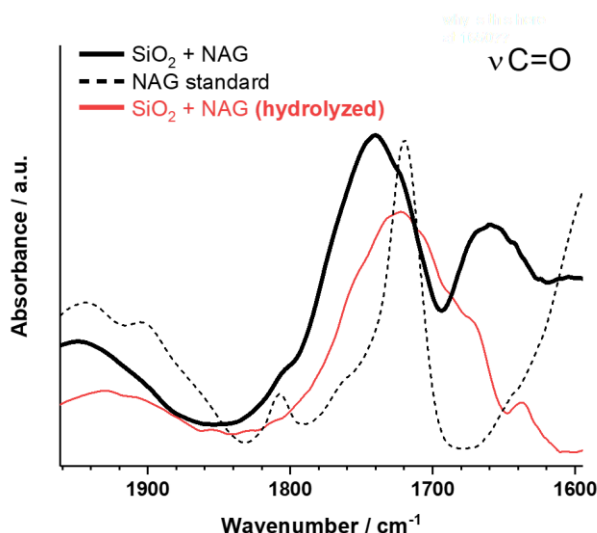
Figure 3-13   Infrared spectra of the carbonyl stretching region from a silica+NAG reaction, incubated at 85 °C (peak at 1740 cm^{-1}). An unreacted NAG standard was included (dashed line) to emphasize the hypsochromic shift due to ester formation (peak at 1720 cm^{-1}). The same sample, post-hydrolysis (red line), demonstrates a shift back to the unreacted carboxylic acid form (peak at 1723 cm^{-1}).

To confirm silyl-ester formation by direct observation, DRIFTS was employed to analyze samples of incubated silica+NAG. Figure 3-13 shows the carbonyl stretching region for the carboxyl moiety of NAG. The dashed line is an unreacted NAG sample, representing the native carboxylic acid state (1720 cm^{-1}). After incubation with silica, the peak exhibits a hypsochromic shift of 20 cm^{-1}, signifying ester formation (1740 cm^{-1}). Such a shift has been identified as a characteristic of esters, compared to carboxylic acids moieties [77, 104, 115], depicted in Figure 3-14. The transformation was confirmed by a gentle hydrolysis and air drying procedure, which showed a restoration of the carbonyl

peak to the native carboxylic acid form. It is important to note that NAG and G differ in their acidity, 3.7 and 2.4 respectively. Due to N-acetylation, NAG does not have a protonated amide that is electron withdrawing, and does not inductively increase the carboxylic acid acidity. NAG is thus more likely to have a protonated carboxyl group and persist in a form amenable for ester formation.
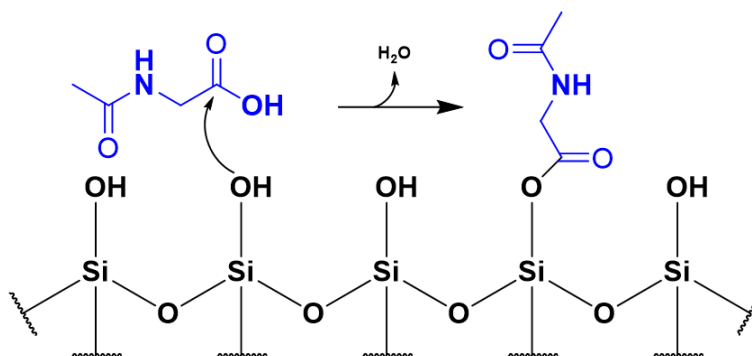
Figure 3-14   Scheme describing the formation of a silyl-ester between NAG and fumed silica.

Figure 3-15 spectrum of silica with NAG incubated at 85 °C to evaporation (NAG at 100 mM, fumed silica added at 100 mg/mL). This spectral region includes the hydroxyl (-OH) stretching mode for silanol (Si-OH) moieties on the surface of silica, with isolated silanols represented by the narrow peak at 3735 cm^{-1}. Similar to Figure S 4, this spectrum represents the subtraction of an unreacted silica sample from a post-reaction silica+NAG sample. For this reaction, the signal is also negative due to a decrease of isolated silanols in the post-reacted sample, relative to the unreacted silica. The decrease in abundance indicates that silanol sites were consumed over the course of the reaction. The specific character of that consumption is confirmed by the carbonyl shift, and refers to silyl-ester formation. Therefore, this result supports the hypothesis that NAG is able to esterify with fumed silica and is capable of facilitating G oligomerization via ester-aminolysis.

81
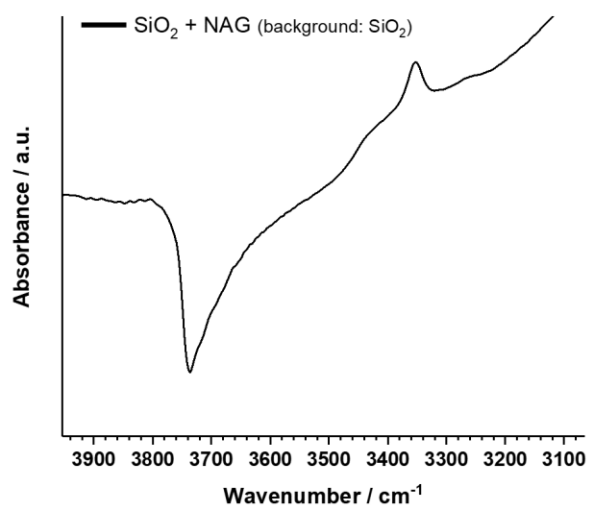
Figure 3-15   Infrared spectra of the silanol region for NAG, incubated with fumed silica (peak at 3735 cm^{-1}).

3.5.2.3   Glycine
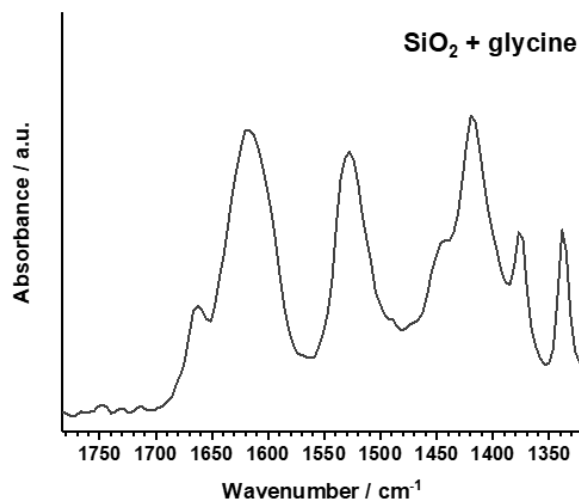
Figure 3-16   Infrared spectra of the carbonyl region for G, incubated with fumed silica.

Figure 3-16 IR analysis (DRIFTS) of an unbuffered fumed silica+G dry-down reaction at 85 °C for 6 days, (G at 100 mM, fumed silica added at 100 mg/mL). This spectrum demonstrates that the zwitterionic form dominates for adsorption and remains so post-reaction. The peaks at (1616 cm^{-1}) and (1527 cm^{-1}) are associated with the protonated amine (NH_3^+), while the peak at (1418 cm^{-1}) corresponds with a carboxylate carbonyl moiety (COO^-). At 1662 cm^{-1} a peak that does not appear in unreacted G powder is present, and associated with an amide motif, commonly referred to as "amide i." Though amide formation is demonstrated by MS and further confirmed by the amide i peak, no peak associated with ester formation is detected (1740-1770 cm^{-1}). This observation suggests that the chemical transformation responsible for the amide signal occurred via direct amide formation and not ester aminolysis. Further evidence that ester aminolysis did not contribute to the amide formation can be found within the silanol region, summarized in Figure 3-17.
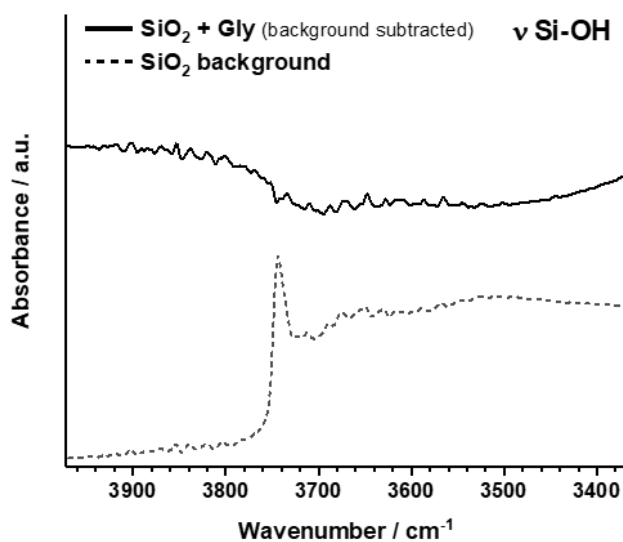
Figure 3-17 Infrared spectra of the silanol region for G, incubated with fumed silica.

For the silica+G reaction, the silanol region was analyzed (Figure 3-17) in addition to the carbonyl region. The solid line of panel B represents the subtraction of an unreacted silica spectrum from the spectrum of a post-reaction silica+G sample. The unreacted silica spectrum used as the background is included as a dashed line for reference. The signal is nearly flat, indicating that no change in abundance of silanols, specifically the isolated silanols represented by the narrow peak at 3740 cm^{-1}. For ester aminolysis to occur, esters must first be formed. Within the reaction of silica+G, the only potential ester-forming nucleophile are silanols, which would be consumed if esterification was achieved with glycine. Consumption of terminal silanols would result in a "negative" signal with background subtraction. Therefore, this experiment demonstrates that while minor amide formation may occur between G when incubated with silica, it does not proceed via an ester aminolysis mechanism.

3.5.3 Analysis of various Silica Substrates

The participation of silica in G oligomerization via EAX has been demonstrated. The formation of silyl-esters, which may only occur if the substrate is silanol terminated, is apparently a necessary characteristic. Additionally, signal depletion of silanol groups, post-reaction, with MOPA and NAG suggest consumption of those groups by reaction. The aforementioned experiments utilized fumed silica, which has strained and diverse terminations [118-120] relative to a more mineral-like fused quartz, despite both possessing the same empirical formula, SiO_2.
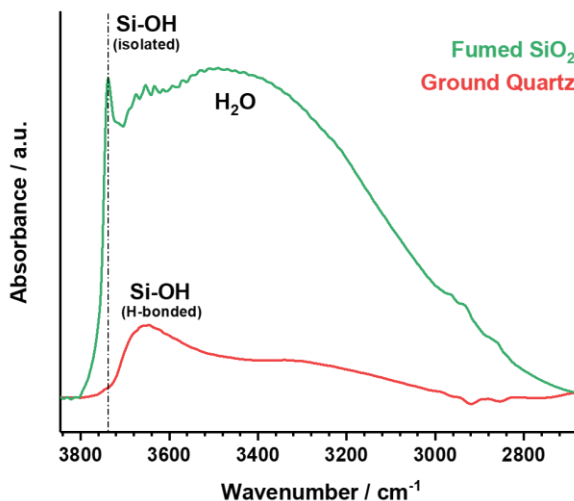
Figure 3-18   Infrared spectra of A) the -OH and silanol stretching region from samples of fumed silica and quartz, incubated at similar conditions with only water. The sharp peak associated with isolated silanols is absent for quartz.

IR analysis in Figure 3-18 illustrates these differences, showing an abundance of *isolated* silanol terminations [120, 121] for fumed silica (3740 cm^{-1}), while quartz presents H-bonding silanols ($\sim$3660 cm^{-1}) and a complete absence of isolated silanol terminations

(Figure 3-19). With this distinction made, quartz can act as a control substrate which is identical in composition but distinct in surface chemistry.

Fumed silica SiO$_2$ **Fused quartz SiO$_2$**
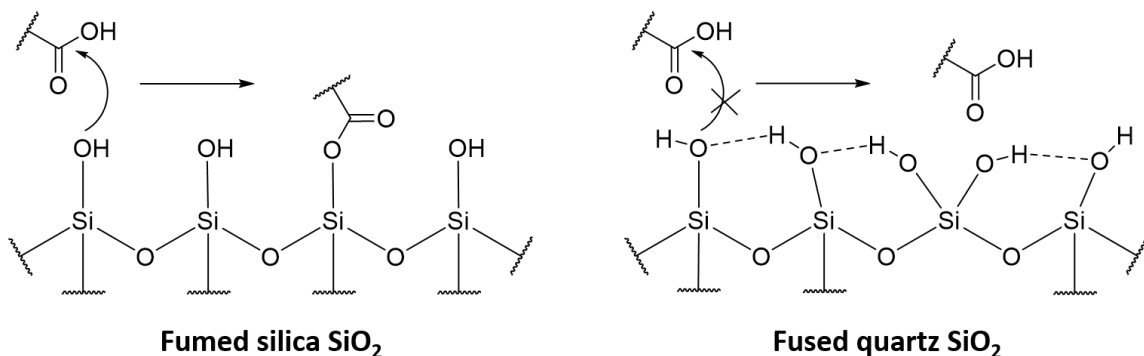
Figure 3-19 – Scheme depicting the distinction between fumed silica and fused quartz in terms of the intermolecular interactions of the terminal silanol functionalities and subsequent reactivity with organic acid molecules.

3.5.4   Quartz Reactions

To directly confirm the role of silanol moieties in the EAX process, a sample of fused quartz was reacted in similar conditions with MOPA and NAG. Considering the results of silica and glycine reactions in addition to the consumption of isolated silanols, ester formation is not expected to proceed on quartz due to decreased nucleophilicity of H-bonded silanols.
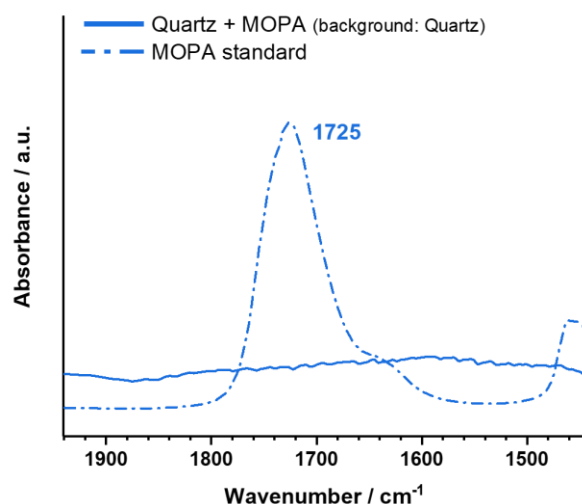
Figure 3-20 – Infrared spectra of the carbonyl region from dry-down reactions of quartz+MOPA, with unreacted standards (dashed lines) included for comparison.

When quartz+MOPA is incubated, much like substrate absent samples, MOPA evaporates and is not detected by IR, Figure 3-20. This corroborates the claim that the volatile MOPA is retained only by esterification or incorporation into a G peptide. For quartz+NAG, Figure 3-21, the post-incubation carbonyl stretch does not shift, inferring a lack of esterification. The IR spectra demonstrates that NAG is retained in the native carboxylic acid form and not as a carboxylate, signifying that quartz does not have a significantly higher PZC compared to fumed silica and therefore does not present a positive surface charge.
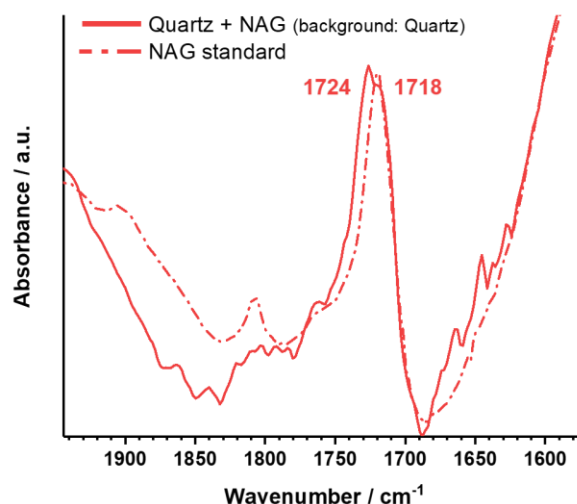
Figure 3-21 – Infrared spectra of the carbonyl region from dry-down reactions of quartz+NAG, with unreacted standards (dashed lines) included for comparison.

A quartz+G reaction at 85 °C for 6 days, (G at 100 mM, quartz added at 500 mg/mL) was also analyzed by DRIFTS, Figure 3-22, and showed no sign of esterification, similar to fumed silica results. This spectrum demonstrates that the zwitterionic form dominates post-reaction; the shoulder at 1609 cm^{-1} and peak at 1528 cm^{-1} are associated with the protonated amine (NH$_3^+$), while peaks at 1588 cm^{-1} and 1417 cm^{-1} are similar to known carboxylate (COO$^-$) frequencies, antisymmetric and symmetric respectively.[57] Little abundance is present in the amide i region near 1650 cm^{-1}, suggesting G oligomerization of a lesser extent than with fumed silica. Additionally, no peak associated with ester formation is detected (1740-1770 cm^{-1}), and confirms that G exclusive oligomerization via ester aminolysis is not supported on a quartz surface.
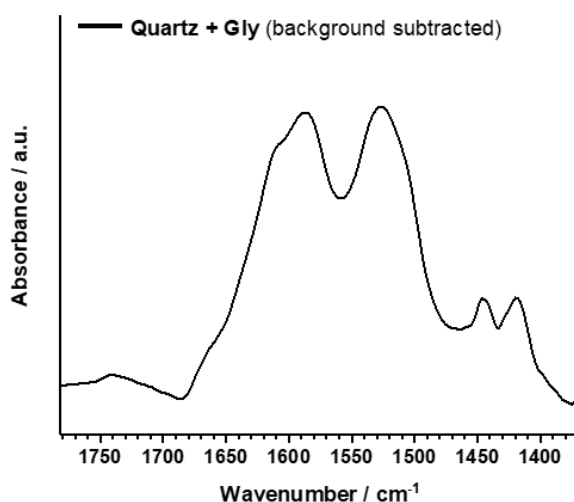
Figure 3-22 – Infrared spectra of the carbonyl region for G, incubated with fused quartz.

Summarizing the MOPA, NAG and G reactions with quartz, it appears that there is a lack of covalent interaction between quartz and the model reactants. This observation, coupled with the absence of isolated silanol features from bare quartz samples, suggests that isolated silanols should be considered the ester-forming nucleophile.

3.6   NMR Analysis

The quantitative approach applied to the silica+G with depsipeptide component analogs draws inspiration from the silica+G+LA NMR analysis in section 2.4.2. While there is inherently less sequence complexity, as all oligomers follow the same form, e.g. 1MOPA+nG, the spectra can still be difficult to interpret. Combining spectra of starting materials, synthesized standards and using trends established in section 2.4.2, certain yields can be determined.
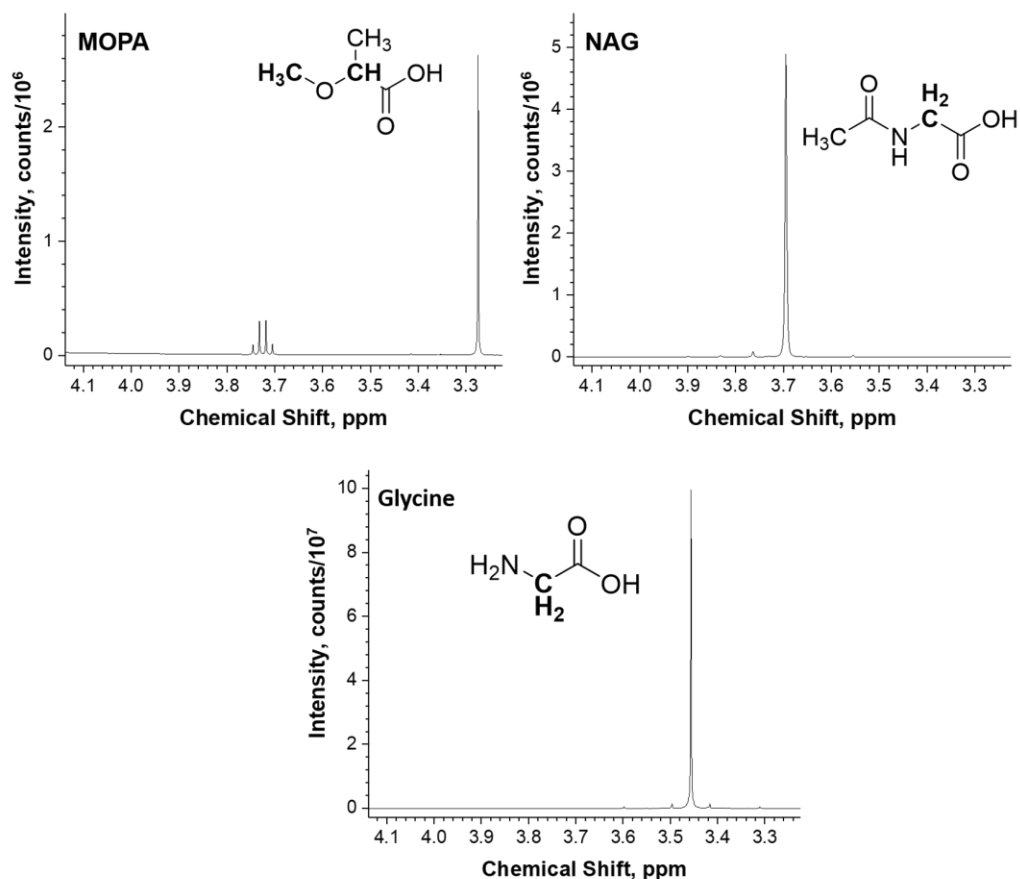
Figure 3-23   NMR spectra of MOPA, NAG and glycine monomers at pH=7.0, calibrated using an external standard.

^{1}H-NMR spectra for pure samples of 2-methoxypropionic acid (MOPA), N-acetylglycine (NAG) and glycine (G) are presented in Figure 3-23 for reference. The resonances included in the figure are emboldened in their molecular representation; the MOPA non-methoxy CH_3 and the NAG acetyl CH_3 groups are omitted. Recording the

spectra for each starting material provides for a better identification of signals belonging to reaction products when the crude reactions are analyzed.

MOPA: ^{1}H-NMR (500 MHz, D$_2$O) δ 3.73 (q, 1H, J = 6.8 Hz), δ 3.27 (s, 3H), δ 1.27 (d, 3H, J = 6.8 Hz)

NAG: ^{1}H-NMR (500 MHz, D$_2$O) δ 3.70 (s, 2H), δ 1.99 (s, 3H)

G: ^{1}H-NMR (500 MHz, D$_2$O) δ 3.46 (s, 2H)
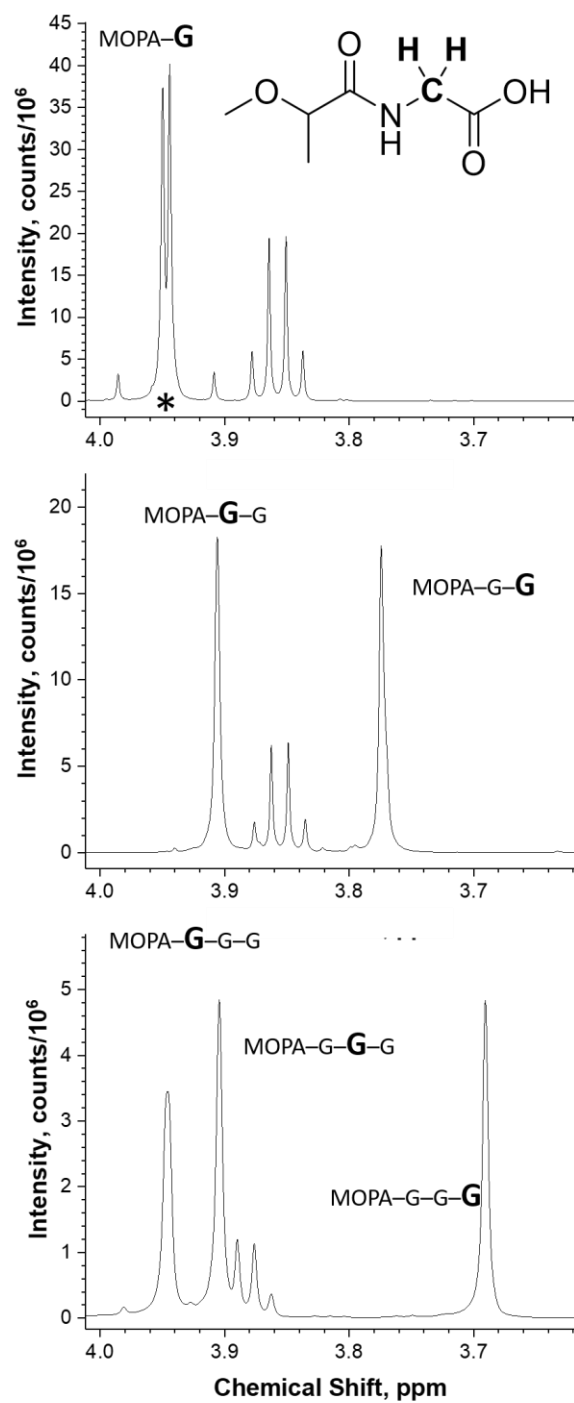
Figure 3-24   NMR spectra of MOPA–nG standards at pH=7.0, calibrated using an external standard.

Standards for MOPA-capped glycine, di-glycine and tri-glycine were synthesized as described in Appendix A. Analysis of these standards by NMR (Figure 3-24) at similar conditions allows for identification of several key motifs expected in the silica+MOPA+G reaction. The MOPA methine (CH) comes as a quartet and is mostly unperturbed by subsequent G addition, remaining at 3.86 ppm and only shifting to 3.90 ppm for the trimer species. The positions of the MOPA methoxy methyl (O-CH$_3$) and methyl (CH$_3$) groups are also invariant with subsequent G addition, at ~3.32 ppm and 1.28 ppm respectively. The G methylene (CH$_2$) groups vary in position and splitting depending on proximity to the oligomer termini, and are therefore significantly more diagnostic of the connectivity for reaction products.

The MOPA–G molecule, has a G methylene group with diastereotopic protons, due to their vicinity to chiral MOPA, which has been discussed for a G and lactic acid system.[107] A MOPA–G heterodimer, and to a lesser extent any MOPA-adjacent G residue, will present as a doublet of doublets, from 3.99-3.91 ppm, with similar coupling constants.

MOPA–G: ^{1}H-NMR (500 MHz, D$_2$O) δ 3.95 (dd, 1H, J = 20.7, 17.9 Hz), δ 3.86 (q, 1H, J = 6.8 Hz), δ 3.32 (s, 3H), δ 1.28 (d, 3H, J = 6.9 Hz)

The MOPA–GG molecule, has two G methylene groups that are associated with either the MOPA-adjacent or C-terminus residue. While the peak at 3.91 ppm appears as a singlet, a small peak at 3.94 ppm can be interpreted as part of the diasteriotopic system for the MOPA-adjacent G residue, as the minor coupling constant for this doublet is 17.1 Hz and similar to the MOPA–G standard. For a purely oligoglycine molecule, the furthest up-

field resonance is associated with the C-terminus residue [107], and is therefore the motif assigned to the peak at 3.77 ppm. Included below are the chemical shifts for the MOPA-adjacent glycine residue stated in two way, depending if it is considered a discernable diastereotopic system or not. This distinction ultimately does not affect quantitation, but serves to strengthen the claim that the furthest down-field resonance is indeed MOPA-adjacent. The similarity of the MOPA–GG dd J value to the lesser MOPA–G J value suggests that this assignment is correct.

MOPA–GG: ^{1}H-NMR (500 MHz, D$_2$O) δ 3.91 (s, 2H) or (dd, 1H, J = 17.1 Hz), δ 3.86 (q, 1H, J = 6.8 Hz), δ 3.77 (s, 2H), δ 3.30 (s, 3H), δ 1.28 (d, 3H, J = 6.9 Hz)

The MOPA–GGG molecule, includes a G methylene of a third distinction, the internal residue, which is surrounded by other G on both sides. For a purely oligoglycine molecule, a more central position in the oligomer is associated with an increasingly down-field resonance, though the MOPA-adjacent residue does not adhere to this convention. Considering that the peak at 3.94 ppm is similar to the MOPA-adjacent residue from the MOPA–GG molecule, in addition to the small peak at 3.98 ppm that could represent a doublet in a diastereotopic system with a coupling constant of 18.4 Hz, the internal-G motif is assigned to the peak at 3.90 ppm.

MOPA–GGG: ^{1}H-NMR (500 MHz, D$_2$O) δ 3.94 (s, 2H) or (dd, 1H, J = 18.4 Hz), δ 3.90 (s, 2H), δ 3.88 (q, 1H, J = 6.8 Hz), δ 3.69 (s, 2H), δ 3.32 (s, 3H), δ 1.28 (d, 3H, J = 6.9 Hz)
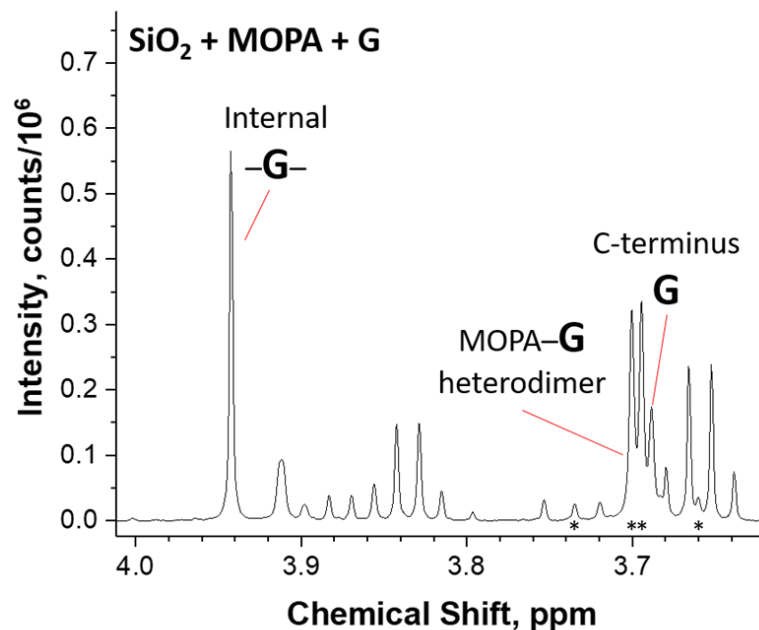
Figure 3-25   NMR spectra of silica+MOPA+G, at pH=7.0, calibrated using an external standard.

Products from incubation of silica+MOPA+G at 85 °C in an evaporative environment were analyzed by NMR (Figure 3-25). Though standards of MOPA–nG were prepared and analyzed at a similar sample pH, some peaks are significantly shifted. However, using the relational trends observed for the MOPA–nG standards, motif resonances can still be assigned. The MOPA–G heterodimer is most unique, as the diastereotopic methylene system comes as a recognizable doublet of doublets with a coupling constant consistently $J = 17$-18 Hz. The only such peak set that shares this splitting trait is centered at 3.69 ppm, with components indicated by (∗). The C-terminus residue should come as the most up-field singlet resonance and is therefore identified as

the peak at 3.58 ppm. It should be noted that while the heterodimer G residue is technically also the C-terminus, it is considered distinct, as the chemical shifts are consistently discernable. Internal G residues should have the most down-field singlet methylene resonances and are therefore assigned to the peak at 3.94 ppm. The MOPA methine, $J =$ 6.8, for the unreacted monomer is centered at 3.66 ppm, but at least two other instances of this quartet are present and likely represent MOPA bound to one or more G residues. As a result of these motif identifications, yields of G incorporation and a course partitioning of yields for heterodimeric and oligoglycine species can be achieved, summarized in Table 3-1.

Table 3-1   **NMR yields for silica+MOPA+G reaction at 85 °C**

Glycine Connectivity Designation		Percent Yield
Total Incorporated G		15.1
Heterodimer	(MOPA–**G**)	6.7
Internal	(–**G**–)	5.9
C-terminus	(**G**–G)	2.5

Heterodimer: δ 3.69 (dd, 1H, $J = 20.2, 17.3$ Hz)
Internal: δ 3.94 (s, 2H)
C-terminus: δ 3.68 (s, 2H)

Yields were calculated as a ratio of the integrated area for each G motif and the sum of integrations for all G species, including unreacted G monomer, assuming no G loss. Substantial loss of MOPA due to volatility was observed, so independent calculation of MOPA incorporation could not be achieved. However, the integration from the discernable non-monomer MOAP methine quartets is within a 10% difference to the sum of heterodimeric and C-terminus G signal, as expected. Comparison of these yields to those of homogeneous reactions of LA and G [33], contextualizes this process as firmly reasonable and not an untenable rare reaction.
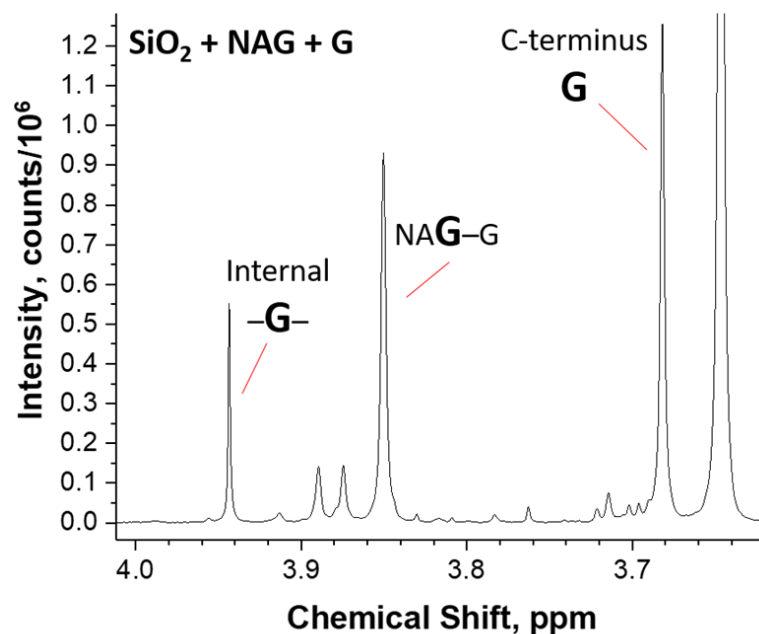
Figure 3-26   NMR spectra of silica+NAG+G, at pH=7.0, calibrated using an external standard.

Products from incubation of silica+NAG+G at 85 °C in an evaporative environment were analyzed by NMR (Figure 3-26). Though standards of NAG–*n*G were not synthesized, the same relational trends from the MOPA standards and reaction with G are relevant for this system as well. For NAG, the acetyl group does not cause nonequivalence for the methylene protons, so all G resonances present as singlets. The peaks at 3.94 ppm and 3.62 ppm are similar to the internal-G and C-terminus residues, respectively, so are assigned the same as the MOPA system. Also like the MOPA analysis, reaction of the NAG monomer by G addition causes a down-field shift that is represented by the peak at 3.85 ppm. This methylene group is not from the initial G reactant, but the G component of

97

the NAG molecule. From these motif identifications, yields of G incorporation and species

with multiple G–G linkages can be achieved, summarized in Table 3-2.

Table 3-2 **NMR yields for silica+NAG+G reaction at 85 °C**

Reactant Connectivity Designation		Percent Yield
Total Incorporated Glycine		32
Internal	(–**G**–)	6
C-terminus	(–**G**)	26
Total Incorporated NAG	(NA**G**–G…)	22

Internal:	δ 3.94 (s, 2H)
C-terminus:	δ 3.62 (s, 2H)
Incorporated NAG:	δ 3.85 (s, 2H)

Yields for G motifs and total incorporation were calculated as a ratio of the

integrated area for each G motif and the sum of integrations for all G species, including

unreacted G monomer, assuming no G loss. Since NAG is non-volatile, the total

incorporation yield was also calculated in the same as for G. Ideally, this value would

exactly match the total G incorporation yield, however the yields are within a 20%

difference. These yields are somewhat close to those regarding the silica+G+LA system,

and presents silyl-ester aminolysis as a viable mechanism for depsipeptide production

3.6.5 Reaction of Glycine and Depsipeptide Analogues with Quartz
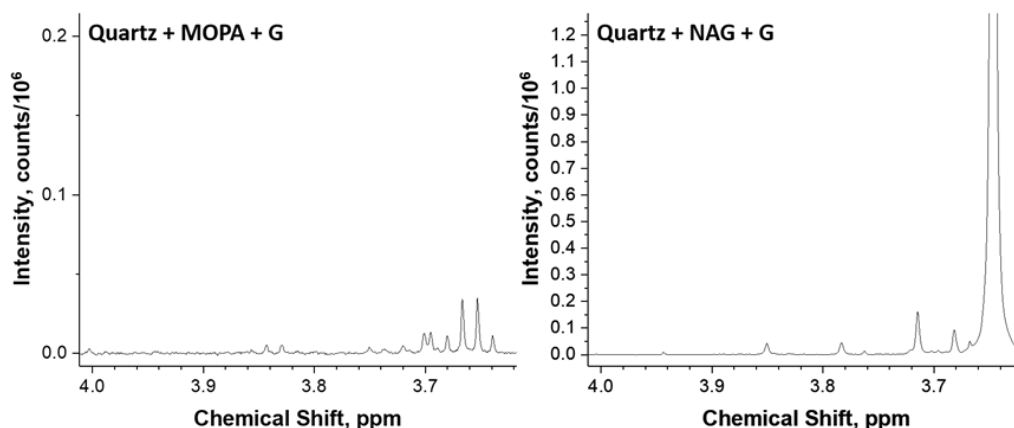
Figure 3-27   NMR spectra of quartz reactions, at pH=7.0, calibrated using an external standard.

Products from incubation of quartz+MOPA+G and quartz+NAG+G at 85 °C in an evaporative environment were analyzed by NMR (Figure 3-27). From IR analysis of quartz+MOPA and quartz+NAG reactions, it is known that these initiator molecules are not able to esterify with the hydrogen-bound silanol network and thus will not facilitate G oligomerization via silyl-ester aminolysis. To confirm this inability, reactions and analyses identical to those for silica samples were conducted to quantify oligoglycine production in the presence of quartz. Assignments derived from the silica with MOPA and NAG analyses are valid for quartz samples as well. Reaction with quartz does not produce significant levels of reacted MOPA or NAG and essentially no oligoglycine; yield of MOPA consumption, compared to present G monomer, is ~1%, while NAG consumption is slightly higher at ~2%. This analysis supports the claim that silyl-ester aminolysis and glycine oligomerization require isolated, not hydrogen bonding, silanols as ester-forming nucleophiles.

3.7   Proposed Mechanism of silyl-ester aminolysis

Drawing from all model reactions between glycine and the analog molecules, it is clear that silica, and specifically the isolated silanols are required for amide formation. This necessity of silica for production of oligoglycine with MOPA or NAG suggests that oligomerization proceeds via ester-aminolysis where fumed silica is a direct participant. A proposed mechanism for N-capped oligoglycine is summarize by Figure 3-28, using MOPA as an example molecular analog, however, NAG could also be used in this scheme.
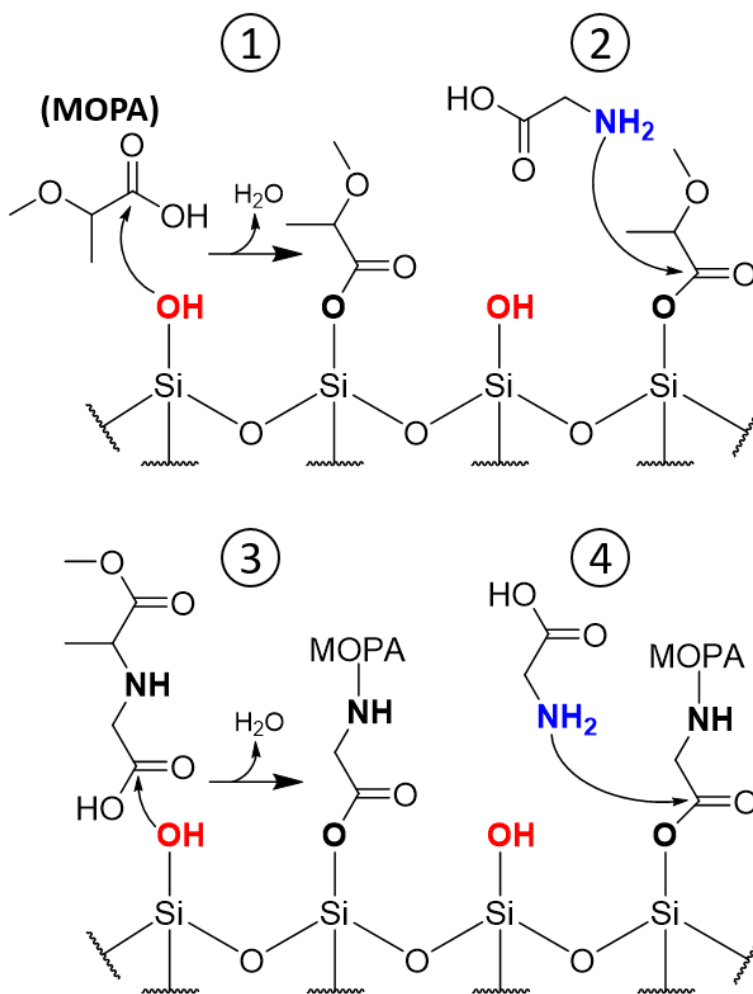
Figure 3-28 – Mechanism proposed for glycine oligomerization via silyl-ester aminolysis, initiated by esterification of MOPA with terminal silanol moieties. This pathway is also valid if NAG is substituted in place of MOPA.

Terminal silanol functionalities act as nucleophiles that can produce a silica surface decorated in silyl-esters when reacted with MOPA, NAG or α-hydroxy acids. Once MOPA or NAG esterify with a silanol, the G amine is able to attack the now more electrophilic carbonyl via silyl-ester aminolysis and form an amide-linked heterodimer. This process displaces the covalent bond between the surface and initial esterified molecule. For oligoglycine production, i.e. multiple contiguous G residues, a silyl-ester must be reformed at the carboxyl group of the terminal G residue preceding each subsequent G addition. While monomeric G lacks the ability to achieve the activated ester motif in these conditions, a G residue incorporated into an oligomer is able to repeat steps 3 and 4, due to a decreased carboxyl acidity. This is directly supported by the ability of NAG, which is analogous to an amide linked G heterodimer, to esterify with silica. By this process, NAG and MOPA act as initiators for G oligomerization via silyl-EAX, only esterifying with a silanol once per oligomer chain.

The potential exists that there are mineral characteristics, in addition to isolated surface hydroxyl functionalities, that are necessary for surface ester aminolysis to proceed on other substrates. For fumed silica, the PZC was 3.0, such that the surface was essentially net neutral, and certainly not positively charged, for the initial phase of the reaction. It may the case that matching solution pHs to PZC, along with reactive terminal sites are both prerequisites for amino acid poly-condensation by surface-ester aminolysis.

This scheme may also be applied to interpret the amino acid enrichment observed with the LA+G depsipeptide reaction. Since LA can esterify with silica, it may be the case that a large portion of the available LA become surface esterified in an early stage of the reaction. Confronted by a silica surface decorated with activated sites, heterodimer formation with a glycine molecule could occur via silyl-ester aminolysis. What might account for a higher ratio of G:LA is a reduced number of mobile LA molecules, and therefore less LA–LA esters formed, assuming transesterification at a silyl-ester site is minimal. Furthermore, this result could not be reproduced by simply increasing the initial amount of glycine relative to LA, as it is not the absence of LA in the system, but the preoccupation of LA as activated motifs for EAX that could account for amino acid enrichment in depsipeptides in the presence of silica.

3.8   Conclusions

In summary, oligomerization of glycine is able to proceed within a depsipeptide-like reaction via silyl-ester aminolysis on a fumed silica surface under plausible prebiotic conditions. To allow for exclusive investigation of surface chemistry, the typical α-hydroxy acid and amino acid components of a depsipeptide system were exchanged for molecular analogs that lack polymerizing and cyclizing capabilities, e.g. 2-methoxypropionic acid (MOPA) and N-acetylglycine (NAG). After incubation at 85 °C, ester formation between fumed silica and both molecular analogs was confirmed via infrared spectroscopy, while monomeric glycine did not exhibit signs of esterification with silica. When glycine was added as a co-reactant to either analog, oligoglycine formed only in the presence of silica, confirmed by mass spectrometry. This observation suggests that once an initial activated ester is formed by MOPA or NAG, which cannot be achieved without silica or by glycine

and silica alone, oligomerization can proceed. Consequently, oligoglycine can be formed in the presence of silica from a purely amino acid reaction when a glycine trimer is used in place of the monomer. Analysis of a distinct SiO_2 sample of quartz demonstrated no ability to esterify with MOPA or NAG due to H-bonded, in lieu of isolated, silanol terminations. While fumed silica is well suited for ester-aminolysis in depsipeptide systems, it is likely not the only substrate that can support this mechanism. Examination of the ability of a diverse cohort of mineral substrates to esterify with model reactants like MOPA, NAG, or similar analogs will identify mineral characteristics that are necessary for this chemistry and therefore predict formation of oligomeric products from depsipeptide reactions. Overall, ester-aminolysis is a robust route for the oligomerization of amino acids and prebiotically abundant α-hydroxy acids that may be better facilitated by certain mineral substrates, e.g. silica, that are otherwise not well-suited to catalyze direct amide formation.

CHAPTER 4.   ASSESSMENT OF SURFACE ESTERIFICATION ON OXIDE AND SILICATE SUBSTRATES

4.1   Background

The research accounts so far have described in detail several scenarios of depsipeptide formation on fumed silica, however these methods and experimental designs have yet to be applied towards a more generalized cohort of mineral substrates. The experiments discussed in this chapter will share a similar chemical system with the aforementioned experiments, but will substitute a battery of various prebiotic minerals in place of fumed silica. The new cohort of minerals will be comprised of metal oxides and various silicates, see Table 4-1. The components of this list are motivated in part due to their prevalence in prebiotic mineral reaction literature [59], mix of oxide and hydroxide classes, and point of zero charge (PZC) parameters that span from ~3, the pH of HA+AA reactions, to much higher, at ~10. As noted above, the absence of isolated silanol groups for ground quartz is a distinction that drastically affects reactivity, despite compositional similarity. Titania and zirconia are chosen as two examples of metal oxides with mid to high PZC; it should be expected that their results resemble one another if the tested mineral characteristics are highly predictive of depsipeptide interactions. The two Al-containing minerals, corundum (Al_2O_3) and gibbsite ($Al(OH)_3$), are intended to offer insight regarding reactivity in oxide versus hydroxide species. In addition to being included in a prominent research paper that addresses thermal condensation of glycine on various mineral substrates, Fe-containing mafic silicates might be abundant species on Earl Earth [59]. Lastly, kaolinite and Montmorillonite will be included due to their prominence in prebiotic

mineral reaction literature, complex composition, and their likely abundance on early Earth. The comparison of glycine exclusive reactions to glycine with α-hydroxy acid-like or non-monomer EAX initiators will offer further insight regarding the extent of viable substrates for the depsipeptide system.

Table 4-1   List of all substrates studied in this chapter, including common name, ideal chemical formula and typical point of zero charge (PZC).

Substrate	Formula	PZC[a]
Fumed Silica	SiO_2	3
Albite	$NaAlSi_3O_8$	2
Alumina	Al_2O_3	9
Aluminum Hydroxide	$Al(OH)_3$	9
Dickite	$Al_2Si_2O_5(OH)_4$	< 3
Enstatite	$MgSiO_3$	4-6
Fayalite	Fe_2SiO_4	4-6
Forsterite	Mg_2SiO_4	3-5
Kaolinite	$Al_2Si_2O_5(OH)_4$	< 3
Montmorillonite-Ca	$(Ca)_{0.33}(Al,Mg)_2(Si_4O_{10})(OH)_2 \cdot nH_2O$	3
Titania	TiO_2	5-6
Vanadium oxide	V_2O_5	1.5
Zeolite	$(Ca,Na_2,K_2)Al_2Si_{10}O_{24}$	< 2
Zirconia	ZrO_2	5-6

a) Values for points of zero charge were taken from reference [70]

Incubation of a mineral with either MOPA or NAG and subsequent analysis by IR indicates the ability for surface esterification, and is predictive of the ability to produce poly-G via EAX in systems without α-hydroxy acid present. The model α-hydroxy acid reagent, MOPA, is used as an analog for lactic acid. It differs from LA in that is cannot form intermolecular ester bonds, e.g. and LA dimer, and is therefore restricted to forming only interfacial esters. In previous experiments with fumed silica, the carbonyl vibrational

frequency appeared hypsochromic shifted by ~20 cm^{-1} relative to the neat monomer liquid. This shift indicated transformation of the carboxyl group from a carboxylic acid to an ester, specifically a silyl-ester. Stabilization of carboxylates on metal oxides have been previously reported [75] and is expected under these conditions and is in agreement with an account of G oligomerization on TiO$_2$ and highlights the diversity in oligomerization pathways accessible for various minerals [122].

4.2   Experimental

Dry-down reactions proceeded via the addition of 1:1 mixtures of 100 mM aqueous solutions of MOPA or NAG and G or 100 mM aqueous solutions of MOPA or NAG to each substrate. Solutions were added to the substrates at 1 mL/100 mg powdered mineral, though the surface area for each of these reactants are significantly distinct.

Infrared (IR) analysis of samples was carried out on a Shimadzu Prestige 21 Infrared Spectrometer with a diffuse reflectance attachment (DRIFTS). All samples with reactants were analyzed in the fully dried state, unwashed, with a background of the particular substrate subtracted post-analysis. Spectra were collected for 64 scans, at 4 cm^{-1} resolution, in the range 400-4000 cm^{-1}.

Mass spectrometry analysis was conducted via the LC-MS technique. The experimental procedure and sample preparation follows exactly is stated in section 2.4.3.1. While baseline peak resolution was not achieved for caped-oligoglycine species in the total ion chromatogram (TIC), the extracted ion chromatograms (EIC) for the m/z values corresponding to the indicated species were sufficiently separated. Additionally, the LC technique afforded much cleaner spectra in the peak regions of the EICs.

4.3 Results

4.3.1 *Substrate reactions with glycine*

The poly-condensation of glycine has been observed under identical conditions as those presented in Figure 4-1 for titanium oxides [59]. TiO_2 and ZrO_2 are expected to share some traits as Ti^{+4} and Zr^{+4} are in the same periodic table group and possess the same oxidative state. Seen in Table 4-1, both oxides possess the same range of typical PZC values, so are expected to present comparable magnitudes of charge in solution. For the reaction of glycine and TiO_2 or ZrO_2 at unbuffered conditions (pH~6) the substrate surfaces should present a near neutral or low magnitude net charge, as the PZCs are close to the solution pH. Regardless, positively charged sites will exist in either case and should be capable of electrostatically binding with a glycine zwitterion or anion. According to several reports discussed in section 1.3, this interaction will draw electron density from the carboxylate system, and increase the electrophilicity of the carbonyl carbon therefore facilitating amide formation by nucleophilic attack of an amine. MS analysis of glycine and either oxide shows extensive oligoglycine production. The abundance and maximum length of glycine oligomers here far exceeds products from similar reactions using fumed silica (Figure 3-4a), and to a greater extent, the control reaction (Figure 3-4b), which contains no substrate at all. The ability of ZrO_2 to facilitate a similar extent of oligoglycine production strengthens the proposed mechanism of carboxylate-mediated amide formation by eliminating the possibility that the previously reported results were due more to the Ti component of the oxide. In summary, these results confirm that TiO_2 and ZrO_2 are capable of facilitating direct amide formation, which likely extends to other substrates that are

107

capable of supporting amino acid carboxylates, and therefore do not require an ester aminolysis mechanism.
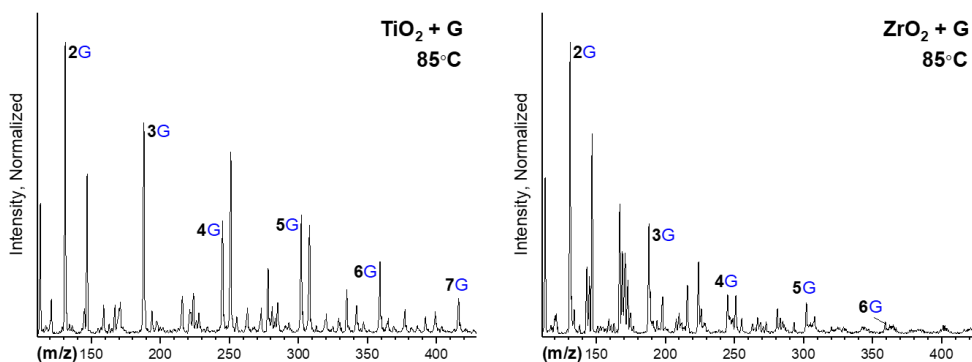
Figure 4-1   MS analysis from the reaction of glycine and TiO₂ or ZrO₂ at 85 °C in unbuffered conditions.

4.3.2   Substrate reactions with MOPA

Similar to the experiments described in CHAPTER 3, MOPA has been applied as a non-oligomerizing and non-cyclizing analog of the α-hydroxy acid LA to assess the ester-forming capabilities of various minerals and substrates. Here, assessment by IR for substrate+MOPA reactions is conducted to determine if ester formation can occur at the surface. MS analysis of those reactions, with glycine added, will provide insight into the mineral characteristics necessary for ester aminolysis.

When fumed silica and MOPA were incubated at 85 °C at unbuffered conditions (pH: ~3), an ester bond was able to form between certain silanol (Si-OH) groups on the silica surface and the carboxyl group for the MOPA. This silyl-ester was directly observed via a hypsochromic shift in the vibrational frequency associated with the carbonyl moiety,

relative to the carbonyl frequency in a carboxylic acid state. Analysis of post-reaction samples from the incubation of MOPA and various metal oxides and silicates by diffuse reflectance infrared spectroscopy (DRIFTS) is displayed below. Within the figure, approximate values associated with a carbonyl in a carboxylic acid and carboxylate state are labeled and marked [116], though the antisymmetric carboxylate stretch can extend to 1650 cm^{-1} [123]. For the carboxylic acid form, only one vibrational mode is apparent, while both the symmetric and antisymmetric carbon-oxygen stretching modes associated with the anionic carboxylate form are visible. Additionally, each plot includes the spectrum of neat, unreacted, liquid MOPA. It is clear from the absence of significant signal in the carboxylate regions that unreacted MOPA is stabilized in its carboxylic acid form. Though not explicitly labels in this figure, the ester carbonyl is close to carboxylic acid frequency, but discernably shifted towards a higher frequency.
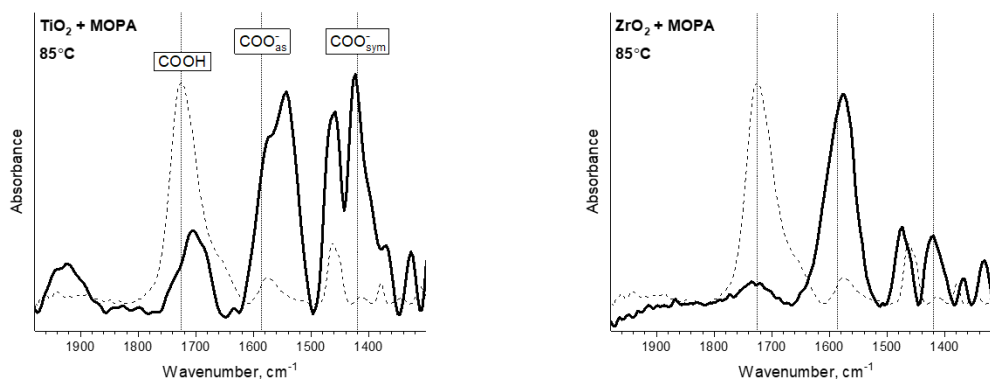
Figure 4-2 **Infrared spectra in the carbonyl region from the reaction of MOPA with TiO$_2$ and ZrO$_2$, incubated at 85 °C.**

In Figure 4-2, both TiO$_2$ and ZrO$_2$ show no sign of ester formation by a shifted carbonyl, 1740-1760 cm^{-1}. These spectra differ from silica reactions and neat MOPA in

that there is a clear signature of carboxylate stabilization. The TiO_2 peaks near 1540 cm^{-1} and 1420cm^{-1} are within an acceptable range of the labels. For the ZrO_2 sample, the peaks near 1575 cm^{-1} and 1420 cm^{-1} are in very close agreement. Both TiO_2 and ZrO_2 have typical PZC values ranging from 5-6, meaning that at the initial reaction pH of ~3, the surface was positively charged, likely due to protonated terminal hydroxyls, e.g. $Ti-OH_2^+$. With abundant positive charges present, electrostatic adsorption is accessible and is likely the responsible for stabilization of MOPA as a carboxylate on both oxides.
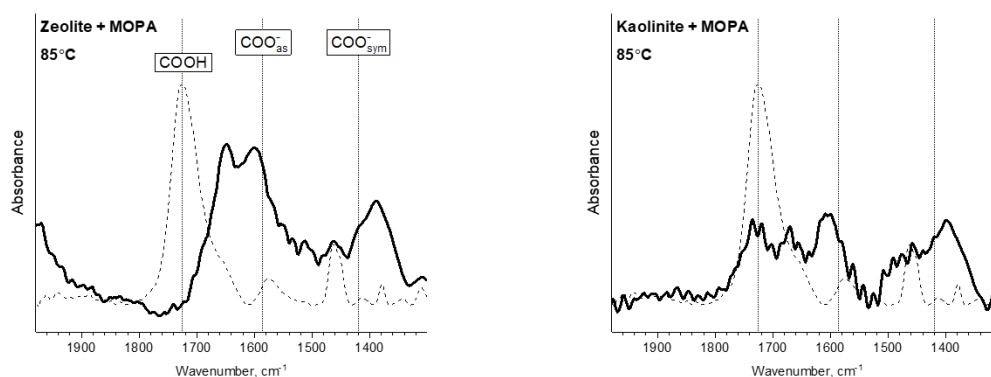
Figure 4-3   Infrared spectra in the carbonyl region from the reaction of MOPA with Zeolite and Kaolinite, incubated at 85 °C.

Two silicates, a zeolite and kaolinite, were also subjected to incubation with MOPA and subsequent IR analysis. For the zeolite sample, evidence of esterification is not present. The carboxylic acid region is also not populated. While there are peaks near both labeled carboxylate regions, the spectrum is distinct from the previous oxide samples. Zeolites are known to have very low PZCs and would be negatively charged. The peaks are not as narrow or well-resolved as for the oxides and this might be due to additional mode of interaction with the mineral, specifically involving the high surface area and channel like

110

architecture associated with tectosilicates such as zeolites. The kaolinite spectrum also does not demonstrate ester formation. Interestingly, this sample appears to have near equal signal in the carboxylic acid and carboxylate regions. While kaolinite also has a PZC below the MOPA solution pH, sheet-like clays such as kaolinite are known to have high isoelectric point motifs on edge sites [50] which would present as a positively charged surface and possibly support a MOPA carboxylate while the negative basal planes permit a protonated MOPA state. In both cases of silicates, MOPA signal is still detectable post-incubation, which is not expected if no interaction occurs, due to the volatility of MOPA itself.
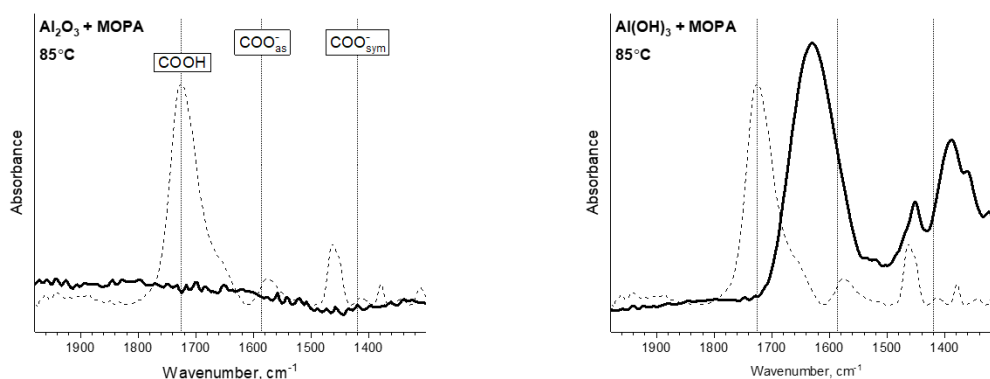
Figure 4-4   Infrared spectra in the carbonyl region from the reaction of MOPA with Al$_2$O$_3$ and Al(OH)$_3$, incubated at 85 °C.

The final set of "MOPA-test" substrates are two distinct Aluminum-Oxygen substrates. While Al$_2$O$_3$ is considered an oxide and Al(OH)$_3$ is classified as a hydroxide, both have PZCs at 9, far above the reaction pH. Accordingly, both these substrates will present positive surface charges, but by different motifs. For titanium, zirconium oxide, along with aluminum hydroxide, surface hydroxyls are present so acidic sites can be either

111

a protonated hydroxyl or an incompletely coordinated metal cation. However, Al_2O_3 is known to possess an uncommonly low population of surface hydroxyls, compared to most metal oxides, and therefore has only the Lewis acidic Al^{3+} cation as an acid site [124]. Now, the primary difference between Al_2O_3 and $Al(OH)_3$ is not the magnitude or polarity of the surface charge, but the presence of protonated hydroxyls as the charged species. Results from MOPA incubation show that the MOPA carboxylate is present on the $Al(OH)_3$ sample, but no MOPA is retained on Al_2O_3. This experiment suggests that not just positively charged oxides are capable of carboxylate stabilization, but any substrate with a surface hydroniums might retain deprotonated MOPA or similar species. This is interesting in the context of direct amide catalysis, which is observed on oxides when amino acid anions are supported.

Continuing a similar experimental trajectory as for the silicas discussed in CHAPTER 3, the reaction of MOPA+G was carried out in the presence of several distinct substrates. Analysis of the products by LC-MS provided an elevated level of sensitivity compared to direct injection techniques, despite incomplete temporal peak resolution. Figure 4-5 and Figure 4-6 display superimposed extracted ion chromatograms for the expected 1MOPA+nG products.
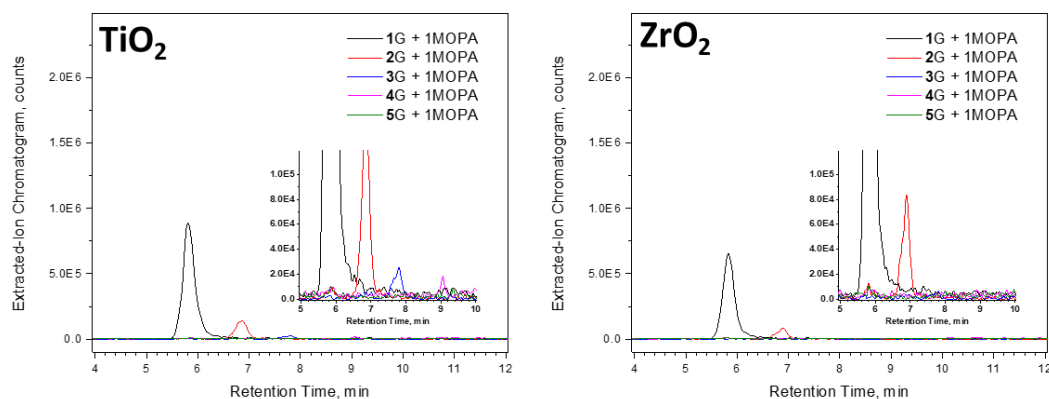
Figure 4-5 **LC-MS analysis from the reaction of glycine+MOPA for TiO₂ or ZrO₂ at 85 °C in unbuffered conditions.**

TiO₂ and ZrO₂ show the longest oligoglycine products, as well as the greatest abundance of those species. While glycine poly-condensation was expected in the presence of these two substrates, considering the extensive oligoglycine products seen in the MOPA-absent reaction (Figure 4-1), the unexpected result here is a lack of longer oligomers. If oligomers exceeding 7 residues in length are produced with glycine alone, why is there such a reduction in product length when MOPA is included? The two main differences between the reactions are i) the initial solution pH is significantly more acidic (pH~3) for G+MOPA and for glycine alone, and ii) a second molecular species might compete for surface sites, which must be accessed for amide formation. The increased acidity should serve to assist the reaction, as protonation of the carbonyl oxygen is a step in the mechanism. However, an increased H^+ concentration will contribute to a less frequent deprotonated amide, which is necessary for the amine to achieve sufficient nucleophilicity for amide formation. Additionally, a lower pH will mean a significantly greater population of positively charged, hydronium surface terminations. While these have been implicated

as the main carboxylate interacting motif, regarding the nucleophilicity of the amine, if Lewis base sites were necessary to deprotonate the amine of the zwitterionic glycine, a lower pH might make that less common. The second difference regards competition; it may be the case that less oligoglycine was able to form due to many of the surface site being occupied by MOPA molecules. Considering the difference in pK_a for glycine and MOPA and a solution pH below the MOPA pK_a, glycine would have a greater population of charged carboxyl groups, and therefore binding sites. However, it is unclear if this contributes to the observed disparity in oligoglycine lengths.
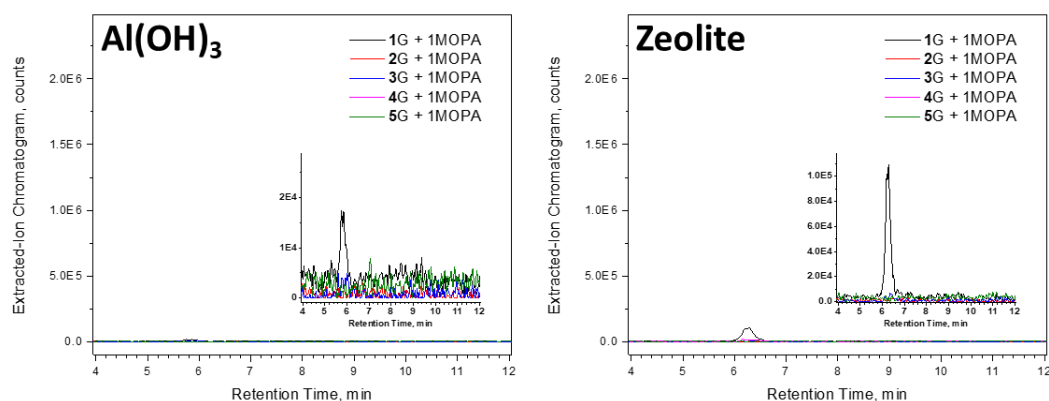
Figure 4-6   LC-MS analysis from the reaction of glycine+MOPA for Al(OH)₃ or Zeolite at 85 °C in unbuffered conditions.

The MOPA+G reaction with Al(OH)₃ and zeolite both produce only the MOPA–G heterodimer. For silica, this reaction was able to proceed via aminolysis by glycine of silyl-esters formed between the substrate and MOPA. Though neither of these substrates demonstrated ester formation when incubated with MOPA, the MOPA carboxylate form was observed. Considering the TiO_2 and ZrO_2 MOPA and G+MOPA results, which showed MOPA carboxylate and oligoglycine formation, it might be expected for Al(OH)₃

114

to produce more and longer G oligomers. However, this is not the case, and Al(OH)$_3$ performs just as well as zeolite.

4.3.3 Substrate reactions with NAG

Model reactants that serve as molecular analogs for the components of depsipeptide reactions have a rapid test molecule when analysed by IR. NAG has been utilized as a non-oligomerizing and non-cyclizing analog of a non-monomeric amino acid to assess the ester-forming capabilities of various minerals and substrates. Here, the substrate+NAG reaction scheme has been administered to 10 distinct samples that are mostly considered prebiotically plausible. Post-incubation analysis by DRIFTS will focus on two key regions: the hydroxyl stretch, to determine of isolated hydroxyl species are present and the carbonyl stretch, to determine if NAG can esterify with the surface.

Extensive hydrogen or cation bonding terminal hydroxyls experience a diverse energetic landscape, so are therefore capable of adsorbing a wide range of infrared radiation. This transforms the otherwise narrow absorption peak, seen with isolated hydroxyls, into a broad absorption band. From the results of esterification between fumed silica and quartz in CHAPTER 3 and other sources [79], such isolated moieties are necessary for EAX support. So narrow hydroxyl peak(s) are likely correlated with a substrate well-suited for NAG esterification. The esterification with NAG will be assessed in a similar manner as was done for silica – a hypsochromic shift of ~20 cm^{-1} [115-117].

The hydroxyl (-OH) stretching region for substrates in an unreacted state is shown in Figure 4-7. Though no NAG has been applied, these sample have been subjected to water and similar incubation temperatures and durations to facilitate the most accurate

background spectra possible. Spectra for fumed silica and quartz, adapted from Figure 3-18, are included as reference. Fumed silica has a sharp peak at 3745 cm^{-1} that is associated with isolated silanol groups. This is in stark contrast to the broad absorption feature centered at 3655 cm^{-1} that is most prominent for the quartz sample and is associated with silanol groups in various hydrogen-bonding motifs. The two olivine group nesosilicates, Forsterite and Fayalite, along with the inosilicate Enstatite, all display hydrogen-bound surface hydroxyls and no isolated species. The zeolite displays an incredibly broad feature in this region, with no peak resolution near the quartz-like 3655 cm^{-1} frequency. This lower frequency absorption may be indicative of retained water due to its high surface area and porous structure. The phyllosilicate Kaolinite, known to be hydroxyl terminated [125], presents several narrow absorption peaks that are interpreted to be hydroxyls that are not part of a hydrogen-bonding network. A narrow peak and does not necessitate availability for reaction or adsorption, but demonstrates a low diversity of hydroxyl conformations, and therefore excitable vibrational modes. Notwithstanding, this result maintains the possibility of NAG esterification, considering the determination from fumed silica and quartz that silanols must be isolated to participate in EAX. A second phyllosilicate, Ca-Montmorillonite, has an absorption spectrum similar to quartz. Inability for Montmorillonite to esterify with NAG would align with results from quartz+NAG. Albite, a tectosilicate, presents a more featured spectrum with some discernable yet poorly resolved peaks. However, these are firmly in the region associated with water and bound hydroxyls. Dickite displays features with many similarities Kaolinite, a phyllosilicate in the same sub-group. At last, while vanadium oxide is the only non-prebiotic mineral

included here, it likely has the lowest PZC value. However, it is clear that V_2O_5 is not

hydroxyl terminated, consistent with previous observations [126, 127]
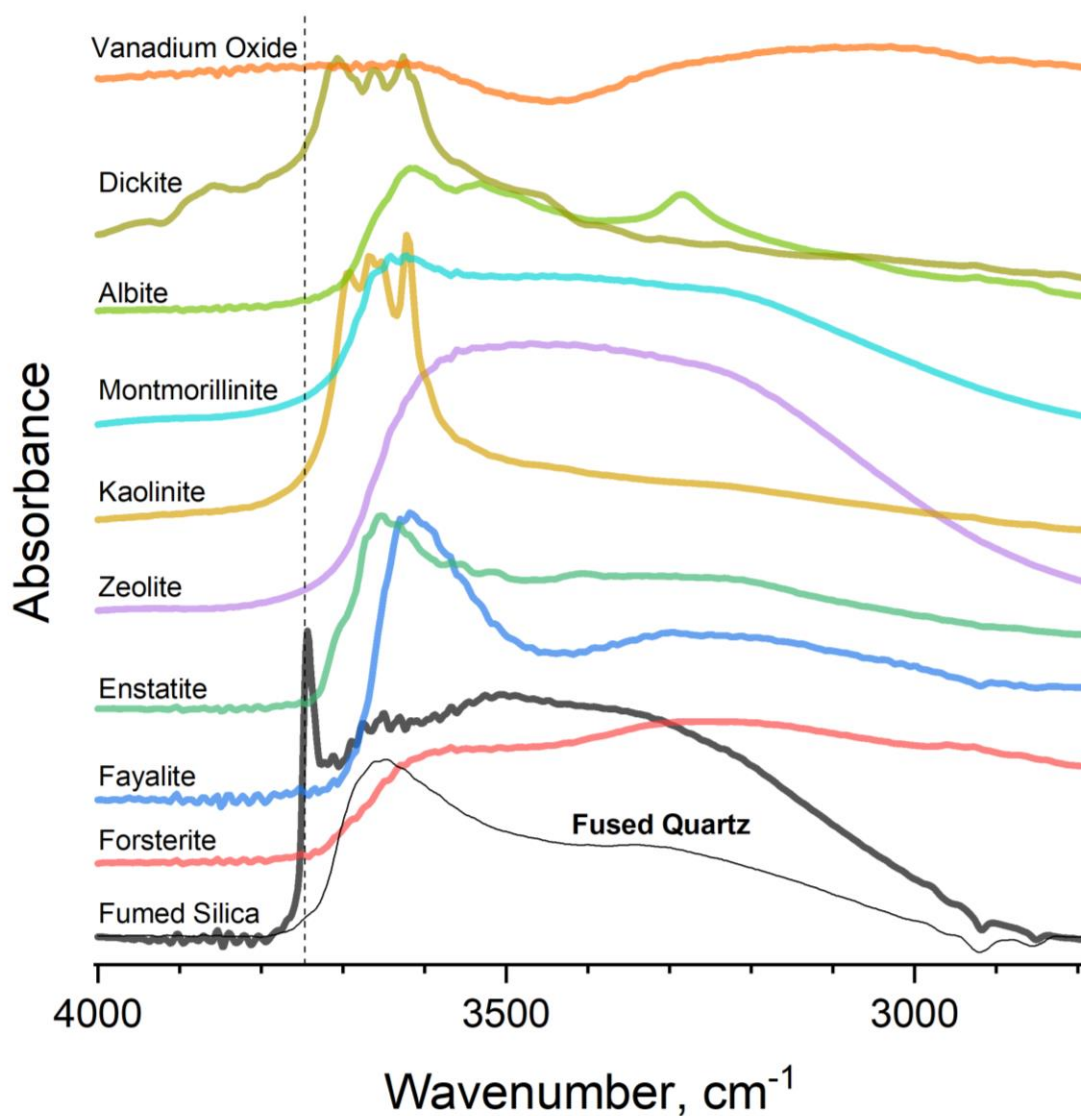
Figure 4-7   DRIFTS analysis of all substrates listed in Table 4-1 highlighting the hydroxyl stretching region. This region includes the characteristic vibrational frequency for the silanol terminations found on silica.

The results from IR analysis of mineral pwders after reaction with NAG at 85 °C are divided into two figures. Tectosilicates and phyllosilicates are displayed in Figure 4-8. The post-reaction spectrum for fumed silica is included as an example of signal from a hyspochromic shifted carbonyl. For additional reference, the virational frequency for unreacted NAG is marked, along with the entire spectrum. Kaolinite and Dickite show a carbonyl vibrational frequency exactly overlapping unreacted NAG, infering both the lack of esterification and that NAG is present in the carboxylic acid form and not the carboxylate. This is consitant with the PZC values for these minerals, which are either at or slightly below the solution pH, meaning that a positive surface is absent, though kaolinite has been impliacted in an ester-forming reaction [128].

The kaolinite interstitial region, which is likely host to the hydroxyl groups responsible for the narrow peaks seen on the IR spectrum, may be either inaccessible or too confining for the necessary transition state. Additionally, if kaolinite is in a depsipeptide forming reaction and relies on surface-EAX, the initial products may be retained or experience insufficient mobility for indefinitely repeated re-esterification at the C-terminus of an increasingly growing oligomer chain. Albite data is anomolous; the spectral signatures for a NAG carboxylate symmetric and antisymmetric stretches are present near 1550 cm^{-1} and 1420 cm^{-1}, but literature values for the PZC are low, ~2, such that the positive surface which would support an anionic NAG would not be present. Still, esterification is not observed on Albite.

For Montmorillonite and Zeolite, there are detectable shifts in carbonyl vibrational frequency. Zeolite is 9 cm^{-1} shifted, while Montmorillonite is 16 cm^{-1} shifted. While the Zeolite shift is much smaller than observed for silica, the Montmorillonite shift is much

closer. Examination of the hydroxyl region for sample reacted with NAG may show a negative signal if certain hydroxyl motifs are consumed. For zeolite, the only depleted feature is the broad absorption below 3750 cm^{-1} which may be mostly due to water evaporation. There is a more localized negative signal for Montmorillonite at 3640 cm^{-1}. A peak here is likely not the same type of isolated silanol as observed for fumed silica, but consumption of some surface species does support the observed hypsochromic shift in the carbonyl region as evidence of esterification.
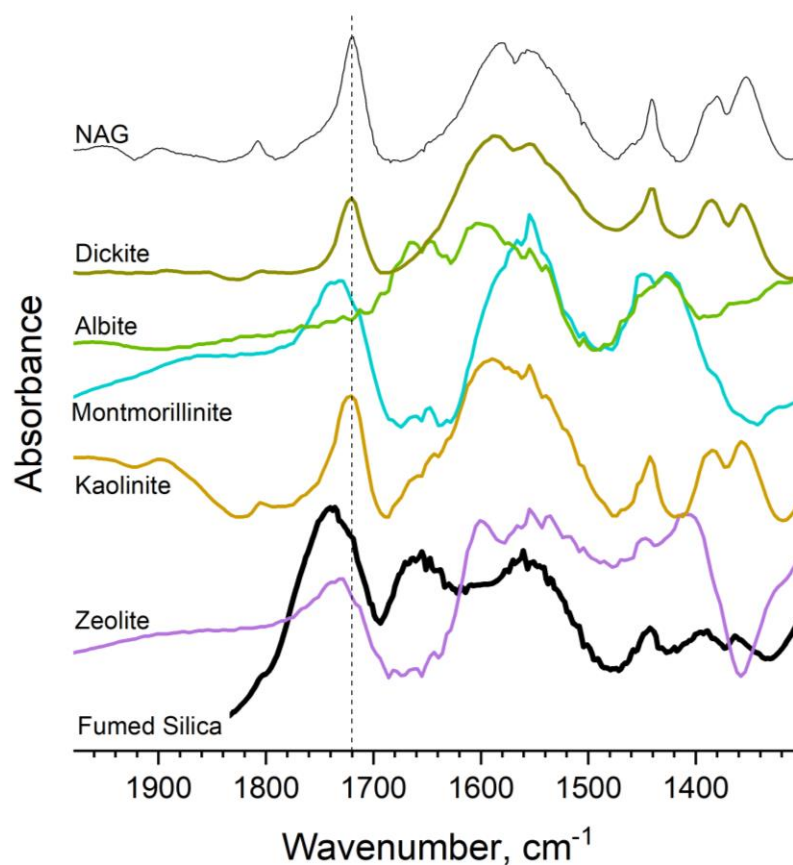
Figure 4-8   DRIFTS analysis of the carbonyl region for the labeled substrates after incubation with NAG. Included here are tectosilicates and phyllosilicates.

The results from IR analysis of mineral powders after reaction with NAG at 85 °C for mafic silicate minerals and vanadium oxide are displayed in Figure 4 9. The three silicates, Forsterite, Fayalite and Enstatite all display NAG in the carboxylate form and no indication that ester production has occurred. This is expected, as the surfaces would be positively charged due to PZC values exceeding the solution pH. The vanadium oxide show NAG in its native carboxylic acid form, and not esterified. This substrate, while not a plausibly prebiotic mineral that would appear in any significant abundance, is a metal oxide with a very low PZC. This contrasts well with TiO_2 and ZrO_2 which have nearly similar cationic oxidation states, yet much higher PZC values. V_2O_5 does not have a surface decorated with hydroxyl groups, in further contrast to TiO_2 and ZrO_2, so the adsorption state of NAG can only be discussed in terms of PZC. The stabilization the NAG carboxylic acid on vanadium oxide suggests that negatively charged surfaces can maintain such moieties in a protonated state.
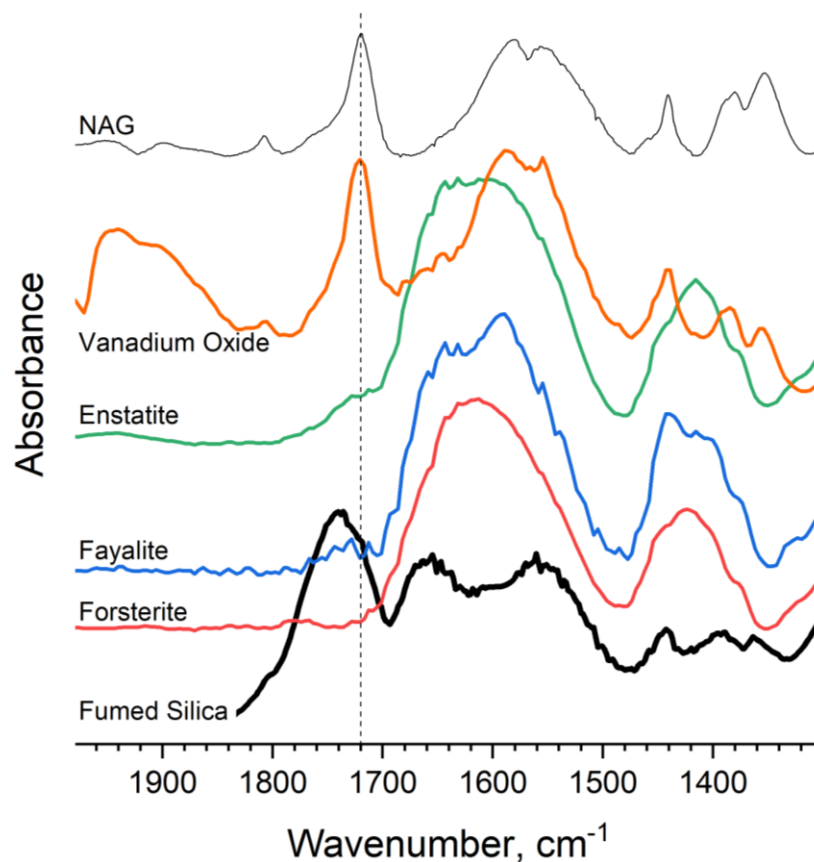
Figure 4-9   DRIFTS analysis of the carbonyl region for the labeled substrates after incubation with NAG. Included here are other silicates and oxides.

A continuation of the oligoglycine experiment in section 3.5, the reaction of NAG+G was carried out in the presence of several distinct substrates. Analysis of the products by LC-MS provided an elevated level of sensitivity compared to direct injection techniques, despite incomplete temporal peak resolution. Figure 4-10 displays superimposed extracted ion chromatograms for the expected 1MOPA+nG products.
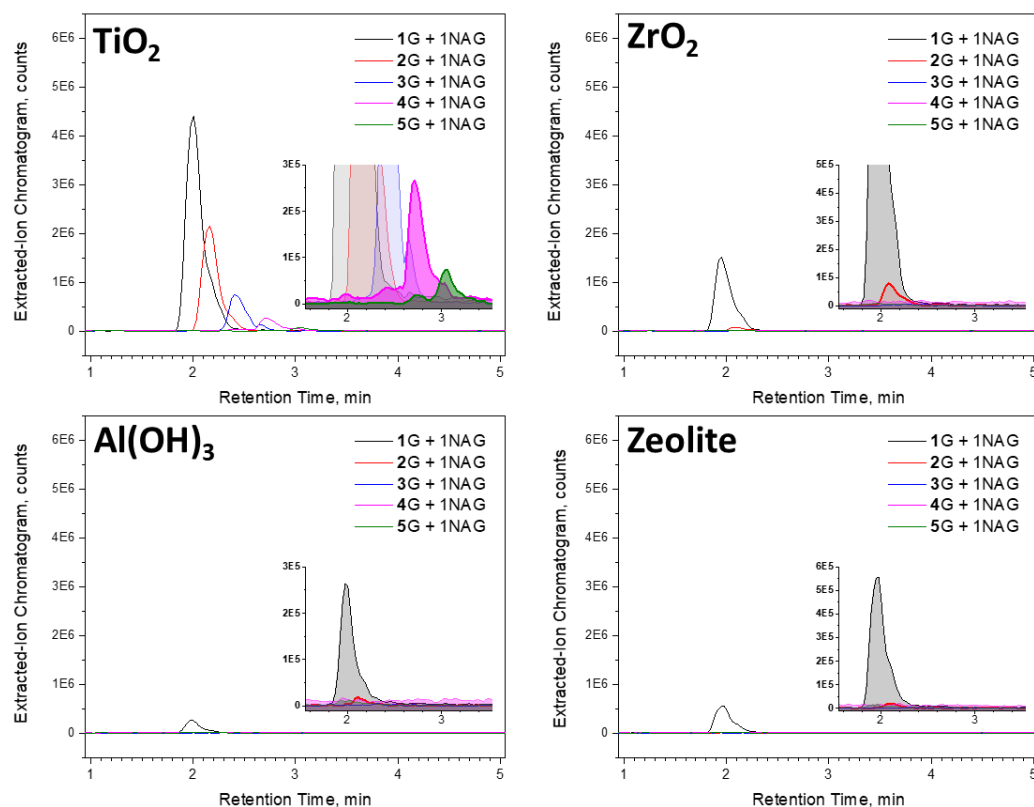
Figure 4-10   LC-MS analysis from the reaction of glycine+NAG for TiO$_2$, ZrO$_2$, Al(OH)$_3$ and zeolite at 85 °C in unbuffered conditions.

The TiO$_2$ produces the longest glycine oligomers, as it has in most cases discussed in this chapter. Due to the results demonstrating G poly-condensation with TiO$_2$ alone, it is unlikely that EAX was a mechanism used in any way. The remaining substrates all produced mainly the NAG–1G heterodimer, with only ZrO$_2$ presenting minimal signal for the di-glycine species. These results are similar in extent of reaction and relative reaction yield to the MOPA+G experiments.

4.4   Conclusions

The same model reactions with depsipeptide component analogs that have been studied with SiO_2 were applied to other inorganic substrates, including metal oxides and various silicates. The intention of these reactions were to determine of surface esterification could occur, and if so, what characteristics of the substrate were responsible for such an interaction. Ultimately, esterification is the first step in the broader ester aminolysis mechanism for poly-condensation of amino acids in a depsipeptide system.

It was determined that at mild temperatures, substrates which supported carboxylates where categorically unable to esterify with either test molecule, MOPA or NAG. The parameter which predicted this behavior was a PZC above the solution pH. Consequently, protonated, and therefore positively charged, surface hydronium groups are unable to esterify with test molecules, likely due to the decreased nucleophilicity of the terminal hydroxyl.

The hypothesis of isolated surface hydroxyls being necessary for esterification was also tested. For silica, the extensively hydrogen-bonding silanols were identified via IR analysis, such that the absence of a narrow isolated hydroxyl peak was associated with the inability to esterify and facilitate EAX. However, results from the NAG-test showed that the only two substrates that exhibited the hypsochromic shift characteristic of ester formation, zeolite and Montmorillonite, did not also have a sharp absorption in the hydroxyl region. In fact, several clays Kaolinite and Dickite, which did have narrow hydroxyl absorptions, did not demonstrate esterification abilities. While Montmorillonite and quartz silanol regions look almost identical, they are in fact quite distinct, owing

mainly to the sheet-like layer structure present in the Montmorillonite clay. From these results, it is clear that a simple DRIFTS analysis is insufficient to predict the ability of a mineral to facilitate EAX in a depsipeptide system. It may be the case that additional spectroscopic techniques must be added to the analysis regiment in order to predict the reactivity of not just the chemical moieties in isolation, but the entire mineral structure as a whole.

CHAPTER 5.   LOW ENERGY SECONDARY ELECTRON INDUCED DAMAGE OF NUCLEOTIDES[3]

5.1   Summary

Radiation damage and stimulated desorption of the ribo- and deoxyribo-nucleotides dAMP, rAMP, dCMP and rCMP have been measured using x-rays as both the probe and source of low energy secondary electrons. The fluence dependent behavior of the O-1s, C-1s, and N-1s photoelectron transitions were analyzed to obtain phosphate, sugar and nucleobase damage cross sections. Growth of the integrated peak area for the O-1s component at 531.3 eV, corresponding to cleavage of the C-O-P phosphodiester bond, yielded effective damage cross sections of about 23 Mb and 32 Mb ($1 \text{ Mb} = 10^{-18} \text{ cm}^2$) for AMP and CMP molecules, respectively. The cross sections for sugar damage, as determined from the decay of the C-1s component at 286.4 eV, and the glycosidic carbon at 289.0 eV were slightly lower (about 20 Mb) and statistically similar for the r- and d-forms of the nucleotides. Though there is no statistical difference between the sugar forms, changing the nucleobase from adenine to cytidine has a slight effect on the damage cross section, possibly due to differing electron capture and transfer probabilities. Though x-ray induced reactions in nucleotides involve both direct ionization and excitation, the observed bonding changes were likely dominated by the inelastic energy-loss channels associated with secondary electron capture and transient negative ion decay.

---

[3] This chapter was adapted from previously published work and is reproduced with permission. McKee, Aaron D.; Schaible, Micah J.; Rosenberg, Richard A.; Kundu, Sramana; Orlando, Thomas M. "Low energy secondary electron induced damage of condensed nucleotides" J. Chem. Phys. 150, 204709 (2019)

5.2 Background

5.2.1 Context

The ubiquity of deoxyribose in DNA and ribose in RNA has been the subject of investigations seeking to understand the origins of RNA and life in general [129, 130]. Sugar selection may be influenced its ability to spontaneously form glycosides with canonical or non-canonical nucleobases, and ultimately self-assemble into proto-RNA structures [131]. Due to the unambiguous presence of prebiotic building blocks on extraterrestrial bodies and the early Earth elevated UV flux, chemical reactions due to high energy radiation [132] must be addressed. Even more so, the inelastic dissipation process for high energy radiation, including protons, ions, UV photons and electrons, through a molecular film or incident a mineral substrate, all produce a significantly larger population of lower energy radiation. These are typically photons and electrons which undergo subsequent inelastic process to ultimately produce near-thermalized, low energy radiation [133]. It could be the case that sugar identities in proto-RNA systems or the transition from ribose to deoxyribose was influenced by low energy electron radiation.

Since the original work of Sanche and co-workers [134], there has been significant activity in understanding the elastic and inelastic scattering of low energy electrons (LEEs) with gas and condensed phase biomolecule targets such as sugars [135, 136], nucleotides [137, 138], deoxyribonucleic acid (DNA) [134, 139-143] and DNA complexed with amino acids [144, 145]. LEEs loose energy prior to trapping via the formation and decay of transient negative ion (TNI) resonances that are typically classified as either lower energy single-particle shape resonances or one-hole and two-electron core-excited Feshbach

resonances, at slightly higher energies. Recent studies on LEE interactions with isolated gas-phase RNA and DNA constituents and small clusters of biomolecules with hydration water(s) have used mass spectrometry to detect the stable anionic fragments produced primarily via the decay of core-excited Feshbach resonances via dissociative electron attachment (DEA) [146-148]. Condensed-phase work has also probed the potential importance of TNIs and DEA using post-irradiation analysis techniques such as gel-electrophoresis [134, 139, 149] and, more recently, enzymatic digestion techniques [150, 151]. Much of the previous work on condensed phase DNA targets is summarized in several review articles [140-142, 152].

5.2.2   *DNA Damage*

It is now generally accepted that initial DNA damage can involve electron capture by the nucleobase followed by transfer to the sugar phosphate bond [153], or direct capture by the phosphate species for very low electron energies (<0.5 eV) [137, 148]. Transfer of the electron initially captured by the nucleobase can be facilitated by the reduction in the energy barrier brought about by the dynamic fluctuations of the adjacent water molecules [154]. The nature of these initial capture resonances can also change due to electronic coupling, giving rise to compound resonances, water damage products and very slow electrons which can locally interact, yielding closely spaced double strand breaks [149]. This proposed model for double strand breaks was recently re-introduced to explain clustered damage at energies below 10 eV [150]. Recent work also implies that the presence of water can lead to a proton transfer event that can also lead to bond breakage that may be different than the primary pathway for DEA [148]. In such experiments, autoionization also occurs but is not probed directly.

An impinging x-ray beam interacts with surfaces to eject both photoelectrons (electrons which do not inelastically interact with any matter until they reach vacuum) and backscattered secondary electrons (the myriad and sequentially lower energy electrons from inelastic collisions). Considering both these processes, x-ray radiation can be used to simultaneously produce and probe changes in the bonding structure of deposited biomolecules [155]. The ejected photoelectrons are diagnostic of the surface composition and can be used to probe the chemical state of the parent atoms through x-ray photoelectron spectroscopy (XPS). Because XPS measures the abundance and kinetic energy of photoelectrons which escape from the surface without scattering, the sampling is highly sensitive to only the uppermost ~10 nm of material. Energetic photoelectrons also ionize atoms and molecules of the solid and produce abundant secondary electrons with energy distributions typically peaking at less than 5 eV [156]. These LEEs can be captured into various resonance states of DNA and its constituents and cause damage to the chemical bonding configuration as well as stimulated desorption of molecules and fragments from surfaces.

Previous work has characterized nucleobases deposited under vacuum conditions and DNA-coated substrates prepared in atmosphere using XPS analysis [157]. These results show that x-ray radiation produces a reduction in the DNA-specific signals, e.g. the N-1s and P-2p transitions, as well as in the O-1s signal, while there is a slight increase in total C-1s signal over the course of the experiment. It was shown that the signal associated with phosphate group oxygen atoms was constant, while those ascribed to alcohol and carbonyl regions decreased. This is consistent with strong interactions between the silicon substrate and the phosphate groups. An increase in the intensity of the C-1s peak

components assigned to the various alcohol (C-OH), ether (C-O-C), or imino bonds was observed after x-ray exposure, and these changes were tentatively ascribed to the formation of hydroxymethyl uracil. It was also seen that intensity of the signal ascribed to the amino bonds decreased rapidly with x-ray exposure, indicating the loss of hydrogen and/or cleavage of the glycocidic bond between the nucleobase and the sugar.

Significant improvements in XPS measurements can be realized using synchrotron radiation, which provides orders of magnitude greater luminosity than standard laboratory x-ray sources. Synchrotron beams provide large enough x-ray fluxes such that appreciable secondary electron fluences ($>10^{17}$ e$^-$/cm^2) can be achieved in a short timeframe and molecular damage can be imaged in real-time by monitoring the changes in the relative intensities of the XPS photoelectrons. Previous experiments carried out using synchrotron radiation have shown the utility of XPS to probe the bonding interaction and geometry of DNA adsorbed on Au substrates [158]. Specifically, angle and polarization resolved XPS studies indicated that both thiolated and unthiolated DNA samples adsorbed on Au were oriented 45º from the surface normal. By monitoring the decay of the O-1s photoelectron peak during irradiation with 950 eV photons, Rosenberg et al. [158] also showed that phosphoester (C-O-P) bonds were cleaved and hydroxyl (C-OH) fragments desorbed while the abundance of carbonyl bonds (C=O) and phosphate bound oxygen (P=O or P-OH) present on the surface increased a proportionately larger amount. The damage cross section for thiolated DNA was found to be significantly higher than for the unthiolated DNA. This was correlated with the lowest unoccupied molecular orbital of the thiolated DNA initially being less populated and hence more effective in capturing low energy secondary electrons from the underlying Au substrate. The x-ray induced damage of the DNA did not produce

significant changes in the total nitrogen abundance or the relative amounts of amine and imine components in the N-1s signal as had been seen in previous studies [157, 159].

Though the important roles of secondary electrons, surface bonding geometries and surface states have been demonstrated, how the nature of the excited states, the variance in the molecular constituents, and the many body interactions contribute to damage in condensed nucleotides remains unclear. In this current work, we explore the mechanisms of LEE induced damage of 2'-deoxyadenosine 5'-monophosphate (dAMP), adenosine 5'-monophosphate (rAMP), 2'-deoxycytidine 5'-monophosphate (dCMP) and cytidine 5'-monophosphate (rCMP) thin-films on a 200 nm thick Au film using tunable synchrotron x-ray irradiation. Here, damage is defined as any molecular transformation involving the breaking and formation of new bonds, as well as desorption of material from the sample surface. Specifically, it is shown that TNI's produced by photoelectron scattering within the nucleotide films decay through dissociative electron attachment or autodetachment and lead to damage and fragment desorption. The electrons released via autodetachment can also produce additional low energy shape resonances that are localized on the sugar and phosphate groups and lead to dissociation. Thus, low energy shape resonances likely contribute significantly to the overall damage to the nucleotides. Although water is present in these samples, its role in the damage events cannot be precisely determined under our experimental conditions.

5.3   Experimental

5.3.1   Preparation of Samples

The chemical structures of the rAMP, dAMP, rCMP and dCMP nucleotides are shown in Figure 5-1 where the atom positions corresponding to specific XPS component designations are indicated. All samples were prepared by first dissolving pure (99.9%) nucleotide crystal analyte in a 50:50 mixture of high purity (> 99.9%) water and methanol to create a 50 µM solution. Solutions were then sonicated for approximately 10 min to assure solvation of the analyte crystallites at room temperature. A 300 µL volume was then deposited via drop-casting onto a washed, 200 nm thick Au film that has been vapor deposited onto a doped Si substrate (5 mm x 10 mm). The samples were dried at ambient pressure and room temperature for at least 24 hours before analysis.
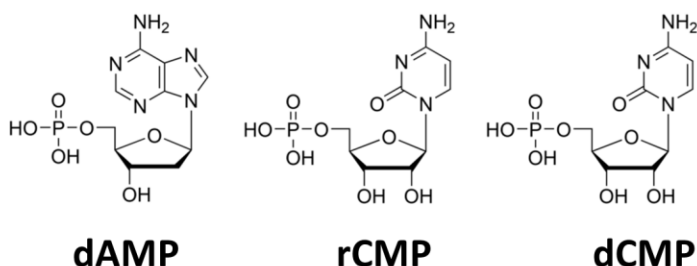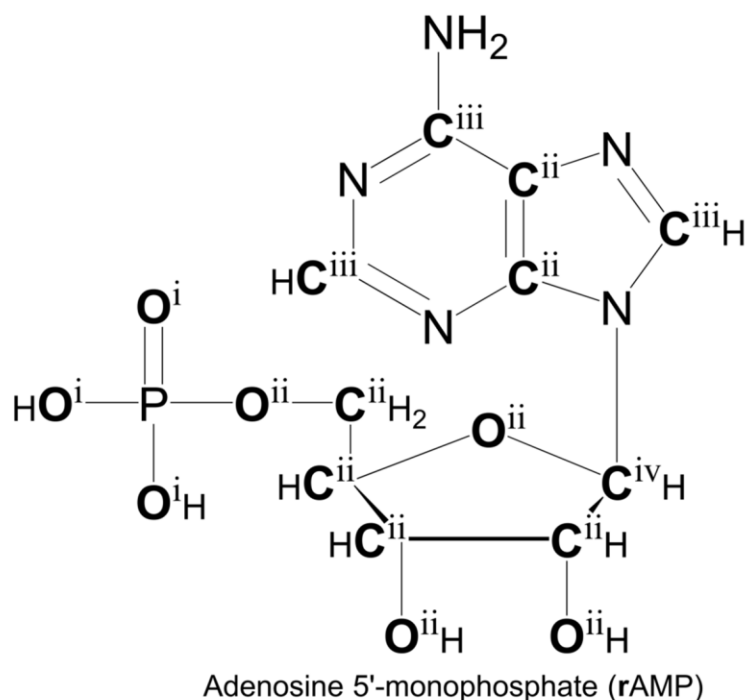
Figure 5-1 **Chemical structures for all analytes included in this study. The ribo-(r) and deoxyribo- (d) nucleotides differ only in the presence or absence of an alcohol at the 2' position of the sugar unit. RNA is comprised exclusively of ribonucleotides, while DNA is exclusively deoxyribo-nucleotides. AMP and CMP differ by the identity of the nucleobase, the purine adenine and the pyrimidine cytosine.**

To characterize the distribution and thickness of the deposited analyte films and determine the physical state of the irradiated samples, scanning electron microscopy (SEM), energy dispersive x-ray spectroscopy (EDX), and x-ray photoelectron spectroscopy (XPS) analyses were performed at Georgia Institute of Technology. Samples were first imaged on a Hitachi SU-8230 FE-SEM (Hitachi High Technologies Corporation,

Tokyo, Japan) using various combinations of magnification and beam current settings selected to obtain the highest fidelity image. Additionally, EDX spectra were collected by combining the SEM column with an Oxford Instruments X-Max SDD 80 mm^2 EDX detector (Oxford Instruments Nano-analysis, High Wycombe, UK). The EDX images are used to directly identify regions containing elevated amounts of O, C, N, and P on the Au substrate. The SEM, EDX, and XPS analysis of the samples held in the laboratory atmosphere environment over a 2-week time-period do not show significant differences in the deposited film morphology or surface composition.

Previous attempts at sample preparations that resulted in visible patches of deposited analyte were found to be inadequate. If the analytes is an insulating material, as is the case here, a think film will be unable to conduct electrons from ground to replace the photoelectrons ejected due to the x-ray beam. This phenomena is known in photoelectron spectroscopy as surface charging, and results in a gradual and systemic increase in the apparent binding energy of electrons.
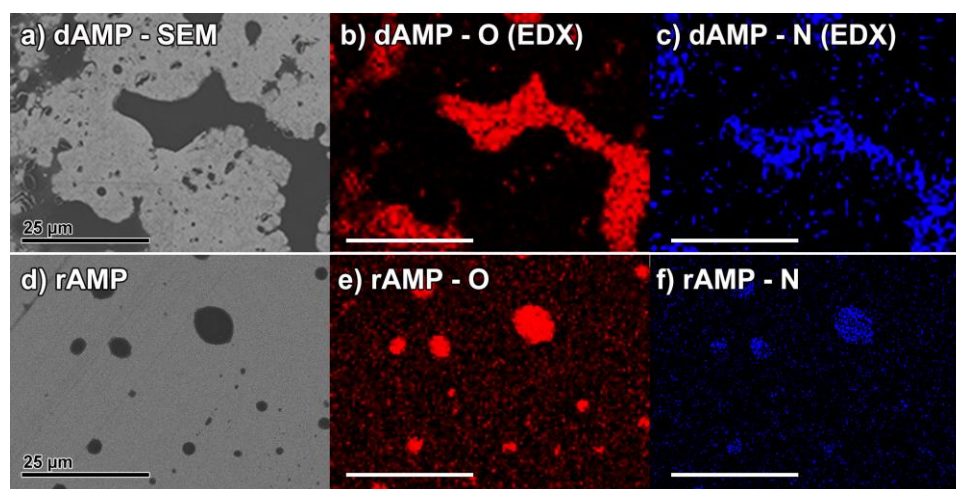
Figure 5-2   AMP samples deposited on gold, before irradiation, analyzed by SEM (a, d) and EDX (b, c, e, f). From the SEM, a difference in deposition morphology

between the d- and r- forms is notable. The EDX spectra feature elements that are associated with the analyte, but not expected to abundantly appear in adventitious species, thereby confirming the deposition of the nucleotides.

SEM and EDX images of the dAMP and rAMP films deposited on bare Au are shown in Figure 5-2. The SEM images for rAMP and dAMP (a and d, respectively) were taken in the high-angle backscattered electron mode where the light/dark contrast (or Z-contrast, shown more explicitly in Figure 5-3) differentiates between areas of high and low effective atomic number [160]. For the nucleotide analyte deposited on the Au substrate, the areas of low atomic number correspond to the deposited analyte and appear darker. The rAMP and dAMP EDX maps for the O and N transitions corresponding to the SEM panels are shown in Figure 5-2b-c and Figure 5-2e-f, respectively. The SEM / EDX analysis of the analyte films showed significant spatial inhomogeneities corresponding to 'islands' which contain elevated concentrations of analyte surrounded by presumably bare or sparsely covered Au substrate.

5.3.2   Quantification of Analyte Coverage

5.3.2.1   Scanning electron microscopy analysis

Performing a high Z-contrast analysis allows the surface coverage of 'islands' to be determined (Figure 5-3). SEM images where altered with image processing capabilities in OriginPro. The contrast was gradually increased such that all pixels have adopted either a black or white value. The black regions were interpreted as analyte and the average coverages found for several freshly prepared samples are given in Table 5-1. This technique is convenient, but is ultimately an approximation. Areas that are covered by only a thin layer of analyte, while perfectly visible to the XPS, would be overlooked by this high

contrast technique. The discrepancy between this technique and a much more accurate method for determination of coverage will be discussed below. Additional atomic force microscopy analysis [161] shows that while the thickness of the high concentration regions can vary, the nucleotide regions which show sufficient contrast to be included in the SEM / EDX analysis are at least 50 nm above the Au surface. This is much greater than the XPS sensitivity depth and the expected mean free path of low energy electrons moving through the nucleotide films [162-165]. Therefore, it is expected that most of the electrons causing damage in the XPS sensitive region originate from within the nucleotide films.
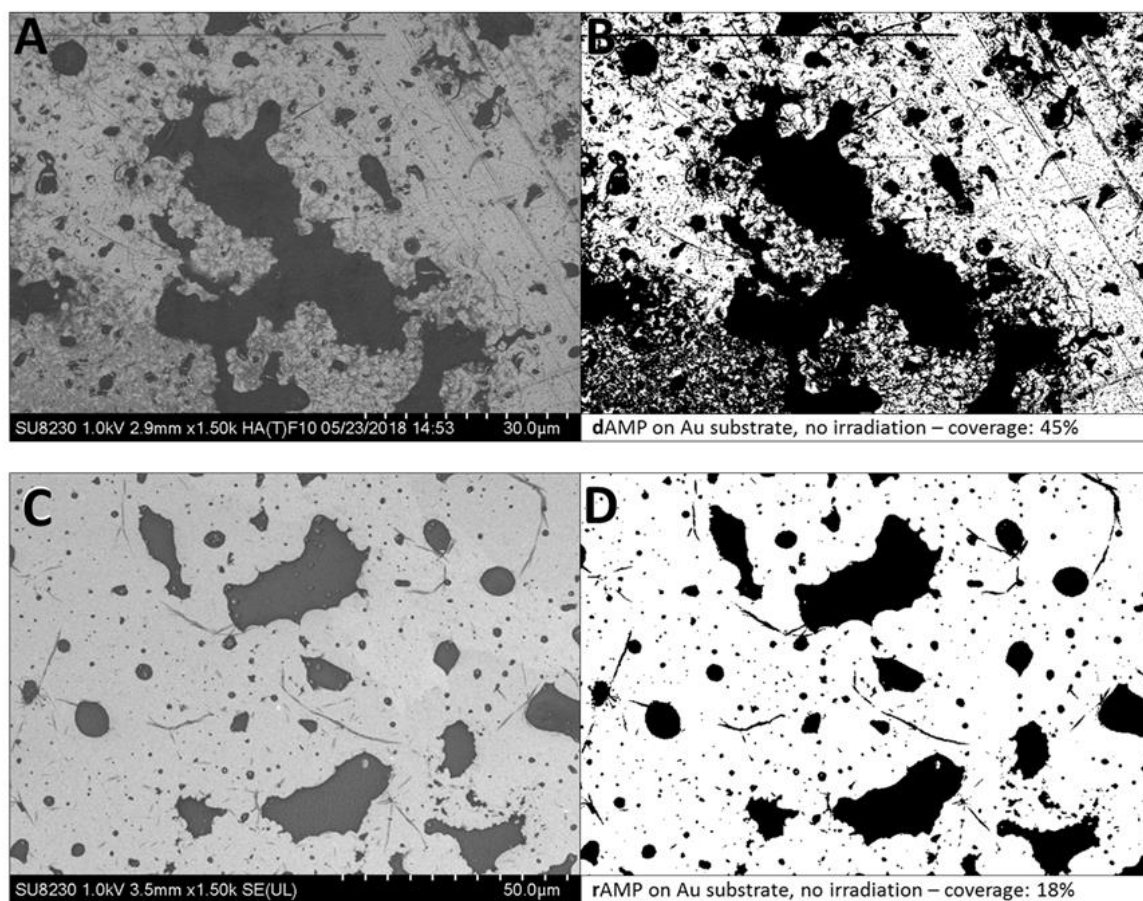
Figure 5-3 **Examples of unadjusted (A and C) and high contrast adjusted (B and D) SEM images of dAMP and rAMP.**

135

Table 5-1   Analyte coverage was determined by analysis of SEM images that have been parsed into a binary covered or not-covered state. A collection of several images from samples of rAMP and dAMP were used to calculate average coverages listed below. This method yields coverage values that are significantly less than those derived from analysis of pre and post-irradiation Au XPS signal, reported as the average ± the standard deviation (Mb).

Molecule	Coverage, %			*Minimum*	*Maximum*
dAMP	46.4	±	12.1	31.7	66.4
rAMP	24.8	±	5.5	18.4	33.1

5.3.2.2 <u>Au-4f$_{7/2}$ Analysis</u>

During the data collection process, signal from the Au 4f$_{7/2}$ transition was recorded before and after each elemental series. A representative spectral pair is provided in Figure 5-4. The source of signal for these peaks is the remaining bare gold substrate. As the sample position is exposed to the x-ray beam for a prolonged duration, fragments and other adsorbed species desorb from the surface, uncovering more substrate and further contributing to the signal. This is the reason that all post-irradiation spectra have a larger integrated area, compared to the initial spectrum. When the integrated areas of these spectra are compared to a position that is known to have no analyte deposited and taken at identical beam and collection conditions, a calibration factor can be determined and coverage calculated.
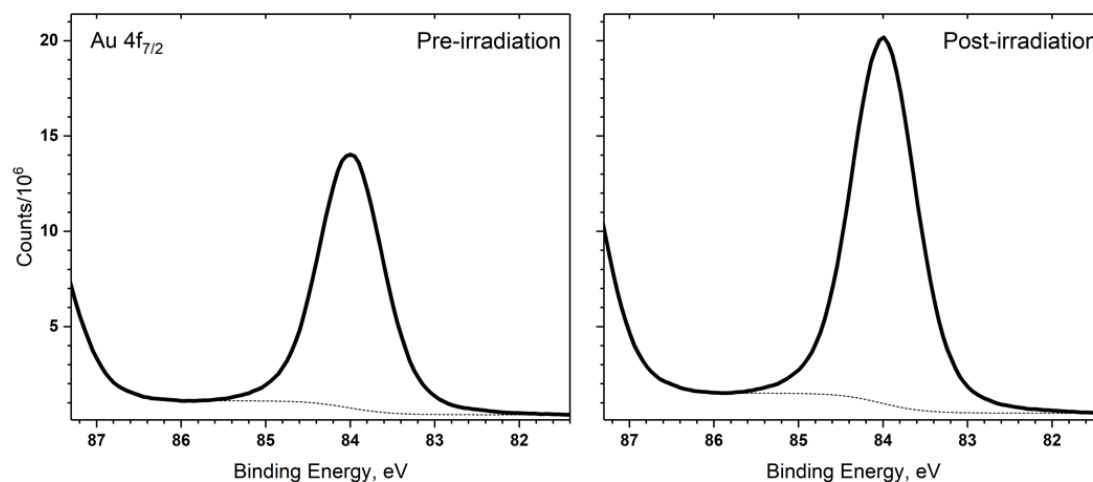
Figure 5-4   **Before and after spectrum of the Au-4f$_{7/2}$ transition. The total area of the Au photoelectron peak increases significantly as a result of analyte desorption from x-ray irradiation.**

The values for coverage by the Au method are summarized in Table 5-2 and are consistently higher. This is expected, due to the lack of any binary determination of coverage. Here, even monolayer analyte coverage diminishes the signal in a quantifiable way. Accordingly, the coverage values by this method are much more reliable and used in quantum efficiency calculations.

Table 5-2   **Analyte coverage analysis by Au-4f7/2 peak integration for all nucleotides, reported as the average ± the standard deviation (Mb). This method is considered to yield more reliable coverage estimates that the aforementioned SEM-derived values.**

Molecule	Coverage, %					
	Pre-Irradiation			Post-Irradiation		
dAMP	62.2	±	4.8	53.7	±	2.0
rAMP	62.1	±	2.6	48.6	±	2.3
dCMP	69.5	±	4.3	51.9	±	2.9
rCMP	60.2	±	7.7	43.2	±	1.8

5.3.3   XPS Analysis and beam line attributes

A separate set of samples was prepared using the same methods described above and shipped to the Argonne National Laboratory Advanced Photon Source (APS) synchrotron, stored in a closed container at ambient pressure and analyzed within 7 days. Radiolysis experiments were performed at the APS using 950 eV x-rays at the 4-ID-C beamline on the in-house XPS end station. Samples were irradiated under ultra-high vacuum (UHV) conditions of approximately 1×10^{-10} Torr. For the duration of the APS experiments, the synchrotron storage ring was operating in "top up" mode, such that the x-ray flux density was constant within 1-2% for any single energy. Emitted photoelectrons were detected using a Scienta Omicron Argus electron energy analyzer operated at a 10 eV pass energy. For the Au-4f$_{7/2}$ spectra, a 20 eV pass energy was used.

The angle between the incident x-ray beam and the sample normal was 60° and the beam dimensions where determined to be 150×380 µm. The incident x-ray beam flux is calculated by measuring the upstream electron current emitted from a 70% transmittance Au grid, dividing by the yield from Au for 950 eV x-rays to obtain the intensity of x-rays[166], and dividing by the measured beam area to obtain the x-ray flux, and finally multiplying by the sine of 60° to account for the angle of incidence. Deviations of the beam shape away from rectangular would lead to larger flux densities than those calculated below.

To monitor the changes in the oxygen and carbon chemical state during x-ray irradiation, multiple series (84) of O-1s and (111) C-1s spectra were obtained sequentially

over a 130 min. period. Spectra were collected using a 0.05 eV step size and a dwell time of 0.5 s for C and O and 1.0 s for P and N. Core level XPS data for each elemental transition, e.g. O-1s, C-1s, etc., were obtained at unique sample locations for each irradiation series. Although charge compensation was not employed, no shifts of the signal envelope toward higher binding energy due to positive charging of the samples from ejection of photoelectrons and secondary electrons from a non-conducting film were observed. Because the damaging electrons are generated in-film and not by an external electron source, no localized negative charge trapping was observed as expected.

5.4   High Resolution XPS of AMP

5.4.1   Fitting Procedure

The FWHM for each peak was held in constant ratio with respect to the others during an irradiation series taken at a single spot, but the ratios were allowed to vary ±10% between spots to achieve the best fit. During a single series, the FWHM of the largest peak, to which the others were constrained, was independently optimized from spectrum to spectrum, although minimal variance was observed. The inter-component spacing was determined by iteratively fitting the fixed number of components across all spectra within a single radiolysis series. Once optimal component locations were determined, the relative positions were allowed to vary ±0.2 eV from their original position during the radiation series. The same fitting constraints were applied to all spectra of a given element. The resulting radiolysis series reveal how both the relative abundance of an elemental component and the total elemental abundance at a given point on the surface change as a function of cumulative incident x-ray radiation.

5.4.2   High-resolution XPS for elemental transitions

High resolution XPS scans for the O-1s, C-1s, N-1s, and P-2p photoelectron peaks of rAMP deposited on Au are shown below. Here, the spectra have been normalized to their maximum envelope height in order to show qualitative differences in the peak shapes caused by x-ray radiation and subsequent LEE interactions with the nucleotides. The 'before' spectra were collected at a beam energy of 650 eV and a beam flux of about 6 $\times 10^{13}$ photon cm^{-2} s^{-1}. This beam energy provides a lower intensity so as not to induce detectable irradiation damage during collection of the spectra. The 'after' spectra were collected at 950 eV (beam flux of 3 $\times 10^{14}$ photon cm^{-2} s^{-1}) following irradiation to a total photon fluence of about 1 $\times 10^{18}$ photon cm^{-2}. This corresponds to an average measured electron fluence of 1.5 $\times 10^{17}$ e$^-$ cm^{-2}. While this flux implies that approximately one x-ray per surface site impacts the sample each second, the attenuation length of x-rays in the AMP and CMP films is expected to be on the order of 4 µm. Thus, only about 0.2% of the x-rays interact with nucleotides in the XPS sensitive region and no more than 5% through the entire thickness of the film [167]. Given that (i) the typical collision cascade produced by the emitted photoelectrons decays on the order of nanoseconds and (ii) the inelastic mean free path for electrons with energies below 10 eV is ~10 nm [162-165], the probability that excitations caused by multiple secondary electrons in the XPS sensitive region will overlap on a single molecule is very small. Changes to the absolute intensity for each XPS component caused by the x-ray irradiation are discussed further below.

The XPS envelope for each transition is comprised of superimposed signals from the respective elements in distinct local chemical environments. Individual components represent various bonding motifs and were modeled as Gaussian and Lorentzian product functions with a 90% and 10% weighting factor, respectively, using CasaXPS software. The integrated area of each component envelope was extracted after subtraction of a standard Shirley background [168]. The fewest number of components needed to minimize the fit residual while still representing the distinct bonding motifs present in the analyte were used to model the signal envelope. Additional peak fitting details are given in the supplemental material. The same fitting constraints were applied to all spectra of a given element.
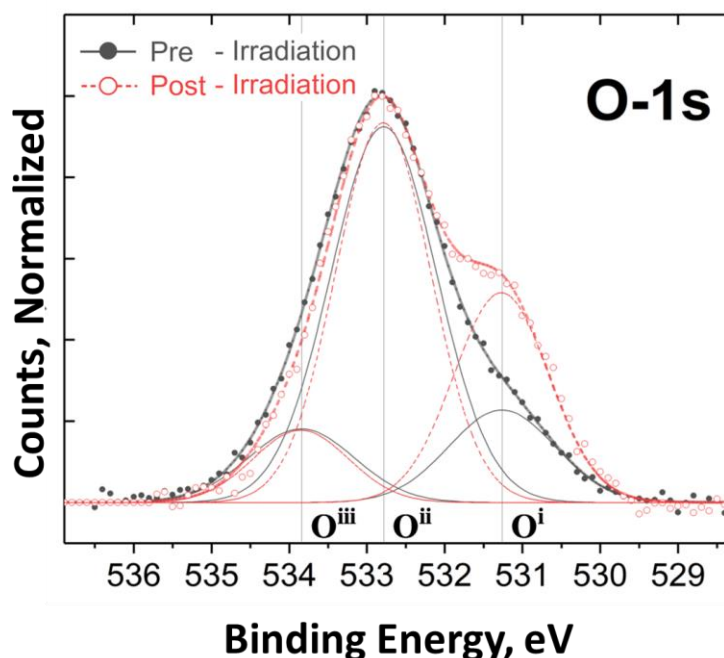
Figure 5-5   High resolution XPS spectra of rAMP O-1s transition, taken with 650 eV X-rays, before (solid) and after (dashed) a full irradiation period. The spectral envelopes are shown with thick lines, while the individual components are shown as thin lines.

The O-1s photoelectron spectra in Figure 5-5 shows three distinct peaks. The largest peak at 532.8 eV (O^{ii}) can be attributed to the C-O-C, C-O-H, and C-O-P bonds for oxygens in the sugar and phosphoester bonds[158, 169] and likely also includes contribution from adventitious O-containing hydrocarbon species[170, 171]. The peak at the lowest binding energy of 531.3 eV (O^i) can be attributed to P-only bound oxygen on the phosphate [158, 169], and the peak at the highest binding energy of 533.9 eV (O^{iii}) can be attributed to water. Due to the overlap of the adventitious hydrocarbon peak with the oxygen bonded to the sugar, the peaks do not show the exact stoichiometry expected for the nucleotide molecules. The initial percentages of O^i, O^{ii}, and O^{iii}, as calculated from the first spectra in each decay series, are given in Table 5-4. It was also observed that the dAMP samples consistently have a slightly higher percentage of O^{iii} than rAMP (14.4% vs. 9.6%). This is likely correlated with additional waters of crystallization or a deposition artifact. The O^{iii} water peak present in the samples is equivalent to between 0.5 and 1.0 waters per nucleotide molecule. Although some of this signal may be due to adventitious water accumulated during atmospheric exposure, comparison with blank spectra suggest that this contribution is negligible. Therefore, water adsorbed from the atmosphere is largely evaporated during vacuum exposure such that only a sub-monolayer remains during analysis. The water present in the O-1s spectra was most likely co-crystalized with the nucleotide from the aqueous solution during sample deposition. Due to the deposition techniques used here, it was not possible to compare the results obtained with 'dry' nucleotides. Future work using vacuum deposition techniques may allow for better determination of the effects of water content on the nucleotide damage cross sections.

In XPS analysis, decrease in signal components indicate either loss due to stimulated atomic or molecular desorption or molecular bond dissociation. Under UHV conditions, where no deposition of background gases occurs on the timescale of the experiment, growth of components indicates chemical transformations typically related to formation of new bonds. The observed decrease in the O^{ii} peak and the corresponding growth in the O^i peak can largely be attributed to the breaking of an oxygen bond associated with the sugar (O^{ii}) and the formation of an additional P-O (O^i) bond. Though O^i is attributed to only phosphate bonded oxygen species when describing the initial state of the analyte, oxygen atoms in carbonyl groups are also expected to possess about the same binding energy[169, 172]. From the oxygen data alone, it is not possible to discern whether the observed nucleotide damage results principally from C-O cleavage at the phosphoester site or the formation of a carbonyl motif, likely associated with the sugar. Since the identity of the radiation-induced formation of a new bonding motif needed to explain the growth of the O^i peak is ambiguous based on only the O-1s spectra, the C-1s spectra must also be considered.
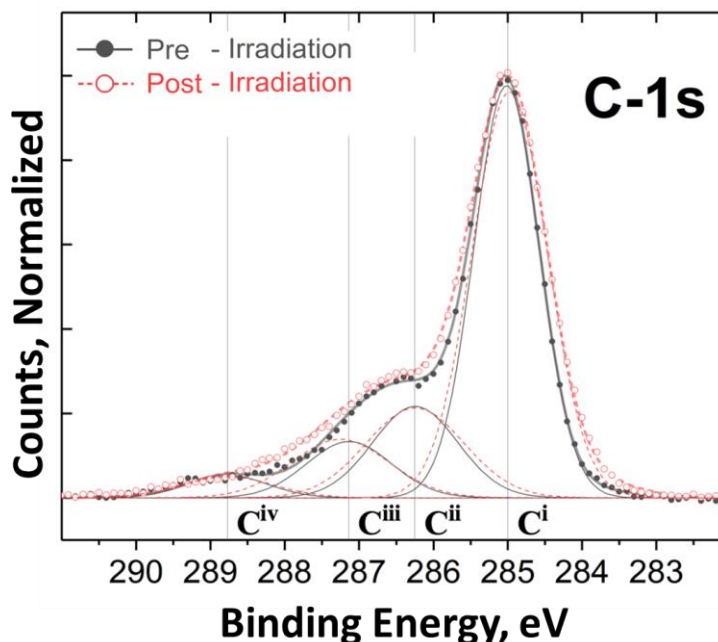
Figure 5-6 **High resolution XPS spectra of rAMP C-1s transition, taken with 650 eV X-rays, before (solid) and after (dashed) a full irradiation period. The spectral envelopes are shown with thick lines, while the individual components are shown as thin lines.**

The carbon C-1s signal, shown in Figure 5-6, is best fit using four component peaks. The largest peak at 285.0 eV (C^i) is due to adventitious carbon and has a standard deviation of ~7.6% between samples, much larger than the relative variation in the nucleotide components. The decrease in absolute intensity is also the largest of all the C-1s components. However, it is likely that much of this desorption is occurring from the bare Au surface and therefore does not affect the nucleotide photoelectron signal. Despite the large differences in abundance of the C^i component between samples, no effect on the calculated cross sections was observed and therefore it is expected that contributions from atmospheric hydrocarbons can be neglected. As seen in Table 5-4, the peak at 286.4 eV (C^{ii}) makes up on average about 75% of the total remaining carbon signal when ignoring

contributions from adventitious carbon species (C[i]). The C[ii] peak can be assigned to the six carbon atoms contained in the C–O, C–N, and N-C–N bonds [158, 169] as well as C-O-C bonds on residual hydrocarbons. The peak at 287.6 eV (C[iii]) can be attributed to the carbon atoms in the N=C-N and C-NH$_2$ bonding motifs, as well as carbonyl functionalities [173]. The final peak at 289.0 eV (C[iv]) can be assigned to the glycosidic N-C-O bond. This transition has received the least consideration in the XPS literature of DNA and its constituents. The C[i] - C[iv] peak assignments are in general agreement with previous published values for DNA [158, 169, 174, 175] and adenosine [176], although there is some variation in literature values for the C[iii] and C[iv] peaks.

As mentioned above, there is ambiguity regarding the nature of the formative O[i] peak as both carbonyl and phosphate motifs are expected to have O-1s binding energies around 531 eV. Analysis of the C-1s spectra can help discern between these two possibilities. The behavior of the C-1s spectra resulting from C-O-P cleavage between the O and C would result in the bond most likely remaining in the C[ii] component or possibly shifting to C[i]. Alternatively, if the O[i] peak increase is due to carbonyl formation, the formation of a new carbonyl motif would be expected to result in a net increase in the C[iii] region [173], mirroring the O[i] component growth. Since there is no net increase in the C[iii] peak, we conclude that the O-1s formative component results from C-O cleavage of the C-O-P linkage.
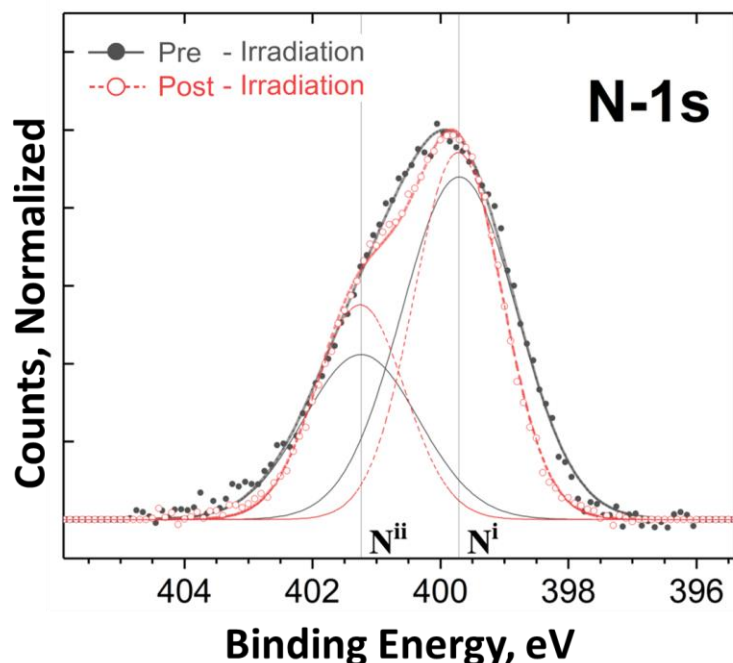
Figure 5-7   High resolution XPS spectra of rAMP N-1s transition, taken with 650 eV X-rays, before (solid) and after (dashed) a full irradiation period. The spectral envelopes are shown with thick lines, while the individual components are shown as thin lines.

The intensities of the signals due to the N-1s and P-2p peaks, shown in Figure 5-7, were insufficient to obtain fluence-resolved irradiation series. However, high-resolution scans of these transitions before and after irradiation are sufficient to resolve the various components and determine qualitative spectral changes. The N-1s signal can be separated into an imine, e.g. -N=, peak at 399.7 eV (N^i) and an amine, e.g. -NH$_2$, peak at 401.2 eV (N^{ii}) [158, 176]. The N-1s spectra taken in post-irradiation regions show a reduction in imine bonds totaling no more than 0.5% relative to the amine as shown in Table 5-3. The relative lack of change in the N-1s peak ratios before and after irradiation of the AMP samples suggests there is minimal damage to the nucleobase due to the irradiation.

Table 5-3 **N-1s XPS for r/dAMP combined, reported as the average ± the standard deviation (%). Analysis of the N-1s transition of AMP and CMP before and after ~1 hr of x-ray exposure. As described in the text, there are only two motifs for N-1s transition, and component ii refers to an amine (–NH$_2$). The ratio of components is essentially unchanged after the irradiation process. For CMP, only 1 pre-irradiation N-1s spectra was taken and no post-irradiation.**

Irradiation Condition	Contribution of Component N^{ii}, %		
Pre	35.1	±	5.0
Post	35.3	±	0.8
Predicted	40		

The P-2p transition, Figure 5-8, shows the expected 1:2 ratio split 2p structure with the 2p$_{3/2}$ band centered at 133.8 eV (P^i). Since there were no before and after scans taken for N and P at the same sample location, no determination of the loss or growth of these peaks in terms of the absolute signal could be determined.
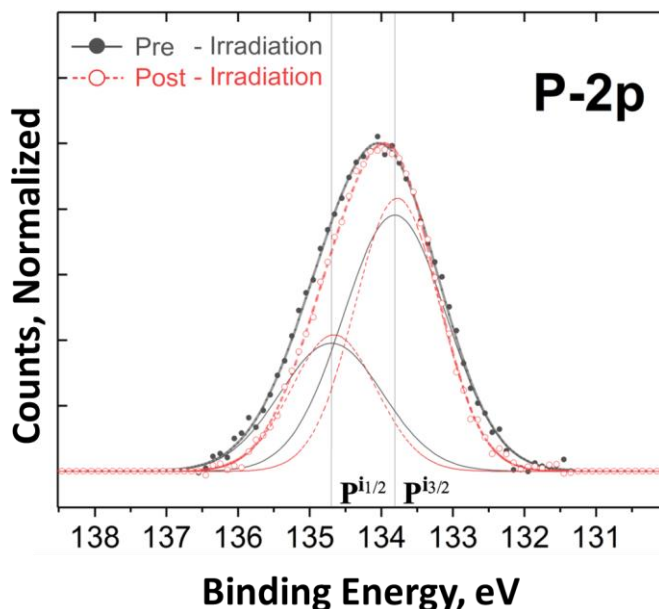
Figure 5-8 **High resolution XPS spectra of rAMP P-2p transition, taken with 650 eV X-rays, before (solid) and after (dashed) a full irradiation period. The spectral envelopes are shown with thick lines, while the individual components are thin lines.**

Since drop-casting the analyte dispersed in a hydrated solution onto the hydrophobic Au surface leads to variations in the local analyte abundance, the proportions of the individual components are not in exact agreement with the expected stoichiometric ratios. Exposing the sample to lab atmosphere in dehydrated form will also lead to adsorption of atmospheric carbonaceous species and water vapor, thus contributing to the total signal envelope. However, careful analysis of the component binding energies and comparison with blank samples can allow accurate background contributions to be identified. Although the contribution to the XPS signal from adventitious atmospheric species can vary significantly between sample spots, the similarity of the nucleotide damage behavior in all spots indicates that atmospheric contributions can be neglected.

5.4.3   Identification of Bonding Motifs

Corrections to the peak positions for small variations in the surface work function depending on sample location were made by shifting the Au 4f7/2 peak (Figure 5-4) so its maximum is at 84.0 eV. All other peaks taken at the same sample location were then shifted by an equal amount to determine the absolute positions of the individual components. This resulted in excellent positional overlap of all remaining r/dAMP, and r/dCMP spectra. The average positions of the various atomic transitions and their corresponding assignments to the various bonding motifs present in the analyte molecules are shown in Table 5-4 and discussed in greater detail below. To account for any variations in XPS signal intensity due to fluctuations in the incident x-ray intensity, all integrated

components of a given spectrum were normalized to the average incident x-ray flux measured during the collection of that spectrum.

Table 5-4   **Positions and chemical motifs associated with each of the spectral components used to model the XPS spectral envelopes. The average component percentages present in the spectra were calculated using the initial decay spectra for C-1s and O-1s, while spectra taken after irradiation were used for N-1s. For the C-1s components, Ci, which is associated with adventitious hydrocarbons resulting from atmospheric exposure, are shown in parenthesis and were neglected in the calculation of the percentages of Cii – Civ.**

Core Level	Component Label	Binding Energy (eV)	Composition %		Motif Assignment
			rAMP	dAMP	
O-1s	i	531.3	21.4	21.2	P-OH, P=O, P-O⁻, C=O
	ii	532.8	69.0	64.4	C-O-C, C-O-P, C-OH
	iii	533.9	9.6	14.4	H_2O
C-1s	i	285.0	(59.1)	(68.1)	Hydrocarbon molecules
	ii	286.4	78.8	73.4	C-O, C-N, N-C-N
	iii	287.6	12.4	15.0	N-C=N, C-NH_2, O=C-R
	iv	289.0	8.8	11.6	N-C-O, N-(C=O)-N
N-1s	i	399.7	64.0	65.3	imine (-N=)
	ii	401.2	36.0	34.7	amine (NR_3, -NH_2)
P-2p$_{3/2}$	i	133.8	--	--	P-OH, P=O, P-O⁻

5.5 Damage Cross Section

Secondary electrons play a prominent role in the chemical changes produced by x-ray irradiation. Therefore, cross sections for low energy electron-induced reactions were determined by measuring the current of secondary electrons emitted from the analyte and Au surface, or total electron yield (TEY).

5.5.1 Data Preparation

The TEY is monitored through the conductive substrate via a current amplifier that measures the restoring current needed to maintain charge neutrality on the electrically isolated sample holder. By dividing the measured TEY values by the measured x-ray beam area, an appropriate flux density of secondary electrons leaving the surface and, by proxy, impacting in the uppermost <10 nm of the sample surface can be determined. Thus, the TEY is directly used to estimate the flux density of LEEs within the nucleotide layer sampled by the XPS measurements. This secondary electron flux density was used to determine the cumulative electron fluence passing through the XPS sensitive region.

The various XPS spectra component areas are plotted below as a function of cumulative secondary electron fluence over the span of the entire radiolysis duration. Irradiating the samples for approximately 1 hour causes the total area of the O-1s and C-1s envelopes to decrease by on average 20% and 15%, respectively. The radiolysis series are modeled as a single exponential decay,

$$I = I_0 * e^{-F/\tau} \tag{3}$$

where I represents the integrated component area, I_0 is the initial component area and F is the secondary electron fluence associated with the spectra [177]. The inverse of the time constant parameter, τ (e^-/cm^2), represents the damage cross section, σ (cm^2/e). As already mentioned, these cross sections include bond breaking, bond formation, and stimulated desorption.

5.5.2 *Adenosine monophosphate analytes*

The cross-sections determined from the O-1s and C-1s exponential decay fits are given in Table 5-5 in terms of Mb where 1 Mb = 10^{-18} cm^2.

5.5.2.1 <u>Cross Section Calculations</u>
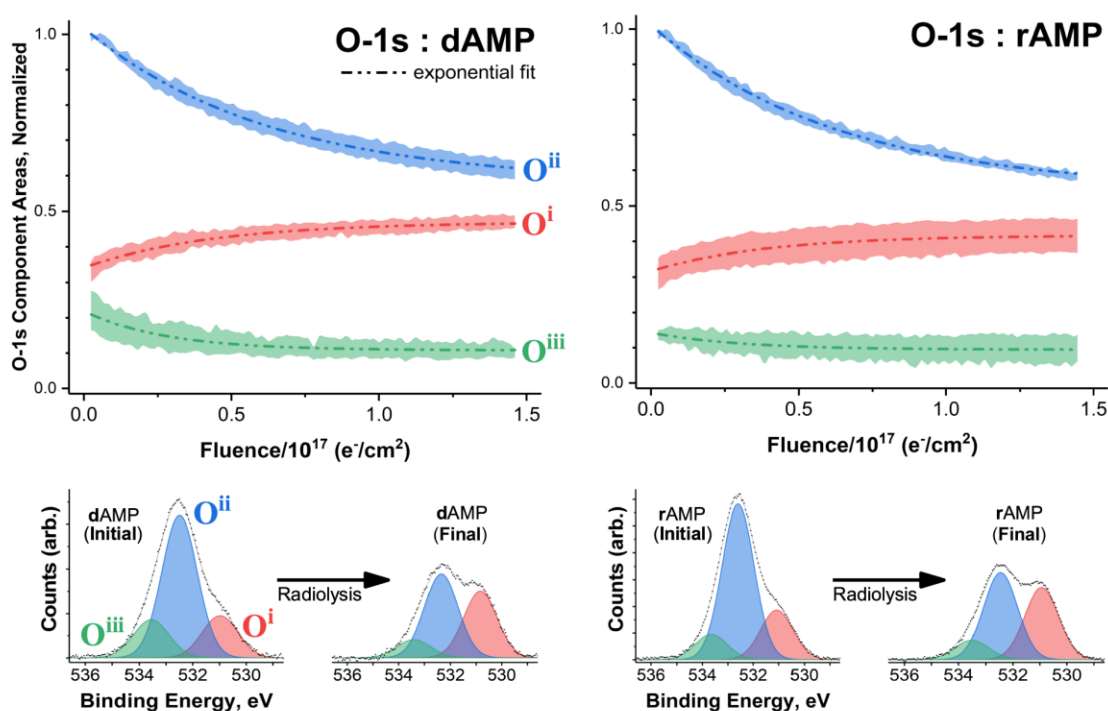
Figure 5-9 **O-1s transition integrated component areas, as a function of electron fluence, for both ribo- and deoxyribo- adenosine nucleotides. All component profiles have been normalized to the Oii pre-irradiation area in order to account for**

differences in the analyte spot to spot concentration and intensity due to beam fluctuations. The area vs. fluence profiles were modeled by a single exponential decay function to derive the damage cross section. Representative before and after spectra for dAMP and rAMP are shown to demonstrate qualitative changes in the O-1s spectral envelope which result from irradiation. The spectra show the absolute XPS signal and the decrease in the overall envelope indicates a net loss of oxygen from the sample surface.

The fluence dependence of the O-1s spectra are shown in Figure 5-9, and the spectra below the decay cures show how the overall intensity of each component changes due to irradiation. The component decay curves for each sample location have been normalized to the O^{ii} pre-irradiation area to account for local variations in the amount of analyte visible to the XPS. The data represent seven and eight unique trials for rAMP and dAMP, respectively, with 84 individual spectra comprising each decay curve. In an average O-1s decay series, an approximately 25% reduction in the O^{ii} peak, a 5% reduction in the O^{iii} peak, and a 10% increase in the O^i peak relative to the initial total envelope area was observed. This can be seen clearly in the initial and final scans shown at the bottom of Figure 5-9. The O^{iii} signal decreases the most rapidly with an average cross section of about 40 Mb ($4x10^{-17}$ cm^2) for both dAMP and rAMP. The similar cross sections, especially for the O^i component which represents phosphate/sugar C-O cleavage, imply that the identity of the sugar does not strongly affect the overall LEE induced damage process. To confirm if the component resolved cross sections are distinct based on the identity of the sugar for analyzed nucleotides a two-sample t-test was employed, $\alpha=0.05$, equal variance assumed (Table 5-6). No statistical differences between the dAMP and rAMP cross sections were observed. The decrease in intensity of the O^{ii} peak is larger than the increase in the O^i peak due to the contribution from desorption of adventitious species and analyte molecule fragments. However, as indicated in Table 5-5, the O^{ii} cross section

is smaller than the O^i cross section, suggesting that the desorption cross sections which contribute to the overall Oii cross section are smaller than for the C-O cleavage.

Figure 5-10 – C-1s transition integrated component areas, as a function of electron fluence, for both ribo- and deoxyribo- adenosine nucleotides. All included component profiles have been normalized to the C^{ii} pre-irradiation area in order to account for differences in the analyte spot to spot concentration and intensity due to beam fluctuations. The largest component (Ci) is not shown due to it being ascribed to adventitious carbon. The area vs. fluence profiles were modeled by a single exponential decay function to derive the damage cross section, except C^{iii} which was modeled using a two-component exponential growth and decay function. Representative before and after spectra for dAMP and rAMP are shown to demonstrate qualitative changes in the C-1s spectral envelope which result from irradiation. The spectra show the absolute XPS signal and the decrease in the overall envelope indicates a net loss of carbon from the sample surface, with losses of C^i and C^{ii} being the largest.

The decay curves for the C-1s peak components, which are comprised of 111 individual spectra, are given in Figure 5-10. Each of the carbon component peaks was normalized to the initial C^{ii} component area to show similarities between sampled regions

and the C^i component is not shown. The C-1s components showed average decreases of 6%, 6%, 1%, and 2% for C^i thru C^{iv}, respectively, relative to the initial total envelope area. The C^{ii} and C^{iv} peaks decrease with increasing irradiation whereas in most series, there is a small initial increase in the C^{iii} peak, and then a slow decrease. Although some series could be fit with an exponential growth curve followed by an exponential decay, the growth curves were variable so no convergence was found. The C^{iii} decay curve decreases very little indicating that the initial carbon motifs assigned to this component are relatively stable.

Table 5-5   Cross sections associated with all XPS regions for AMP nucleotides, reported as the average ± the standard deviation (Mb).

Core Level	Component Label	Molecule	Cross Section		
O-1s	**i**	**d**AMP	23.4	±	4.4
		rAMP	22.3	±	2.7
	ii	**d**AMP	14.5	±	0.7
		rAMP	14.1	±	3.2
	iii	**d**AMP	43.9	±	16.7
		rAMP	38.0	±	15.6
C-1s	**ii**	**d**AMP	18.2	±	4.4
		rAMP	23.7	±	3.9
	iii$_{decay}$	**d**AMP	4.0	±	3.1
		rAMP	4.9	±	6.0
	iv	**d**AMP	20.4	±	2.4
		rAMP	18.6	±	2.6

5.5.2.2   Hypothesis Testing

To assess if damage cross sections could be considered distinct and therefore a demonstration of a potentially prebiotic proto-RNA transformation mechanism, hypothesis testing was applied to the data. A two-sample t-test was used on the samples sets of cross sections for each nucleotide. Using an α value of 0.05, the difference in

sample averages was considered significant if p<0.05. The results of all t-test are outlined in Table 5-6.

Table 5-6   Summary of O-1s and C-1s cross sections and t-test results for AMP analytes.

Component	Molecule	t-value ($\sigma_d \neq \sigma_r$)	Degrees of Freedom	p-value	Result (α=0.05)
O^i	**d**AMP **r**AMP	0.555	13	0.588	NOT significant
O^{ii}	**d**AMP **r**AMP	0.324	13	0.751	NOT significant
O^{iii}	**d**AMP **r**AMP	0.709	13	0.491	NOT significant
C^i	**d**AMP **r**AMP	0.086	6	0.934	NOT significant
C^{ii}	**d**AMP **r**AMP	-1.865	6	0.111	NOT significant
C^{iii}_{growth}	**d**AMP **r**AMP	-0.022	4	0.983	NOT significant
C^{iii}_{decay}	**d**AMP **r**AMP	-0.260	4	0.807	NOT significant
C^{iv}	**d**AMP **r**AMP	1.025	6	0.345	NOT significant

156

5.5.3 Cytosine monophosphate analytes

To explore the role of the nucleobase, similar experiments to those described above were carried out for rCMP and dCMP. A molecular representation of rCMP is provided in Figure 5-11, with the elemental motifs labeled. Only two unique trials each were taken for rCMP and dCMP, and therefore the statistical interpretation is substantially weaker, compared the AMP dataset. Similar trends are observed, however, further analysis is needed to make defensible statements. The O-1s and C-1s decay curves for these molecules are shown in Figure 5-12.
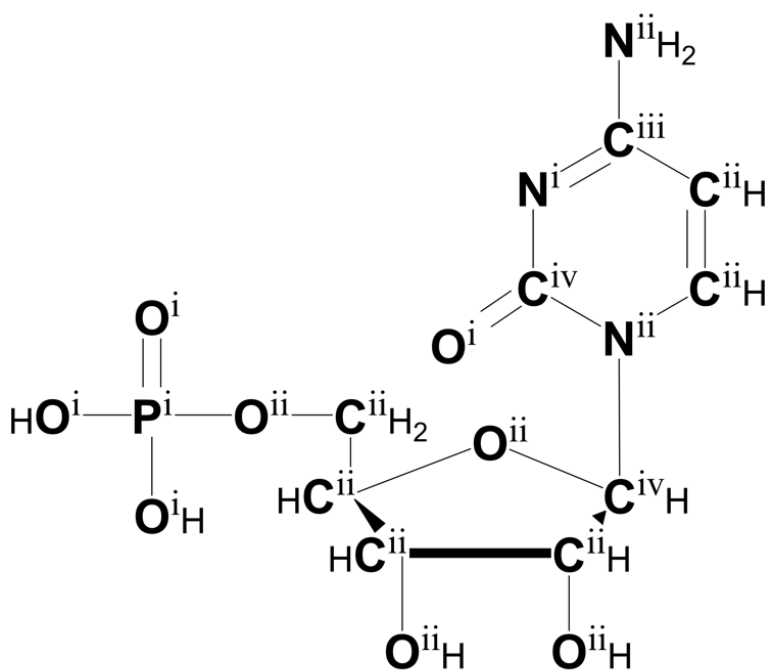
Cytidine 5'-monophosphate (**r**CMP)

Figure 5-11   Depiction of cytosine monophosphate with all atoms labeled to correspond to XPS components. The assignments do not differ from AMP molecules in the phosphate and sugar regions. The absence of the 2' oxygen, in the case of dCMP, does not change the assignment of the corresponding carbon.

Similar to AMP results, the same three components appear in roughly equal ratios, and the increasing O^i and decreasing O^{ii} peak behavior is generally the same as for the AMP samples. Likewise, C^{ii} and C^{iv} are seen to decrease while C^{iii} remains effectively constant.

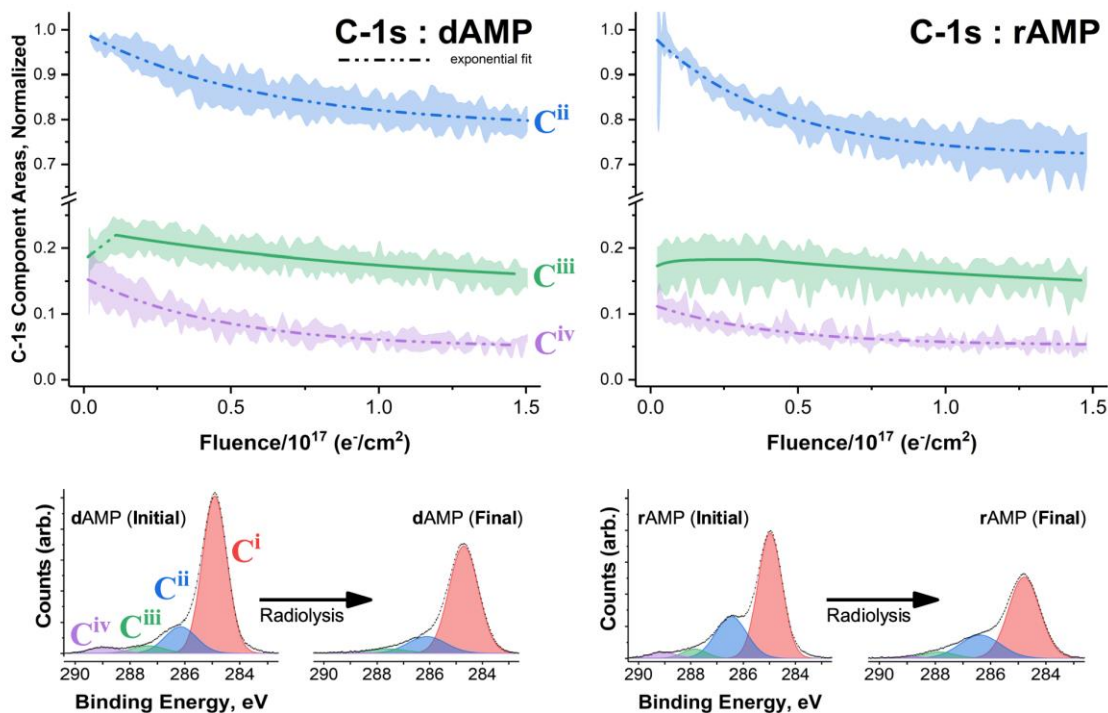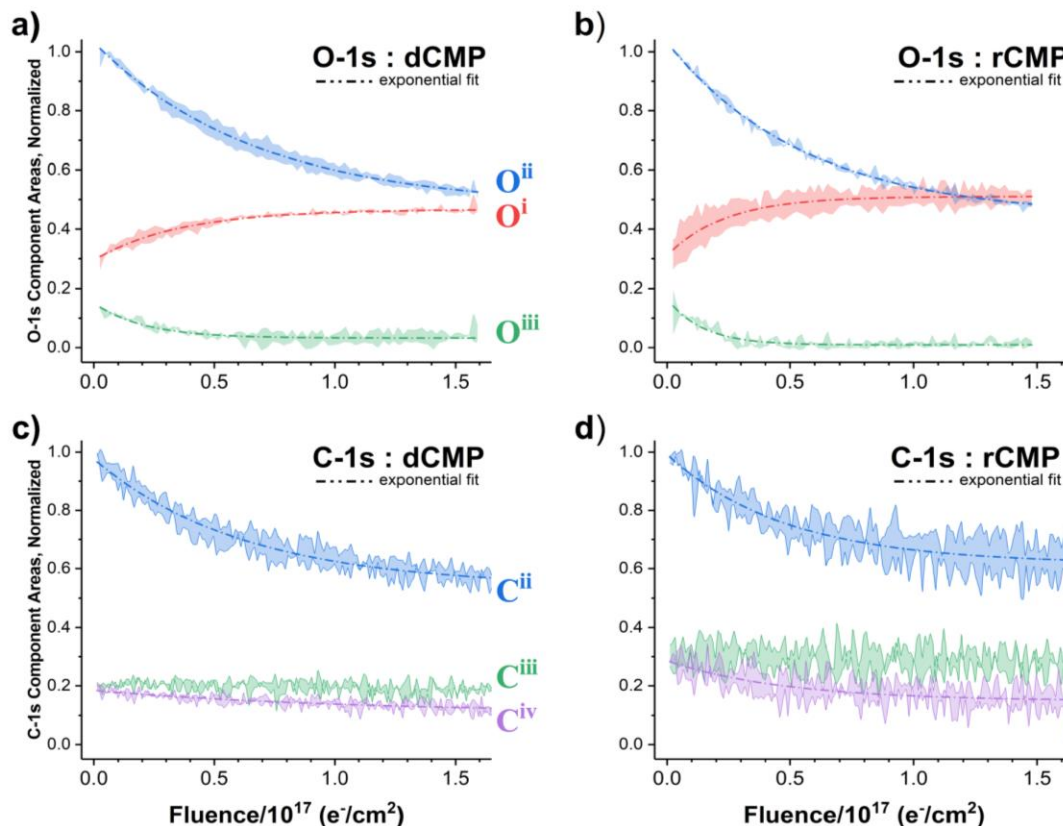**Figure 5-12   O-1s and C-1s transitions integrated component areas, as a function of electron fluence, for both ribo- and deoxyribo- cytidine nucleotides. All component profiles have been normalized to the Oii pre-irradiation area in order to account for differences in the analyte spot to spot concentration and intensity due to beam fluctuations.**

The final concentration of oxygen in the O^i peak is higher than for the AMP molecules, and the CMP cross-section values, given in Table 5-7, are correspondingly larger than for the AMP molecules. Like AMP, there is no statistically significant difference in the r- and d- forms of the sugar. However, the O^{ii} cross-sections are similar

to that found for AMP, while the O^i and O^{iii} cross-sections are 1.5-2.0 times larger. This

suggests that both oxygen phosphoester bond cleavage and water loss from the substrate

are more efficient in CMP than in AMP. Additionally, the smaller average C^{ii} and C^{vi} cross

sections for CMP suggest that the sugar subunit is slightly more stable than for AMP. More

studies are needed to determine the full cross section dependence for nucleobase variation.

Table 5-7   Cross sections associated with all XPS regions for CMP nucleotides, reported as the average ± the standard deviation (Mb).

Core Level	Component Label	Molecule	Cross Section		
O-1s	i	**d**CMP	30.7	±	9.5
		rCMP	32.8	±	19.2
	ii	**d**CMP	9.1	±	2.1
		rCMP	17.9	±	2.9
	iii	**d**CMP	65.4	±	17.9
		rCMP	75.4	±	11.5
C-1s	ii	**d**CMP	13.6	±	0.7
		rCMP	14.7	±	2.7
	iv	**d**CMP	6.8	±	0.6
		rCMP	15.1	±	1.2

The same hypothesis testing procedure was applied the CMP results; a two-sample

t-test was used with an α value of 0.05. The difference in sample averages was considered

significant if p<0.05. The results of all t-test are outlined in Table 5-8.

Table 5-8   Summary of O-1s and C-1s cross sections and t-test results for CMP analytes.

Component	Molecule	t-value ($\sigma_d \neq \sigma_r$)	Degrees of Freedom	p-value	Result (α=0.05)
O^i	**d**CMP **r**CMP	-0.144	2	0.899	NOT significant
O^{ii}	**d**CMP **r**CMP	-3.419	2	0.076	NOT significant
O^{iii}	**d**CMP **r**CMP	-0.668	2	0.573	NOT significant
C^i	**d**CMP **r**CMP	0.311	2	0.785	NOT significant
C^{ii}	**d**CMP **r**CMP	-0.582	2	0.619	NOT significant
C^{iii}_{growth}	**d**CMP **r**CMP	0.953	2	0.441	NOT significant
C^{iii}_{decay}	**d**CMP **r**CMP	1.242	2	0.340	NOT significant
C^{iv}	**d**CMP **r**CMP	-9.032	2	0.012	**Significant**

5.6   Proposed Mechanism of Nucleotide Damage

Irradiation with 950 eV photons causes the relative intensities of the O-1s and C-1s photoelectron components to change indicating specific bond formation and breakage in ribo- and deoxyribo-nucleotides studied. There is also on average a 20% total signal decrease due to loss of analyte molecules and adventitious species from the substrate. The experimental results indicate that x-ray irradiation reduces the intensity of the O^{ii} peak, associated with oxygen on the sugar subunit, while the intensity of O^i peak, associated with the phosphate subunit, is seen to increase. This behavior, outlined in Figure 5-13, can be described by the cleavage the C-O-P bond between the carbon and 5'-oxygen in the phosphoester bond. As indicated by the XPS spectra included in Figure 5-13, this

transformation results in a corresponding shift in binding energy due to formation of a new phosphate oxygen motif.
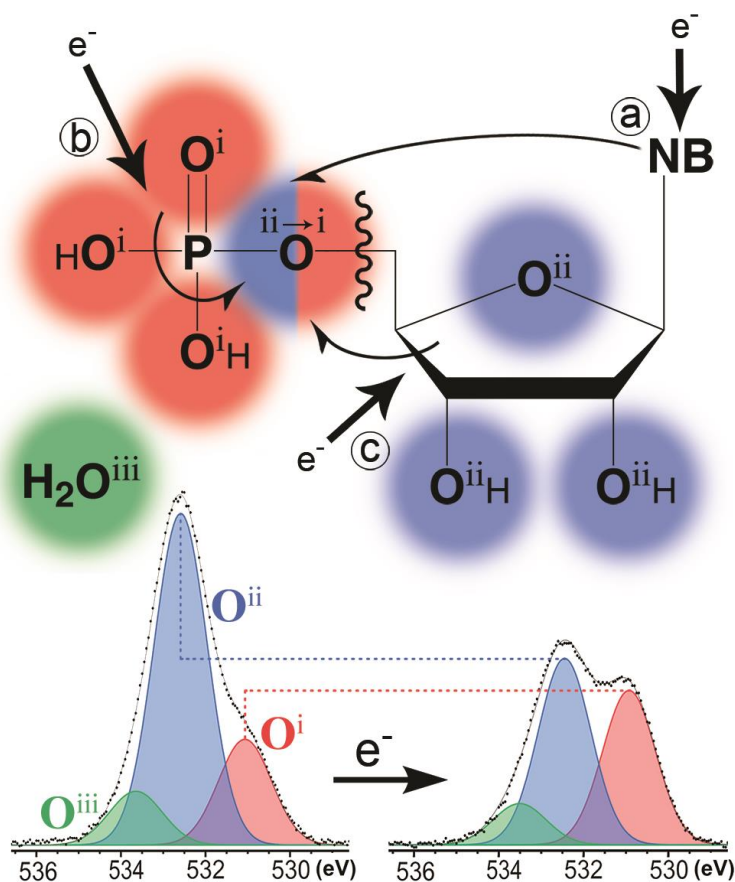
Figure 5-13   Depiction of the primary chemical transformation observed, annotated with XPS assignments. The cleavage of the phosphoester bond between the carbon and 5' oxygen is denoted by a wavy line. The 5' oxygen, initially assigned as Oii, shifts in binding energy upon cleavage and is subsequently assigned as Oi. The damage can involve several pathways: a) nucleobase capture followed by resonant excitation, b) phosphate capture followed by direct dissociation, and c) sugar capture followed by resonant excitation.

The cross sections for phosphoester bond cleavage are 70% larger for CMP molecules than for AMP under similar irradiation conditions. The sugar damage cross sections are also somewhat smaller for CMP suggesting a possible effect of the nucleobase identity. Decays in the C^{ii} and C^{iv} signals of the AMP molecules also suggest that the sugar

subunit undergoes significant fragmentation and desorption. In both AMP and CMP molecules, it is seen that the identity of the sugar does not discernably affect the overall LEE induced damage process. While this scheme may qualitatively account for the behavior of the O-1s transition throughout the irradiation process, the expected formation of a C-H motif in the C-1s spectra is not directly observed.

The slight initial build-up of the C^{iii} component followed by a slow decay and the lack of carbonyl bond formation indicates the potential preferential damage or removal of the sugar. The preferential damage and removal of the sugar also suggests potential build-up of the nucleobase subunits in the near vacuum-surface region sampled by the XPS. The similarity of N-1s spectra in both pristine and irradiated regions, also indicates that the nucleobase is relatively stable under our film and irradiation conditions. Nucleobase excision may occur in place of damage [178, 179] but it does not appear to be a major channel under our experimental conditions. In summary, Figure 5-13 shows the damage can involve several pathways: a) nucleobase capture followed by resonant excitation, b) phosphate capture followed by direct dissociation, and c) sugar capture followed by resonant excitation.

Though no reported values for LEE cross section damage of nucleotides appear in the literature, comparisons with those measured for DNA and nucleotide constituents can be instructive. Reported cross sections for 10 eV electron damage of nucleobases were 10-50 Mb, similar to the values reported here [180]. However, the damage cross sections reported here for cleavage of the nucleotide C-O phosphoester bond are about 2-5 times larger than previous values reported for external, mono-energetic LEE beam irradiation

162

[181] and synchrotron x-ray [158] studies for DNA thin films. These differences can be explained by larger expected secondary electron yields from the Au substrate than for the crystalline nucleotide islands. Previous measurements considering x-ray irradiation of DNA have shown a factor of 4 to 7 enhancement in damage of thin (15 nm) DNA films deposited on Ti compared to thick films (20 µm) [182]. The enhancement can be explained due to the fact that the bulk of the thick films were exposed exclusively to secondary electrons originating in the DNA, while the thin films experience a significant contribution from the underlying Ta substrate[167]. Similar behavior was seen by contrasting an insulating glass surface with a metal where the metal showed greater damage at similar x-ray fluxes [156, 167].

5.7 Conclusions

Radiation damage and desorption of nucleotides 2'-deoxyadenosine 5'-monophosphate (dAMP), adenosine 5'-monophosphate (rAMP), 2'-deoxycytidine 5'-monophosphate (dCMP) and cytidine 5'-monophosphate (rCMP) deposited on 200 nm Au films have been measured using x-rays as both the probe and source of slow electrons. Fitting the flux dependent data to a single exponential decay yields damage cross sections of 23.4, 22.3, 30.7 and 32.8 Mb for dAMP, rAMP, dCMP and rCMP, respectively. The cross sections for sugar damage were slightly lower and statistically similar between dAMP, rAMP, dCMP and rCMP. The base was found to be relatively stable with a low damage cross section (~5 Mb). Though there is no statistical difference between the stability of the sugar forms, changing the base from adenine to cytidine causes a slight increase in the damage cross section. In view of the expected energy distribution of the secondary electrons, the observed damage is dominated by the inelastic energy-loss

channels associated with secondary electron capture and transient negative ion decay. These decay pathways will depend upon the local potentials, many body interactions and the presence of water. Thus, these effects must be taken into account when assessing the overall efficacy of LEEs and DEA channels.

CHAPTER 6.   CONCLUSIONS AND FUTURE DIRECTIONS

6.1   Conclusions

The motivation underlying experimental design and direction for work included in this thesis began and persisted as the pursuit of describing the effect a mineral substrate might have within prebiotic chemical environments. The primary framework for this pursuit has been the depsipeptide protein-progenimer system. The co-reaction of α-hydroxy acids and amino acids offers a new and robust pathway towards polypeptide formation in mild and plausible prebiotic conditions. Work presented here has built upon the principles of the homogeneous depsipeptide reaction, and contributed to them in specific and general ways, in the context of minerals and chemistry at an interface.

The first demonstration of depsipeptide formation in the presence of a heterogeneous substrate has been described. Two amino acid species, alanine and glycine, were incorporated into mixed ester/amide linked oligomers in the presence of silica. Not only were conversion yields for the amino acids within a factor of 2 from those of the homogeneous reaction, but the composition of the oligomer products were distinct. It has been shown that depsipeptides formed in the presence of silica are amino acid enriched. Compared to homogeneous reaction products, these depsipeptides have fewer ester linkages and more contiguous amino acid residues. While it had not been directly observed yet, the covalent interaction between the hydroxy acid and the silica surface was a demonstration of amino acid poly-condensation via surface-ester aminolysis.

This result comes as a rare account of a mineral-like substrate operating in a manner other than simply increasing a reaction rate, and instead altering the inclusion ratio between two similar reactants. For this effect to be facilitated by silica stands as another uncommon account. In many comparative substrate experiments for amide formation, silica is typically an under performer. However, the depsipeptide system seems to be a chemical environment that is well suited for the characteristic of silica. The precise reason for this match, however, was not able to be elucidated using the same amino acid and hydroxy acid reactants.

Revisiting the depsipeptide reaction with modified hydroxy andic and amino acid analogs provided a route towards identifying and describing the process that likely contributed to the amino acid enrichment previously observed. Mono-functional versions of hydroxy acids (MOPA) and non-monomeric amino acids (NAG) established a system where the only activated ester complex that could form would be at the silica surface. It was determined that silica is capable of forming ester bonds with hydroxy acid-like molecules, but not amino acid monomers. Due to the zwitterionic nature of amino acids in moderate pH conditions, the carboxylate is not well-suited for ester formation. However, it was shown that silica can esterify with a C-terminus amino acid residue analog (NAG) and an actual oligopeptide C-terminus residue (G_3). More than just esterification, amino acid poly-condensation can occur entirely on the surface, if an ester-initiator is present, e.g. MOPA or NAG. A parallel study with quartz, which yielded no covalent interaction, suggests that isolated silanols are a necessity for silyl-ester aminolysis to occur.

The analysis of a whole cohort of prebiotic minerals with the same chemical tools used to determine and propose a mechanism for silyl-ester aminolysis yielded a variety of interesting results. While isolated surface hydroxyls and a low PZC describe necessary

166

characteristics between fumed silica and quartz, they are not wholly predictive of esterification ability, given results from several of the clay minerals. It was made clear that a PZC exceeding the reaction pH assured that esterification would not occur, but instead could catalyze direct amide formation from the carboxylate form. Which is a very important distinction to be made. Minerals are known to catalyze polypeptide formation in exclusively amino acid systems, and that mechanism involves amino acid carboxylates and a positive surface. However, not all minerals are positively charged at this reaction pHs and not all have surface hydroxyls, such as Al_2O_3. The inability of silica to interact with amino acids in the same way that TiO_2 does, merely demonstrates that the incredibly diverse population of minerals also requires a diversity of possible poly-condensation mechanisms, and surface-ester aminolysis has now been show as a viable pathway.

6.2   Future Directions

The chemical origins of life has not been precisely determined at present. Accordingly, there are several avenues of continued inquiry that are particularly related to, and extensions of, the work described in this thesis. Minerals were, and will continue to be, a ubiquitous presence on rocky planets in many distinct sub-environments.

6.2.1   *Continuation of MOPA/NAG-tests for various prebiotic minerals*

The results outlined in CHAPTER 4 might serve as a framework for continued investigation of a wide variety of mineral substrates reacting with a limited number of "test" molecules. Both the group of minerals studied as well as the analysis approaches must be carefully selected to extract useful information; an experimental cohort that is designed to describe the relationship between mineral and depsipeptide chemical reactions

167

for a broader set of substrates especially pertinent to the chemical origins of life should be a priority. While the work discussed here relates to the topic of chemical evolution, Earth's lithosphere has likewise undergone a series of transformations due to physical and chemical processes that has resulted in a variable mineralogical inventory over time. In the post-accretion epoch (4.5-4.0 Ga), igneous rocks began forming as hydroxides and clay minerals, joining olivines, other phyllosilicates and many others [183]. This set is of particular interest for two reasons: inclusion of minerals that participate in the serpentinization process and the presence of both silicate and hydroxide mineral classes. Serpentinization is a metamorphic process where mafic minerals like olivine $(Mg,Fe)_2Si_2O_4$ are transformed into hydroxide silicates, such as lizardite $Mg_3Si_2O_5(OH)_4$ and other hydroxide products. These highly exothermic reactions have been postulated to serve as potential sources of energy that could have driven production of necessary prebiotic building blocks, such as glyoxylate, in addition to general chemosynthesis by early life forms predating photosynthesis.[184] In addition to relevance to prebiotic chemistry, minerals in this process are well suited to exploring the applicability of ester aminolysis at a surface.

Considering a limited number of members (fayalite: Fe_2SiO_4, forsterite: Mg_2SiO_4, iron hydroxide: $Fe(OH)_2$, brucite: $Mg(OH)_2$, lizardite: $Mg_3Si_2O_5(OH)_4$), several traits shared by these minerals are hydroxyl functionalities, either as explicitly part of the crystal or just as a defect termination, and high points of zero charge (PZC). These substrates would aide in addressing important questions regarding the mechanism summarized in section 4, by testing the type of hydroxyl that can participate in esterification as a nucleophile (Fe-OH, Mg-OH, etc.), if explicitly hydroxide minerals or just oxides are better

suited for esterification (e.g. $XSiO_4$ or $XSi_2O_5(OH)$) and if such esterification reactions can proceed at a surface which has a net positive charge due to the high PZC. While this mineral set contains mostly nesosilicates, the end product of serpentinization, e.g. lizardite, is a phyllosilicate. This will bridge previous work involving depsipeptide systems and kaolinite. This cohort, together with other clays or kaolinite class minerals which possess a negatively charged surface at reaction conditions of pH 3, will span a parameter space that will contribute to the ability to predict the behavior of prebiotic minerals in depsipeptide systems.

New analysis approaches, in addition to MS and Infrared spectroscopy, are needed to properly address this topic. While the results suggest that there are correlations between detectable "isolated" hydroxyl terminations, PZC values and surface esterification capabilities, there are also anomalous results that require additional analysis. Montmorillonite, for example, was capable of esterification with NAG, but lacked discernable isolated hydroxyls via IR analysis. In fact, the OH region looked exactly like quartz, that was incapable of NAG esterification, and both have similar and low PZC values. It is likely a product of the elaborate sheet-like structure associated with this mineral and other clays. This type of characteristic must be understood in order to develop a model or attribute list that can predict behavior of depsipeptide systems in the presence of any mineral.

6.2.2 *Self-Sustaining Ester-Aminolysis Amino Acids*

In addition to mineral diversity, amino acids other than glycine and alanine should be investigated in a model depsipeptide system. While neutral side-chain amino acid are

convenient during simple oligomerization studies, the reality is that charged side-chain residues existed concurrent to those simple residues, as monomers and in oligopeptides, and may be dominated by different interactions towards poly-condensation.

The first molecules of interest could be negatively charged side-chain amino acids aspartic acid (D) and glutamic acid (E). Based on the conclusions of the experiments summarized in CHAPTER 3, the carboxylic acid functionality on these amino acid would likely be able to esterify with silanols. The separation of the side-chain carboxylic acid from the amine by an additional 1 or 2 CH_2 units, compared to the α-carbonyl, contributes to the increased pka. The pka values for D and E, 3.9 and 4.1 respectively, are much closer to those of hydroxy acids, MOPA, and NAG, all of which are able to form silyl-esters under evaporative conditions at 85°C. These amino acids could possess the dual role of activation, by the ester-forming electrophilic side-chain carboxyl, and amide formation, by the nucleophilic amine. Though the initial ester aminolysis step would produce a branched dipeptide, once the amine is incorporated in an amide bond, the acidity of the C-terminus primary carboxylic acid decreases and becomes more amenable to subsequent esterification, much like the behavior of NAG or tri-glycine. From a population of these dipeptides, a continued process of elongation via EAX may proceed, though it is likely that there will be competition between the primary and side-chain carboxylic acids for esterification. The differences in side-chain carboxyl pka values between D and E might affect this competition as well and possibly limit one system to only one linkage site. Beta-alanine is another amino acid that may be capable of both forming an initial silyl-ester and amide formation via EAX. This could be another self-supporting system, similar to those containing Glu or Asp, but would not encounter difficulties with branching.

6.2.3   Prebiotic Proto-Lipid System

The silyl-ester aminolysis mechanism might be applied to another prebiotic system, distinct from proto-peptide formation. If silica may be considered a viable ester forming substrate, then step-wise reaction with some long-chain carboxylic acid, such as decanoic acid, and the resulting silyl esters could act as activated sites for trans-esterification by subsequently added sugars. This process might offer a plausible route to prebiotic vesicles using the resulting amphiphilic molecules.

APPENDIX A.   SYNTHESIS OF MOPA-CAPPED

OLIGOGLYCINE STANDARDS

The following synthesis, analysis and results of molecules appearing in Appendix A were performed in their entirety and reported by Luke J. Leman, within the Department of Chemistry at The Scripps Research Institute, La Jolla, California.

A.1   (S)-MOPA-Gly-OH
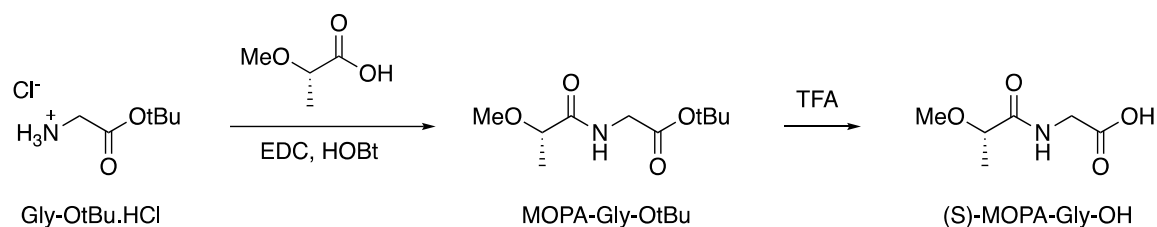
Figure A 1   Scheme for production of MOPA–G

(S)-methoxypropionic acid (MOPA, Combi-Blocks #QE-5921, 0.114 g, 1.1 mmol) was dissolved in DCM (4 mL). Next, HOBt.H2O (0.168 g, 1.1 mmol) and EDC.HCl (0.211 g, 1.1 mmol) were added. This was followed by the addition of H-Gly-OtBu.HCl (Alfa-Aesar #L17116, 0.168 g, 1.0 mmol) and triethylamine (0.21 mL, 1.5 mmol). The solution was stirred at room temperature for 14 h. The solution was diluted with DCM (50 mL), washed three times with sat. NaHCO$_3$, three time with 1 N HCl, and brine. After drying over MgSO$_4$, the solvent was evaporated to yield a clear oil. The crude product was dissolved in neat TFA and allowed to stand at RT for 1 h. After evaporation of the solvent, the desired compound was purified by preparative HPLC. Lyophillization yielded 0.121 mg of a clear oil (75% yield over two steps).

^{1}H-NMR (500 MHz, DMSO) δ 8.07-8.05 (t, 1H), 3.82-3.69 (m, 3H), 3.29 (s, 3H), 1.23-1.21 (d, 3H). ^{13}C NMR (126 MHz, DMSO) δ 173.23, 171.60, 77.75, 57.28, 40.72, 18.75.

HRMS: calculated as 162.0766 amu [M+H] for $C_6H_{11}NO_4$, observed as 162.0765 amu.

A.2 (S)-MOPA-Gly-Gly-OH
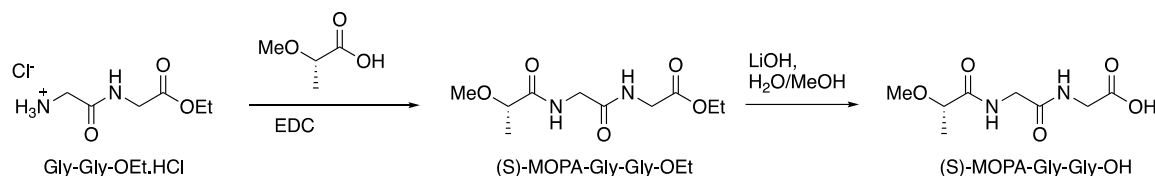
Figure A 2   **Scheme for production of MOPA–G$_2$**

(S)-methoxypropionic acid (MOPA, Combi-Blocks #QE-5921, 0.114 g, 1.1 mmol) was dissolved in DCM (4 mL). Next, HOBt.H2O (0.168 g, 1.1 mmol) and EDC.HCl (0.211 g, 1.1 mmol) were added. This was followed by the addition of H-Gly-Gly-OEt.HCl (Sigma #G-3129, 0.197 g, 1.0 mmol) and triethylamine (0.21 mL, 1.5 mmol). The solution was stirred at room temperature for 14 h. The solution was evaporated to an oil the desired compound was purified by preparative HPLC and the fractions containing product were evaporated to an oil. The residue was dissolved in a mixture of water/MeOH (1:1) and LiOH.H2O (0.126 g, 3 mmol) was added. The mixture stirred at RT for 15 h, after which time the solvent was evaporated and the product was purified by preparative HPLC. Lyophillization yielded 0.170 mg of a sticky solid (78% yield over two steps).

^{1}H-NMR (500 MHz, DMSO) δ 8.06-8.04 (t, 1H), 8.01-7.99 (t, 1H), 3.81-3.69 (m, 5H), 3.29 (s, 3H), 1.23-1.22 (d, 3H). ^{13}C NMR (126 MHz, DMSO) δ 173.08, 171.58, 169.29, 77.72, 57.31, 41.86, 41.58, 18.65.

HRMS: calculated as 219.0981 amu [M+H] for $C_8H_{14}N_2O_5$, observed as 219.0986 amu.

A.3   (S)-MOPA-Gly-Gly-Gly-OH

(S)-MOPA-Gly-Gly-Gly-OH
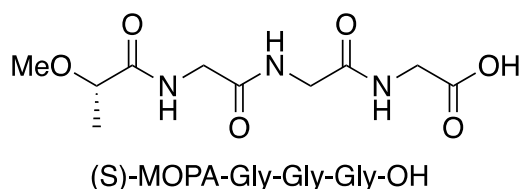
Figure A 3   Chemical structure for MOPA–G$_3$

The title compound was synthesized via standard Fmoc solid-phase peptide synthesis protocols on 0.4 mmol scale using H-Gly-chlorotrityl chloride resin (Chem-Impex). Coupling reactions were carried out using a four-fold excess of oxyma, diisopropylcarbodiimide, and Fmoc-protected amino acid or (S)-MOPA for 75 min. Fmoc deprotection steps were carried out by treating the resin with 25% 4-methylpiperidine/DMF twice for 10 min. The peptide was cleaved from the resin using 95:2.5:2.5 TFA/H$_2$O/triethylsilane for 10 min. The cleavage solution was evaporated to yield an oil, and the desired compound was purified by preparative HPLC using a water/acetonitrile/TFA solvent system. Fractions containing the product were lyophilized to yield 11 mg of a white powder (10% yield based on resin loading).

High resolution ESI-TOF MS (m/z): calculated as 276.1196 amu [M+H] for $C_{10}H_{17}N_3O_6$, and observed as 276.1200 amu.

APPENDIX B. INVESTIGATION OF PREBIOTIC MINERALS BY X-RAY PHOTOELECTRON SPECTROSCOPY[4,5]

B.1 Background

Chemical process that proceed at liquid/mineral interfaces are commonly studied indirectly by bulk phase measurements of the solution phase. However, it is always the case that mineral-involved reactions occur at the surface and therefore are determined by its chemical properties. Photoelectron spectroscopy is a technique that primarily detects electrons emitted from a substrate that have not scattered. The mean free path for such conditions is typically limited to <10 nm for core shell electrons, and is therefore a technique sensitive to exclusively the top layers of a sample. Specific chemical knowledge of this region necessary in many research fields, including prebiotic chemistry. The following accounts summarize the application of x-ray photoelectron spectrometry (XPS) analysis, carried out on the Electron Spectroscopy for Chemical Analysis (ESCA) instrument that I personally rebuilt with assistance from Service Physics LLC staff and Dr. Reuben Gann.

---

[4] The work summarized in Appendix B.1 has been reported in a recently submitted manuscript. Schaible, Micah; Pinto, Henry; McKee, Aaron; Leszczynski, Jerzy; Orlando, Thomas "Characterization and Simulation of Natural Pyrite Surfaces: A Combined Experimental and Theoretical Study" *J. Phys. Chem. C* **2019** XXXX, XXX, XXX-XXX

[5] The work summarized in Appendix B.2 has been reported in previously published work. La Cruz, Nikita L.; Qasim, Danna; Abbott-Lyon, Heather; Pirim, Claire; McKee, Aaron D.; Orlando, Thomas; Gull, Maheen; Lindsay, Danny; Pasek, Matthew A. "The evolution of the surface of the mineral schreibersite in prebiotic chemistry" *Phys.Chem.Chem.Phys.*, **2016**, 18, 20160

B.1   S-Deficient Phases of Iron Sulfide Crystals on a Natural Pyrite Surface

Pyrite (FeS_2) is one of the most abundant metal sulfides in the Earth's crust and is prominent in submarine hydrothermal vent systems [185]. A popular theory of chemical evolution described by Wächtershäuser postulates that the exothermic production of FeS_2 could have provided chemical energy to prebiotic metabolic systems [186]. An important tenant of the so-called iron-sulfur world theory is the adsorption of organic molecule to the pyrite surface for the purpose of concentration, as that could not be achieved by evaporation under water. Despite the potential importance of this mineral, few studies have examined the surface features of natural samples, in lieu of pristine and well prepared samples [187, 188]. Because the surface stoichiometry dictates mineral reactivity, this project sought to determine the true terminating motifs of an otherwise FeS_2 sample.

Examination by XPS of the S-2p transition revealed a sulfur deficient surface with a near unity S:Fe ratio instead of the bulk ratio of 2. To identify the precise surface termination motif, the sample was analyzed by the ultra-violet photoelectron spectroscopy (UPS) technique. The experimental results where compared to simulated spectra from several known iron sulfide terminations: pyrite FeS_2, troilite FeS, pyrrhotite Fe_7S_8 and greigite Fe_3S_4. The motifs that can account for the observed data were the FeS and Fe_7S_8 systems. Simulation of a FeS_2 termination with S-vacancies, as suggested by the XPS data, was not able to recreate the observed UPS spectrum. In summary, the results suggest that the surface of a sample of natural pyrite can be described as a stoichiometric bulk FeS_2 coated by some S-deficient phase of iron sulfide like FeS or Fe_7S_8, and should be the assumed terminating motif for naturally occurring pyrite minerals.

B.2   Evolution of the Surface of the Mineral Schreibersite in Prebiotic Chemistry

It is apparent by a cursory appraisal that phosphorous (P) is a vital element in biology. Though its presence in proto-RNA macromolecules is unknown, P is a necessary component of nucleic acids, and its source on early Earth is of interest. While P itself has never been rare, a non-oxidized form, which would be amenable to reaction with organic compounds, is not yet known. One theory is that the mineral Schreibersite $(Fe,Ni)_3P$ could have been the source. While it is not unreasonable to attribute the source of P to a mineral that is non-terrestrial and exclusively found in meteorites, that fact does cause issue for modern experimentation, due to rarity. Therefore, it would be highly desirable to produce a synthetic iron-nickel phosphide in a laboratory setting.

The most desirable characteristic of schreibresite and therefore the attribute which is highest priority to recreate is the P in a reduced state. XPS is well adept at resolving elements in various oxidative states, due to the decreased binding energy for an electron in a core shell of an element in a more reduced state. The binding energy for such an oxidation state was determined to be 129.7 eV, consistent with actual meteoritic Schreibersite samples. By this technique, various synthetic procedures were assessed until a product which presented a reduced P-2p signal was determined. The corrosion process by water with and without salt was subsequently investigated. It was found that samples subjected to deionized water formed surface oxides at a much slower rate that when salted water was used. While the precise identity of the phosphorous oxide could not be determined, the peak was notably broad which suggests several P-species of various oxidation states, one of which might be the species responsible for phosphorylation of choline.

177

REFERENCES

1.   Luisi, P.L., *About various definitions of life.* Origins of Life and Evolution of the Biosphere, 1998. **28**(4-6): p. 613-622.

2.   Deamer, D.W. and G.R. Fleischaker, *Origins of life : the central concepts*. 1994, Boston: Jones and Bartlett Publishers.

3.   Benner, S.A., *Defining Life.* Astrobiology, 2010. **10**(10): p. 1021-1030.

4.   Margulis, L. and D. Sagan, *What is Life?* 1995, London: Weidenfeld and Nicholson.

5.   Oparin, A.I., *The Origin of Life*. 1938, New York, NY: MacMillan.

6.   Piries, N.M., Discovery, 1953. **14**.

7.   Oparin, A.I., *Life: Its Nature, Origin and Development*. 1961: Academic Press. 207.

8.   Cafferty, B.J., et al., *Efficient self-assembly in water of long noncovalent polymers by nucleobase analogues.* Journal of the American Chemical Society, 2013. **135**(7): p. 2447-2450.

9.   Miller, S.L., *A Production of Amino Acids Under Possible Primitive Earth Conditions.* Science, 1953. **117**(3046): p. 528-529.

10.   Engel, M.H., S.A. Macko, and J.A. Silfer, *Carbon isotope composition of individual amino acids in the Murchison meteorite.* Nature, 1990. **348**(6296): p. 47-49.

11.   Peltzer, E.T. and J.L. Bada, *[alpha]-Hydroxycarboxylic acids in the Murchison meteorite.* Nature, 1978. **272**(5652): p. 443-444.

12.   Chyba, C. and C. Sagan, *Endogenous production, exogenous delivery and impact-shock synthesis of organic molecules: an inventory for the origins of life.* Nature, 1992. **355**(6356): p. 125.

13.   Gilbert, W., *Origin of life: The RNA world.* nature, 1986. **319**(6055): p. 618.

14.   Kruger, K., et al., *Self-splicing RNA: autoexcision and autocyclization of the ribosomal RNA intervening sequence of Tetrahymena.* cell, 1982. **31**(1): p. 147-157.

15.   Joyce, G.F., *RNA evolution and the origins of life.* Nature, 1989. **338**(6212): p. 217.

16.   Cedergren, R. and H. Grosjean, *On the primacy of primordial RNA.* BioSystems, 1987. **20**(2): p. 175-180.

17.   Bean, H.D., et al., *Formation of a β-pyrimidine nucleoside by a free pyrimidine base and ribose in a plausible prebiotic reaction.* Journal of the American Chemical Society, 2007. **129**(31): p. 9556-9557.

18.   Zubay, G. and T. Mui, *Prebiotic synthesis of nucleotides.* Origins of Life and Evolution of the Biosphere, 2001. **31**(1-2): p. 87-102.

19.   Dyson, F.J., *Origins of life.* 1985.

20.   Bourbo, V., et al., *Self-assembly and self-replication of short amphiphilic β-sheet peptides.* Origins of Life and Evolution of Biospheres, 2011. **41**(6): p. 563-567.

21.   Nelson, K.E., M. Levy, and S.L. Miller, *Peptide nucleic acids rather than RNA may have been the first genetic molecule.* Proceedings of the National Academy of Sciences, 2000. **97**(8): p. 3868-3871.

22.   Burton, A.S., et al., *Understanding prebiotic chemistry through the analysis of extraterrestrial amino acids and nucleobases in meteorites.* Chemical Society Reviews, 2012. **41**(16): p. 5459-5472.

23.   Marshall-Bowman, K., et al., *Catalytic peptide hydrolysis by mineral surface: Implications for prebiotic chemistry.* Geochimica et Cosmochimica Acta, 2010. **74**(20): p. 5852-5861.

24.   Kristof, P., R. Hannes, and M.R. Bernd, *Prebiotic Chemistry: The Amino Acid and Peptide World.* Current Organic Chemistry, 2005. **9**(12): p. 1107-1114.

25.   Martin, R.B., *Free energies and equilibria of peptide bond hydrolysis and formation.* Biopolymers: Original Research on Biomolecules, 1998. **45**(5): p. 351-353.

26.   Fox, S.W. and K. Harada, *The thermal copolymerization of amino acids common to protein1.* Journal of the American Chemical Society, 1960. **82**(14): p. 3745-3751.

27.   Fox, S.W. and K. Harada, *Thermal copolymerization of amino acids to a product resembling protein.* Science, 1958. **128**(3333): p. 1214-1214.

28.	Orgel, L.E., *The origin of polynucleotide-directed protein synthesis.* Journal of molecular evolution, 1989. **29**(6): p. 465-474.

29.	Lahav, N., D. White, and S. Chang, *Peptide formation in the prebiotic era: thermal condensation of glycine in fluctuating clay environments.* Science, 1978. **201**(4350): p. 67-69.

30.	Cafferty, B.J., D.M. Fialho, and N.V. Hud, *Searching for Possible Ancestors of RNA: The Self-Assembly Hypothesis for the Origin of Proto-RNA*, in *Prebiotic Chemistry and Chemical Evolution of Nucleic Acids*. 2018, Springer. p. 143-174.

31.	Bean, H.D., et al., *Glyoxylate as a backbone linkage for a prebiotic ancestor of RNA.* Origins of Life and Evolution of Biospheres, 2006. **36**(1): p. 39-63.

32.	Mamajanov, I., et al., *Ester formation and hydrolysis during wet–dry cycles: generation of far-from-equilibrium polymers in a model prebiotic reaction.* Macromolecules, 2014. **47**(4): p. 1334-1343.

33.	Forsythe, J.G., et al., *Ester-Mediated Amide Bond Formation Driven by Wet–Dry Cycles: A Possible Path to Polypeptides on the Prebiotic Earth.* Angewandte Chemie International Edition, 2015. **54**(34): p. 9871-9875.

34.	Weber, A.L., *Prebiotic amino acid thioester synthesis: thiol-dependent amino acid synthesis from formose substrates (formaldehyde and glycolaldehyde) and ammonia.* Origins of Life and Evolution of the Biosphere, 1998. **28**(3): p. 259-270.

35.	Krishnamurthy, R., *Life's Biological Chemistry: A Destiny or Destination Starting from Prebiotic Chemistry?* Chemistry – A European Journal, 2018. **24**(63): p. 16708-16715.

36.	Gavette, J.V., et al., *RNA–DNA Chimeras in the Context of an RNA World Transition to an RNA/DNA World.* Angewandte Chemie International Edition, 2016. **55**(42): p. 13204-13209.

37.	Schork, J., et al., *Polycondensation in the primordial world: A hypothesis for the evolution of the first biopolymers.* 2015.

38.	Stribling, R. and S.L. Miller, *Energy yields for hydrogen cyanide and formaldehyde syntheses: The hcn and amino acid concentrations in the primitive ocean.* Origins of life and evolution of the biosphere, 1987. **17**(3): p. 261-273.

39.	Mulkidjanian, A.Y., et al., *Origin of first cells at terrestrial, anoxic geothermal fields.* Proceedings of the National Academy of Sciences, 2012. **109**(14): p. E821.

40.	Nelson, K.E., et al., *Concentration by Evaporation and the Prebiotic Synthesis of Cytosine.* Origins of life and evolution of the biosphere, 2001. **31**(3): p. 221-229.

41.   Lambert, J.-F., *Adsorption and Polymerization of Amino Acids on Mineral Surfaces: A Review.* Origins of Life and Evolution of Biospheres, 2008. **38**(3): p. 211-242.

42.   Bernal, J.D., *The physical basis of life*. 1951: Routledge and Paul.

43.   Ma, Z. and F. Zaera, *Organic chemistry on solid surfaces.* Surface Science Reports, 2006. **61**(5): p. 229-281.

44.   James Cleaves Ii, H., et al., *Mineral-organic interfacial processes: potential roles in the origins of life.* Chemical Society Reviews, 2012. **41**(16): p. 5502-5525.

45.   Drake, M., et al. *Asteroids, Comets, Meteors*. in *Proc. IAU*. 2005.

46.   Hazen, R.M., et al., *Mineral evolution.* American Mineralogist, 2008. **93**(11-12): p. 1693-1720.

47.   Gomes, R., et al., *Origin of the cataclysmic Late Heavy Bombardment period of the terrestrial planets.* Nature, 2005. **435**(7041): p. 466.

48.   Deer, W.A., et al., *Rock-forming minerals. Volume 4B: Framework silicates: silica minerals, feldspathoids and the zeolites*. 2 ed. 2004: Geological Society, Geological Society Publishing House. 982.

49.   McDonough, W.F. and S.s. Sun, *The composition of the Earth.* Chemical Geology, 1995. **120**(3): p. 223-253.

50.   Schoonen, M., A. Smirnov, and C. Cohn, *A Perspective on the Role of Minerals in Prebiotic Synthesis*. Vol. 33. 2004: BIOONE. 539-551, 13.

51.   Norrish, K., *The swelling of montmorillonite.* Discussions of the Faraday society, 1954. **18**: p. 120-134.

52.   Pelletier, J.D.A. and J.-M. Basset, *Catalysis by Design: Well-Defined Single-Site Heterogeneous Catalysts.* Accounts of Chemical Research, 2016. **49**(4): p. 664-677.

53.   Kyzas, G.Z. and K.A. Matis, *Nanoadsorbents for pollutants removal: A review.* Journal of Molecular Liquids, 2015. **203**: p. 159-168.

54.   Chen, C., et al., *Amine–silica composites for CO2 capture: A short review.* Journal of Energy Chemistry, 2017. **26**(5): p. 868-880.

55.   Smith, G.V. and F. Notheisz, *Heterogeneous Catalysis in Organic Chemistry*. 1999: Elsevier Science.

56.   Stievano, L., et al., *Glycine and lysine adsorption and reactivity on the surface of amorphous silica.* European Journal of Mineralogy, 2007. **19**(3): p. 321-331.

57.   Meng, M., L. Stievano, and J.-F. Lambert, *Adsorption and Thermal Condensation Mechanisms of Amino Acids on Oxide Supports. 1. Glycine on Silica.* Langmuir, 2004. **20**(3): p. 914-923.

58.   Forsythe, J.G., et al., *Ester-Mediated Amide Bond Formation Driven by Wet–Dry Cycles: A Possible Path to Polypeptides on the Prebiotic Earth.* Angewandte Chemie International Edition, 2015. **54**(34): p. 9871--9875.

59.   Kitadai, N., et al., *Glycine Polymerization on Oxide Minerals.* Origins of Life and Evolution of Biospheres, 2017. **47**(2): p. 123-143.

60.   Fox, S., et al., *Hypercondensation of an amino acid: synthesis and characterization of a black glycine polymer.* Chemistry–A European Journal, 2015. **21**(24): p. 8897-8904.

61.   Clark, B.C. and V.M. Kolb, *Comet Pond II: Synergistic Intersection of Concentrated Extraterrestrial Materials and Planetary Environments to Form Procreative Darwinian Ponds.* Life (Basel), 2018. **8**(2).

62.   Holm, N.G., *Why are hydrothermal systems proposed as plausible environments for the origin of life?*, in *Marine Hydrothermal Systems and the Origin of Life*. 1992, Springer. p. 5-14.

63.   Feng, S., et al., *Hydrothermal biochemistry: from formaldehyde to oligopeptides.* Journal of Materials Science, 2008. **43**(7): p. 2418-2425.

64.   Rushdi, A.I. and B.R. Simoneit, *Abiotic condensation synthesis of glyceride lipids and wax esters under simulated hydrothermal conditions.* Origins of Life and Evolution of Biospheres, 2006. **36**(2): p. 93-108.

65.   Maheen, G., et al., *Resolving the enigma of prebiotic C☐ O☐ P bond formation: Prebiotic hydrothermal synthesis of important biological phosphate esters.* Heteroatom Chemistry: An International Journal of Main Group Elements, 2010. **21**(3): p. 161-167.

66.   Simeone, R., et al., *Mineralogical and stable isotope studies of kaolin deposits: shallow epithermal systems of western Sardinia, Italy.* Economic Geology, 2005. **100**(1): p. 115-130.

67.   Ferris, J.P., *Montmorillonite-catalysed formation of RNA oligomers: the possible role of catalysis in the origins of life.* Philosophical Transactions of the Royal Society B: Biological Sciences, 2006. **361**(1474): p. 1777-1786.

68.   Hazen, R.M. and D.A. Sverjensky, *Mineral surfaces, geochemical complexities, and the origins of life.* Cold Spring Harbor perspectives in biology, 2010. **2**(5): p. a002162-a002162.

69. Parks, G.A., *Aqueous Surface Chemistry of Oxides and Complex Oxide Minerals*, in *Equilibrium Concepts in Natural Water Systems*. 1967, AMERICAN CHEMICAL SOCIETY. p. 121-160.

70. Kosmulski, M., *Surface charging and points of zero charge*. Surfactant Science Series, ed. A.T. Hubbard. 2009, New York, NY: CRC press. 1064.

71. Davis, J.A., R.O. James, and J.O. Leckie, *Surface ionization and complexation at the oxide/water interface: I. Computation of electrical double layer properties in simple electrolytes.* Journal of Colloid and Interface Science, 1978. **63**(3): p. 480-499.

72. Lahav, N. and S. Chang, *The possible role of solid surface area in condensation reactions during chemical evolution: reevaluation.* Journal of molecular evolution, 1976. **8**(4): p. 357-380.

73. Yang, Y., et al., *Adsorption of Lysine on Na-Montmorillonite and Competition with Ca2+: A Combined XRD and ATR-FTIR Study.* Langmuir, 2016. **32**(19): p. 4746-4754.

74. Fuchida, S., H. Masuda, and K. Shinoda, *Peptide formation mechanism on montmorillonite under thermal conditions.* Origins of Life and Evolution of Biospheres, 2014. **44**(1): p. 13-28.

75. Deiana, C., et al., *Direct Synthesis of Amides from Carboxylic Acids and Amines by Using Heterogeneous Catalysts: Evidence of Surface Carboxylates as Activated Electrophilic Species.* ChemCatChem, 2013. **5**(10): p. 2832-2834.

76. Martra, G., et al., *The Formation and Self-Assembly of Long Prebiotic Oligomers Produced by the Condensation of Unactivated Amino Acids on Oxide Surfaces.* Angew. Chem., Int. Ed., 2014. **53**(18): p. 4671-4674.

77. Rimola, A., et al., *Does Silica Surface Catalyse Peptide Bond Formation? New Insights from First-Principles Calculations.* ChemPhysChem, 2006. **7**(1): p. 157-163.

78. Rimola, A., et al., *Interaction of Glycine with Isolated Hydroxyl Groups at the Silica Surface: First Principles B3LYP Periodic Simulation.* Langmuir, 2006. **22**(15): p. 6593-6604.

79. Rimola, A., et al., *How Does Silica Catalyze the Amide Bond Formation under Dry Conditions? Role of Specific Surface Silanol Pairs.* ACS Catalysis, 2018. **8**(5): p. 4558-4568.

80. Lomenech, C., et al., *Theoretical and Experimental Study of the Adsorption of Neutral Glycine on Silica from the Gas Phase.* ChemPhysChem, 2005. **6**(6): p. 1061-1070.

81.   Furumai, R., et al., *FK228 (Depsipeptide) as a Natural Prodrug That Inhibits Class I Histone Deacetylases.* Cancer Research, 2002. **62**(17): p. 4916-4921.

82.   Søgaard, O.S., et al., *The Depsipeptide Romidepsin Reverses HIV-1 Latency In Vivo.* PLOS Pathogens, 2015. **11**(9): p. e1005142.

83.   Bada, J.L., *New insights into prebiotic chemistry from Stanley Miller's spark discharge experiments.* Chemical Society Reviews, 2013. **42**(5): p. 2186-2196.

84.   Yu, S.-S., et al., *Kinetics of prebiotic depsipeptide formation from the ester–amide exchange reaction.* Physical Chemistry Chemical Physics, 2016. **18**(41): p. 28441-28450.

85.   Parker, E.T., et al., *A plausible simultaneous synthesis of amino acids and simple peptides on the primordial earth.* Angew. Chem. Int. Edit., 2014. **126**(31): p. 8270-8274.

86.   Parker, E.T., et al., *Quantitation of α-hydroxy acids in complex prebiotic mixtures via liquid chromatography/tandem mass spectrometry.* Rapid Commun. Mass Sp., 2016. **30**(18): p. 2043-2051.

87.   Lahav, N. and S. Chang, *Possible role of solid surface area in condensation reactions during chemical evolution: reevaluation.* J. Mol. Evol., 1976. **8**(4): p. 357-380.

88.   Lambert, J.-F., *Adsorption and Polymerization of Amino Acids on Mineral Surfaces: A Review.* Origins Life Evol. B, 2008. **38**(3): p. 211-242.

89.   James Cleaves Ii, H., et al., *Mineral-organic interfacial processes: potential roles in the origins of life.* Chem. Soc. Rev., 2012. **41**(16): p. 5502-5525.

90.   Rimola, A., et al., *Silica Surface Features and Their Role in the Adsorption of Biomolecules: Computational Modeling and Experiments.* Chem. Rev., 2013. **113**(6): p. 4216-4313.

91.   Martra, G., et al., *The Formation and Self-Assembly of Long Prebiotic Oligomers Produced by the Condensation of Unactivated Amino Acids on Oxide Surfaces.* Angew. Chem. Int. Edit., 2014. **53**(18): p. 4671-4674.

92.   Bujdák, J. and B.M. Rode, *Activated alumina as an energy source for peptide bond formation: Consequences for mineral-mediated prebiotic processes.* Amino Acids, 2001. **21**(3): p. 281-291.

93.   Yu, S.-S., et al., *Elongation of Model Prebiotic Proto-Peptides by Continuous Monomer Feeding.* Macromolecules, 2017. **50**(23): p. 9286-9294.

94.   Rodriguez-Garcia, M., et al., *Formation of oligopeptides in high yield under simple programmable conditions.* Nat. Commun., 2015. **6**.

95.	Forsythe, J.G., et al., *Ester-Mediated Amide Bond Formation Driven by Wet–Dry Cycles: A Possible Path to Polypeptides on the Prebiotic Earth.* Angew. Chem. Int. Edit., 2015. **54**(34): p. 9871--9875.

96.	Espartero, J.L., et al., *NMR Analysis of Low Molecular Weight Poly(lactic acid)s.* Macromolecules, 1996. **29**(10): p. 3535-3539.

97.	Kitadai, N., et al., *Glycine Polymerization on Oxide Minerals.* Origins Life Evol. B., 2017. **47**(2): p. 123-143.

98.	Thiel, P.A. and T.E. Madey, *The interaction of water with solid surfaces: Fundamental aspects.* Surf. Sci. Rep., 1987. **7**(6): p. 211-385.

99.	Sugiyama, N., et al., *Phosphopeptide Enrichment by Aliphatic Hydroxy Acid-modified Metal Oxide Chromatography for Nano-LC-MS/MS in Proteomics Applications.* Mol. Cell Proteomics, 2007. **6**(6): p. 1103-1109.

100.	White, D.H., R.M. Kennedy, and J. Macklin, *Acyl silicates and acyl aluminates as activated intermediates in peptide formation on clays.* Orig. Life, 1984. **14**(1): p. 273-278.

101.	O'Hara, M.J., *Primary magmas and the origin of basalts.* Scot. J. Geol., 1965. **1**(1): p. 19-40.

102.	Kitadai, N., et al., *Glycine Polymerization on Oxide Minerals.* Origins of Life and Evolution of BiospheresEvol. B, 2017. **47**(2): p. 123-143.

103.	Dalai, P., et al., *The Influence of Mineral Matrices on the Thermal Behavior of Glycine.* Origins of Life and Evolution of Biospheres, 2017. **47**(4): p. 427-452.

104.	Basiuk, V.A., et al., *Mechanisms of amino acid polycondensation on silica and alumina surfaces.* Origins of life and evolution of the biosphere, 1990. **20**(6): p. 483-498.

105.	Cassanas, G., et al., *Vibrational spectra of lactic acid and lactates.* J. Raman Spectrosc., 1991. **22**(7): p. 409-413.

106.	Meaurio, E., N. López-Rodríguez, and J.R. Sarasua, *Infrared Spectrum of Poly(l-lactide): Application to Crystallinity Studies.* Macromolecules, 2006. **39**(26): p. 9291-9301.

107.	McKee, A.D., et al., *A Possible Path to Prebiotic Peptides Involving Silica and Hydroxy Acid-Mediated Amide Bond Formation.* ChemBioChem, 2018. **19**(18): p. 1913-1917.

108.	Young, R., *Infrared spectroscopic studies of adsorption and catalysis. Part 3. Carboxylic acids and their derivatives adsorbed on silica.* Can. J. Chem., 1969. **47**(12): p. 2237-2247.

109.   Buckingham, D.A., D.M. Foster, and A.M. Sargeson, *Cobalt(III)-promoted amidolysis of glycine ethyl ester. An example of internal nucleophilic displacement.* Journal of the American Chemical Society, 1969. **91**(13): p. 3451-3456.

110.   Bujdák, J. and B. Rode, *Peptide bond formation on the surface of activated alumina: peptide chain elongation.* Catalysis letters, 2003. **91**(3-4): p. 149-154.

111.   Lambert, J.-F., et al., *A comparative study of the catalysis of peptide bond formation by oxide surfaces.* Physical Chemistry Chemical Physics, 2013. **15**(32): p. 13371-13380.

112.   Grover, M.A., et al., *A Chemical Engineering Perspective on the Origins of Life.* Processes, 2015. **3**(2): p. 309-338.

113.   Morrow, B.A. and A.J. McFarlan, *Chemical reactions at silica surfaces.* Journal of Non-Crystalline Solids, 1990. **120**(1): p. 61-71.

114.   Rodriguez-Garcia, M., et al., *Formation of oligopeptides in high yield under simple programmable conditions.* Nature Communications, 2015. **6**: p. 8385.

115.   Young, R.P., *Infrared spectroscopic studies of adsorption and catalysis. Part 3. Carboxylic acids and their derivatives adsorbed on silica.* Canadian Journal of Chemistry, 1969. **47**(12): p. 2237-2247.

116.   Cassanas, G., et al., *Vibrational spectra of lactic acid and lactates.* Journal of Raman Spectroscopy, 1991. **22**(7): p. 409-413.

117.   Ma, X.-k., et al., *Surface modification and characterization of highly dispersed silica nanoparticles by a cationic surfactant.* Colloids and Surfaces A: Physicochemical and Engineering Aspects, 2010. **358**(1–3): p. 172-176.

118.   Chuang, I.S. and G.E. Maciel, *A Detailed Model of Local Structure and Silanol Hydrogen Bonding of Silica Gel Surfaces.* The Journal of Physical Chemistry B, 1997. **101**(16): p. 3052-3064.

119.   Rimola, A., M. Sodupe, and P. Ugliengo, *Amide and Peptide Bond Formation: Interplay between Strained Ring Defects and Silanol Groups at Amorphous Silica Surfaces.* The Journal of Physical Chemistry C, 2016. **120**(43): p. 24817-24826.

120.   McDonald, R.S., *Surface Functionality of Amorphous Silica by Infrared Spectroscopy.* The Journal of Physical Chemistry, 1958. **62**(10): p. 1168-1178.

121.   Burneau, A. and C. Carteret, *Near infrared and ab initio study of the vibrational modes of isolated silanol on silica.* Physical Chemistry Chemical Physics, 2000. **2**(14): p. 3217-3226.

122.   Martra, G., et al., *The Formation and Self-Assembly of Long Prebiotic Oligomers Produced by the Condensation of Unactivated Amino Acids on Oxide Surfaces.* Angewandte Chemie International Edition, 2014. **53**(18): p. 4671-4674.

123.   Alves, M.R., et al., *Chemistry and Photochemistry of Pyruvic Acid Adsorbed on Oxide Surfaces.* The Journal of Physical Chemistry A, 2019.

124.   Zaki, M.I., M.A. Hasan, and L. Pasupulety, *Surface Reactions of Acetone on Al2O3, TiO2, ZrO2, and CeO2: IR Spectroscopic Assessment of Impacts of the Surface Acid−Base Properties.* Langmuir, 2001. **17**(3): p. 768-774.

125.   Frost, R.L. and A.M. Vassallo, *The Dehydroxylation of the Kaolinite Clay Minerals using Infrared Emission Spectroscopy.* Clays and Clay Minerals, 1996. **44**(5): p. 635-651.

126.   Kamata, H., et al., *SO2 oxidation over the V2O5/TiO2 SCR catalyst.* Catalysis Letters, 2001. **73**(1): p. 79-83.

127.   Sanchez, C., J. Livage, and G. Lucazeau, *Infrared and Raman study of amorphous V2O5.* Journal of Raman Spectroscopy, 1982. **12**(1): p. 68-72.

128.   Konwar, D., et al., *Esterification of carboxylic acids by acid activated Kaolinite clay.* Indian Journal of Chemical Technology, 2008. **15**(1): p. 75-78.

129.   Chen, M.C., et al., *Spontaneous Prebiotic Formation of a β-Ribofuranoside That Self-Assembles with a Complementary Heterocycle.* Journal of the American Chemical Society, 2014. **136**(15): p. 5640-5646.

130.   Islam, S., D.-K. Bučar, and M.W. Powner, *Prebiotic selection and assembly of proteinogenic amino acids and natural nucleotides from complex mixtures.* Nature Chemistry, 2017. **9**: p. 584.

131.   Fialho, D.M., et al., *Glycosylation of a model proto-RNA nucleobase with non-ribose sugars: implications for the prebiotic synthesis of nucleosides.* Organic & Biomolecular Chemistry, 2018. **16**(8): p. 1263-1271.

132.   Arumainayagam, C.R., et al., *Extraterrestrial prebiotic molecules: photochemistry vs. radiation chemistry of interstellar ices.* Chemical Society Reviews, 2019.

133.   Mingli, T. and Y. Zengliang, *Bioeffects of Low Energy Ion Beam Implantation: DNA Damage, Mutation and Gene Transter.* Plasma Science and Technology, 2007. **9**(4): p. 513-518.

134.   Boudaiffa, B., et al., *Resonant formation of DNA strand breaks by low-energy (3 to 20 eV) electrons.* Science, 2000. **287**(5458): p. 1658-1660.

135.   Antic, D., L. Parenteau, and L. Sanche, *Electron-Stimulated Desorption of H- from Condensed-Phase Deoxyribose Analogues: Dissociative Electron Attachment*

versus Resonance Decay into Dipolar Dissociation. The Journal of Physical Chemistry B, 2000. **104**(19): p. 4711-4716.

136. Ptasińska, S., et al., *Inelastic electron interaction (attachment/ionization) with deoxyribose.* The Journal of Chemical Physics, 2004. **120**(18): p. 8505-8511.

137. Kopyra, J., *Low energy electron attachment to the nucleotide deoxycytidine monophosphate: direct evidence for the molecular mechanisms of electron-induced DNA strand breaks.* Physical Chemistry Chemical Physics, 2012. **14**(23): p. 8287-8289.

138. McAllister, M., et al., *Understanding the Interaction between Low-Energy Electrons and DNA Nucleotides in Aqueous Solution.* Journal of Physical Chemistry Letters, 2015. **6**(15): p. 3091-3097.

139. Chen, Y.F., A. Aleksandrov, and T.M. Orlando, *Probing low-energy electron induced DNA damage using single photon ionization mass spectrometry.* International Journal of Mass Spectrometry, 2008. **277**(1-3): p. 314-320.

140. Alizadeh, E., T.M. Orlando, and L. Sanche, *Biomolecular Damage Induced by Ionizing Radiation: The Direct and Indirect Effects of Low-Energy Electrons on DNA*, in *Annual Review of Physical Chemistry, Vol 66*, M.A. Johnson and T.J. Martinez, Editors. 2015, Annual Reviews: Palo Alto. p. 379-398.

141. Alizadeh, E. and L. Sanche, *Precursors of Solvated Electrons in Radiobiological Physics and Chemistry.* Chemical Reviews, 2012. **112**(11): p. 5578-5602.

142. Naaman, R. and L. Sanche, *Low-Energy Electron Transmission through Thin-Film Molecular and Biomolecular Solids.* Chemical Reviews, 2007. **107**(5): p. 1553-1579.

143. Huels, M.A., et al., *Single, Double, and Multiple Double Strand Breaks Induced in DNA by 3−100 eV Electrons.* Journal of the American Chemical Society, 2003. **125**(15): p. 4467-4477.

144. Ptasinska, S., et al., *Damage to amino acid-nucleotide pairs induced by 1 eV electrons.* Physical Chemistry Chemical Physics, 2010. **12**(32): p. 9367-9372.

145. Solomun, T. and T. Skalicky, *The interaction of a protein-DNA surface complex with low-energy electrons.* Chemical Physics Letters, 2008. **453**(1-3): p. 101-104.

146. Bald, I., E. Illenberger, and J. Kopyra, *Damage of DNA by Low Energy Electrons (< 3 eV).* 1st Nano-Ibct Conference 2011 - Radiation Damage of Biomolecular Systems: Nanoscale Insights into Ion Beam Cancer Therapy, 2012. **373**.

147. Ptasińska, S. and L. Sanche, *On the mechanism of anion desorption from DNA induced by low energy electrons.* The Journal of Chemical Physics, 2006. **125**(14): p. 144713.

148. Kočišek, J., et al., *Electron Attachment to Microhydrated Deoxycytidine Monophosphate.* The Journal of Physical Chemistry B, 2018. **122**(20): p. 5212-5217.

149. Orlando, T.M., et al., *Low-energy electron diffraction and induced damage in hydrated DNA.* Journal of Chemical Physics, 2008. **128**: p. 195102.

150. Shao, Y., et al., *Unified Mechanism for the Generation of Isolated and Clustered DNA Damages by a Single Low Energy (5–10 eV) Electron.* The Journal of Physical Chemistry C, 2017. **121**(4): p. 2466-2472.

151. Park, Y., et al., *DNA Damage Induced by Low-Energy Electrons: Conversion of Thymine to 5,6-Dihydrothymine in the Oligonucleotide Trimer TpTpT.* Radiation Research, 2011. **175**(2): p. 240-246.

152. Sanche, L., *Low energy electron-driven damage in biomolecules.* European Physical Journal D, 2005. **35**(2): p. 367-390.

153. Simons, J., *How Do Low-Energy (0.1−2 eV) Electrons Cause DNA-Strand Breaks?* Accounts of Chemical Research, 2006. **39**(10): p. 772-779.

154. Schyman, P. and A. Laaksonen, *On the effect of low-energy electron induced DNA strand break in aqueous solution: A theoretical study indicating guanine as a weak link in DNA.* Journal of the American Chemical Society, 2008. **130**(37): p. 12254-+.

155. Rosenberg, R.A. and S.P. Frigo, *FUNDAMENTAL ASPECTS OF SYNCHROTRON RADIATION INITIATED SURFACE CHEMISTRY*, in *Chemical Applications of Synchrotron Radiation*. p. 462-516.

156. Brun, E., et al., *Damage Induced to DNA by Low-Energy (0-30 eV) Electrons under Vacuum and Atmospheric Conditions.* Journal of Physical Chemistry B, 2009. **113**(29): p. 10008-10013.

157. Ptasińska, S., et al., *X-ray induced damage in DNA monitored by X-ray photoelectron spectroscopy.* The Journal of Chemical Physics, 2008. **129**(6): p. 065102.

158. Rosenberg, R.A., et al., *The relationship between interfacial bonding and radiation damage in adsorbed DNA.* Physical Chemistry Chemical Physics, 2014. **16**(29): p. 15319-15325.

159. Xiao, F.X., et al., *Cleavage Enhancement of Specific Chemical Bonds in DNA by Cisplatin Radiosensitization.* Journal of Physical Chemistry B, 2013. **117**(17): p. 4893-4900.

160. Hashimoto, Y., et al., *Image Contrast in Energy-Filtered BSE Images at Ultra-Low Accelerating Voltages.* Microscopy Today, 2016. **24**(3): p. 20-25.

161.   Schaible, M.J., E. Woods, and T.M. Orlando, *Microscopy characterization of nucleotides deposited on gold and graphene substrates.* Microscopy Today, 2019. **In preparation**.

162.   Leclerc, G., et al., *Low-Energy (0-10 Ev) Electron Transmission Spectra of Multilayer Tryptophan Films.* Journal of Physical Chemistry, 1987. **91**(19): p. 4999-5001.

163.   Boudaiffa, B., et al., *Cross sections for low-energy (10-50 eV) electron damage to DNA.* Radiation Research, 2002. **157**(3): p. 227-234.

164.   Michaud, M., A. Wen, and L. Sanche, *Cross sections for low-energy (1-100 eV) electron elastic and inelastic scattering in amorphous ice.* Radiation Research, 2003. **159**(1): p. 3-22.

165.   Haume, K., et al., *Transport of secondary electrons through coatings of ion-irradiated metallic nanoparticles.* European Physical Journal D, 2018. **72**(6).

166.   Henneken, H., F. Scholze, and G. Ulm, *Lack of proportionality of total electron yield and soft x-ray absorption coefficient.* Journal of Applied Physics, 2000. **87**(1): p. 257-268.

167.   Alizadeh, E., et al., *Soft X-ray and Low Energy Electron-Induced Damage to DNA under N-2 and O-2 Atmospheres.* Journal of Physical Chemistry B, 2011. **115**(15): p. 4523-4531.

168.   Shirley, D.A., *HIGH-RESOLUTION X-RAY PHOTOEMISSION SPECTRUM OF VALENCE BANDS OF GOLD.* Physical Review B, 1972. **5**(12): p. 4709-&.

169.   Kummer, K., et al., *Electronic Structure of Genomic DNA: A Photoemission and X-ray Absorption Study.* The Journal of Physical Chemistry B, 2010. **114**(29): p. 9645-9652.

170.   Stevens, J.S., et al., *Quantitative analysis of complex amino acids and RGD peptides by X-ray photoelectron spectroscopy (XPS).* Surface and Interface Analysis, 2013. **45**(8): p. 1238-1246.

171.   Stevens, J.S. and S.L.M. Schroeder, *Quantitative analysis of saccharides by X-ray photoelectron spectroscopy.* Surface and Interface Analysis, 2009. **41**(6): p. 453-462.

172.   Kundu, S., et al., *Thermal Stability and Reducibility of Oxygen-Containing Functional Groups on Multiwalled Carbon Nanotube Surfaces: A Quantitative High-Resolution XPS and TPD/TPR Study.* Journal of Physical Chemistry C, 2008. **112**(43): p. 16869-16878.

173. Prabhakaran, K. and C.N.R. Rao, *ADSORPTION OF CARBONYL-COMPOUNDS ON CLEAN AND MODIFIED CU(110) SURFACES - A COMBINED EELS-UPS STUDY.* Applied Surface Science, 1990. **44**(3): p. 205-210.

174. Gomes, P.J., et al., *Energy Thresholds of DNA Damage Induced by UV Radiation: An XPS Study.* The Journal of Physical Chemistry B, 2015. **119**(17): p. 5404-5411.

175. Vilar, M.R., et al., *Interaction of Self-Assembled Monolayers of DNA with Electrons: HREELS and XPS Studies.* The Journal of Physical Chemistry B, 2008. **112**(23): p. 6957-6964.

176. Tsud, N., et al., *Adenine adlayers on Cu(111): XPS and NEXAFS study.* The Journal of Chemical Physics, 2015. **143**(17): p. 174704.

177. Klyachko, D.V., M.A. Huels, and L. Sanche, *Halogen anion formation in 5-halouracil films: X rays compared to subionization electrons.* Radiation Research, 1999. **151**(2): p. 177-187.

178. Li, Z., et al., *Low-Energy Electron-Induced DNA Damage: Effect of Base Sequence in Oligonucleotide Trimers.* Journal of the American Chemical Society, 2010. **132**(15): p. 5422-5427.

179. Zheng, Y., J.R. Wagner, and L. Sanche, *DNA damage induced by low-energy electrons: Electron transfer and diffraction.* Physical Review Letters, 2006. **96**(20): p. 4.

180. Michaud, H., et al., *Modelling and in-situ measurements of intense currents during a winter storm in the Gulf of Aigues-Mortes (NW Mediterranean Sea).* Comptes Rendus Geoscience, 2013. **345**(9-10): p. 361-372.

181. Rezaee, M., et al., *Absolute cross section for low-energy-electron damage to condensed macromolecules: A case study of DNA.* Physical Review E, 2012. **86**(3).

182. Cai, Z.L., et al., *Enhanced DNA damage induced by secondary electron emission from a tantalum surface exposed to soft X rays.* Radiation Research, 2006. **165**(3): p. 365-371.

183. Papineau, D., et al., *Mineral evolution.* American Mineralogist, 2008. **93**(11-12): p. 1693-1720.

184. Schulte, M., et al., *Serpentinization and Its Implications for Life on the Early Earth and Mars.* Astrobiology, 2006. **6**(2): p. 364-376.

185. Faber, M.S., et al., *Earth-Abundant Metal Pyrites (FeS2, CoS2, NiS2, and Their Alloys) for Highly Efficient Hydrogen Evolution and Polysulfide Reduction Electrocatalysis.* The Journal of Physical Chemistry C, 2014. **118**(37): p. 21347-21356.

186.   Wächtershäuser, G., *Pyrite formation, the first energy source for life: a hypothesis.* Systematic and Applied Microbiology, 1988. **10**(3): p. 207-210.

187.   Pettenkofer, C., W. Jaegermann, and M. Bronold, *Site Specific Surface Interaction of Electron-Donors and Acceptors on Fes2(100) Cleavage Planes.* Berichte Der Bunsen-Gesellschaft-Physical Chemistry Chemical Physics, 1991. **95**(5): p. 560-565.

188.   Bronold, M., Y. Tomm, and W. Jaegermann, *Surface states on cubic d-band semiconductor pyrite (FeS2).* Surface Science, 1994. **314**(3): p. L931-L936.